


University of Alberta

**High Resolution Spectroscopic and *Ab Initio* Studies of  
Chiral Molecular Complexes**

by

Zheng Su 

A thesis submitted to the Faculty of Graduate Studies and Research  
in partial fulfillment of the requirements for the degree of

Doctor of Philosophy

Department of Chemistry

Edmonton, Alberta  
Spring 2008



Library and  
Archives Canada

Bibliothèque et  
Archives Canada

Published Heritage  
Branch

Direction du  
Patrimoine de l'édition

395 Wellington Street  
Ottawa ON K1A 0N4  
Canada

395, rue Wellington  
Ottawa ON K1A 0N4  
Canada

*Your file    Votre référence*  
*ISBN: 978-0-494-45613-2*  
*Our file    Notre référence*  
*ISBN: 978-0-494-45613-2*

**NOTICE:**

The author has granted a non-exclusive license allowing Library and Archives Canada to reproduce, publish, archive, preserve, conserve, communicate to the public by telecommunication or on the Internet, loan, distribute and sell theses worldwide, for commercial or non-commercial purposes, in microform, paper, electronic and/or any other formats.

The author retains copyright ownership and moral rights in this thesis. Neither the thesis nor substantial extracts from it may be printed or otherwise reproduced without the author's permission.

**AVIS:**

L'auteur a accordé une licence non exclusive permettant à la Bibliothèque et Archives Canada de reproduire, publier, archiver, sauvegarder, conserver, transmettre au public par télécommunication ou par l'Internet, prêter, distribuer et vendre des thèses partout dans le monde, à des fins commerciales ou autres, sur support microforme, papier, électronique et/ou autres formats.

L'auteur conserve la propriété du droit d'auteur et des droits moraux qui protègent cette thèse. Ni la thèse ni des extraits substantiels de celle-ci ne doivent être imprimés ou autrement reproduits sans son autorisation.

---

In compliance with the Canadian Privacy Act some supporting forms may have been removed from this thesis.

Conformément à la loi canadienne sur la protection de la vie privée, quelques formulaires secondaires ont été enlevés de cette thèse.

While these forms may be included in the document page count, their removal does not represent any loss of content from the thesis.

Bien que ces formulaires aient inclus dans la pagination, il n'y aura aucun contenu manquant.

  
**Canada**

## ABSTRACT

The first observations of the rovibrational spectra of C–H stretching bands of propylene oxide (PO) with a high resolution infrared (IR) spectrometer are reported. Rotational spectra of four PO containing chiral molecular complexes, namely PO–Ne, PO–H<sub>2</sub>O, PO–(H<sub>2</sub>O)<sub>2</sub>, and PO–PO, were recorded using a pulsed molecular beam Fourier transform microwave spectrometer. *Ab initio* calculations were carried out to complement the data analysis. The spectroscopic and theoretical results were utilized to derive information about the structures of these complexes and the dynamics of their interactions.

Tentative assignment of the rovibrational spectra of PO monomer demonstrates the potential of the rapid scan mid-IR lead salt diode laser spectrometer for probing vibrationally excited states of chiral molecules. Refined rotational and centrifugal distortion constants were obtained for the PO–<sup>20</sup>Ne and PO–<sup>22</sup>Ne isotopomers. Two distinct structural conformers of both PO–H<sub>2</sub>O binary and PO–(H<sub>2</sub>O)<sub>2</sub> ternary complexes, namely *syn*- and *anti*-configurations, were detected experimentally. For PO–H<sub>2</sub>O, novel evidence for the stabilization effect of the methyl group to the intermolecular hydrogen bond is provided. The experimental observations showed that *syn*-PO–H<sub>2</sub>O was more favored over *anti*-PO–H<sub>2</sub>O, while the opposite was observed for PO–(H<sub>2</sub>O)<sub>2</sub>. The configuration preference observed in PO–(H<sub>2</sub>O)<sub>2</sub>, *anti* over *syn*, is in accordance with the prediction for PO in aqueous solution. This systematic study of complexes of PO with one and two water molecules clearly demonstrates how the stabilities of conformers can alter during the initial steps of hydration.

Six pairs of homo- and heterochiral conformers of PO dimer were predicted to be the most stable configurations. Rotational spectra of three homo- and heterochiral conformer pairs were measured and analyzed. The results suggest that the concerted effort of secondary hydrogen (H)-bonds, that is the  $O_{\text{epoxy}} \cdots \text{H}-\text{C}$  noncovalent interactions, can successfully lock the subunits in a particular orientation and that the overall binding strength is comparable to classic H-bonding. This is the first time that the homo- and the corresponding heterochiral dimers have been unambiguously identified via high resolution spectroscopy, as well as the essence of their interactions have been interpreted.

## PREFACE

This thesis is based on the research that I have done at the University of Alberta between September 2003 and August 2007. The references for the published work at this time, whether or not included in this thesis, are provided below for the sake of completeness.

Zheng Su and Yunjie Xu, “*Ab initio* study of chiral recognition in the propylene imine–hydrogen peroxide complex”, Physical Chemistry Chemical Physics, 7, 2554-2560 (2005).

Zheng Su, Waishun Tam and Yunjie Xu, “High resolution infrared spectroscopy and *ab initio* studies of the cyclopropane–carbon dioxide weak interaction”, Journal of Chemical Physics, 124, 024311/1-9 (2006).

### Chapter 4:

Zheng Su and Yunjie Xu, “Pulsed jet rotational spectra of the propylene oxide–neon dimer”, Journal of Molecular Spectroscopy, 232, 112-114 (2005).

Zheng Su, Qing Wen and Yunjie Xu, “Conformational stability of the propylene oxide–water adduct: direct spectroscopic detection of O–H···O hydrogen bonded conformers”, Journal of the American Chemical Society, 128, 6755-6760 (2006).

Zheng Su and Yunjie Xu, “Hydration of a chiral molecule: the gas phase study of the propylene oxide–(water)<sub>2</sub> ternary cluster”, Angewandte Chemie International Edition, 46, 6163-6166 (2007).

### Chapter 5:

Zheng Su, Nicole Borho and Yunjie Xu, “Chiral self-recognition: direct spectroscopic detection of the homochiral and heterochiral dimers of propylene oxide in the gas phase”, Journal of the American Chemical Society, 128, 17126-17131 (2006).

## ACKNOWLEDGMENTS

I wish to express my thanks to my supervisor Yunjie for her tremendous support over the past four years. There is no word to describe how much I have learned from her science-wise and how much she has impacted me morally. An old Chinese proverb says, “A supervisor for a day is like a parent for a lifetime.” I attribute my intellectual growth to my academic “parent”.

I also want to thank my colleagues in the Xu group, both former and present, for fostering many useful discussions. In particular, I would like to acknowledge Dr. W. Tam for his invaluable help during my research and Dr. N. Borho for her stimulating discussions.

The course of my research was greatly enhanced by the support of many people outside of the Xu group. In this respect, I would like to thank Dr. Wolfgang Jäger for his general guidance and offering his FTMW instrument for my main experimental results. I must also acknowledge his group members, R. Lehnig, W. Topic, J. Michaud, J. Landry, I. Leonov and C. Tanjaroon. Thanks especially to Dr. Q. Wen for her constant and generous support of my research work and for her friendship over the years. A special note of thanks goes to the staff at the Department’s machine shop and electronics shop. I am grateful to the friendship with Dr. A. Jordan, my teaching assistant coordinator, for her moral support and advice on many difficult occasions.

Finally I wish to acknowledge my parents, my sister and my husband for their endless love and belief in me.

# TABLE OF CONTENTS

Chapter	Page
<b>Chapter 1 Introduction</b>	<b>1</b>
References	9
<b>Chapter 2 Theoretical Background</b>	<b>12</b>
2.1 Overview of high resolution spectroscopy	12
2.1.1 Rotational spectroscopy	14
2.1.2 Vibrational spectroscopy	20
2.2 Theoretical methods: <i>Ab initio</i> calculations	23
2.2.1 The Born-Oppenheimer approximation	23
2.2.2 Level of theory	24
2.2.3 Basis set	25
2.2.4 Dissociation energy	26
References	28
<b>Chapter 3 Experimental Approaches</b>	<b>30</b>
3.1 Supersonic expansion	30
3.2 Fourier transform microwave spectrometer	32
3.3 Mid-infrared diode laser spectrometer	35
3.3.1 Lead salt diode laser	37
3.3.2 Optical path length enhancement	38
1) Beer-Lambert Law	38
2) Herriott-type multipass cell for reference gas	39
3) Astigmatic mirror multipass for molecular expansion	42
3.3.3 Spectrometer design	45
3.3.4 Laser modulation and detection schemes	48
1) Fast scan technique and data acquisition scheme	48
2) Frequency calibration	52

3) Measurement of rovibrational spectra	53
References	56
<b>Chapter 4 Spectroscopic Investigation of Propylene Oxide (PO) Monomer and PO–Ne van der Waals Dimer</b>	<b>59</b>
4.1 Introduction	59
4.2 Investigation of the PO monomer	61
4.2.1 Previous infrared studies of the C–H stretching modes of PO	61
4.2.2 <i>Ab initio</i> calculations	63
4.2.3 Experimental details	63
4.2.4 Rovibrational spectra	66
1) The tentative assignments of the $\nu_{1a}(\text{CH}_3)$ and $\nu_{2a}(\text{CH}_3)$ bands at $2974 \text{ cm}^{-1}$	67
2) The $\nu_s(\text{CH}_3)$ Band at $2942 \text{ cm}^{-1}$	69
3) Other bands	72
4.3 Rotational study of PO–Ne molecular complex	72
4.3.1 Rotational spectra	72
4.3.2 Discussion	73
4.4 Concluding remarks	76
References	78
<b>Chapter 5 Investigation of PO–(H<sub>2</sub>O)<sub>N=1-4</sub> Clusters: <i>Ab initio</i> Calculations and Rotational Spectra</b>	<b>81</b>
5.1 Introduction	81
5.2 <i>Ab initio</i> calculations	84
5.2.1 PO–H <sub>2</sub> O	84
1) Geometry optimizations and analysis	84
2) Dissociation energy	90
3) Spectroscopic constants	91
5.2.2 PO–(H <sub>2</sub> O) <sub>2</sub>	94



5.2.3 PO-(H <sub>2</sub> O) <sub>3</sub> and PO-(H <sub>2</sub> O) <sub>4</sub>	98
5.3 Experimental details	102
5.4 Spectral search and assignment	103
5.4.1 PO-H <sub>2</sub> O	103
5.4.2 PO-(H <sub>2</sub> O) <sub>2</sub>	107
5.5 Discussion	110
5.5.1 Structural analysis	110
1) PO-H <sub>2</sub> O	110
2) PO-(H <sub>2</sub> O) <sub>2</sub>	113
5.5.2 Conformational stability and hydrogen bonding strength	116
1) PO-H <sub>2</sub> O	116
2) PO-(H <sub>2</sub> O) <sub>2</sub>	120
5.6 Concluding remarks	121
References	123

<b>Chapter 6</b>	<b>Investigation of PO Dimers: <i>Ab initio</i> Calculations and Rotational Spectra</b>	<b>126</b>
6.1	Introduction	126
6.2	<i>Ab initio</i> calculations	129
6.2.1	Construction of the conformers	129
6.2.2	Geometry optimizations	130
6.2.3	Nomenclature	131
6.3	Spectral search and assignment	136
6.4	Discussion	142
6.4.1	Conformational geometries	142
6.4.2	Secondary hydrogen-bonds and conformational stability	145
6.4.3	Chirodiastaltic energies	148
6.5	Concluding remarks	151
	References	152

<b>Chapter 7</b>	<b>General Conclusions</b>	<b>155</b>
	References	160
Appendix 1	Tables of microwave transition frequencies measured for the PO containing complexes	161
Appendix 2	Tables of <i>ab initio</i> Cartesian coordinates for the PO containing complexes	176

## LIST OF TABLES

Table		Page
4-1	Frequency calculations of the C–H stretching modes of PO.	64
4-2	Spectroscopic constants of the ground and first vibrationally excited states of the C–H stretching modes of PO.	65
4-3	Rotational and centrifugal distortion constants of PO–Ne.	76
5-1	Calculated dipole-dipole interaction energies of PO–H <sub>2</sub> O.	89
5-2	Calculated dissociation energies of PO–H <sub>2</sub> O.	91
5-3	Calculated dissociation energies of D-substituted PO–water complex.	91
5-4	Calculated rotational constants and dipole moments of PO–H <sub>2</sub> O.	92
5-5	Comparison between experimental and calculated rotational constants of the ethylene oxide–water complex.	93
5-6	Calculated rotational constants of D-substituted PO–water complex.	93
5-7	Calculated harmonic frequencies of the vibrational bands of the water unit in the PO–water complex.	94
5-8	Calculated dissociation energies, rotational constants and dipole moment components of three conformers of PO–(H <sub>2</sub> O) <sub>2</sub> .	97
5-9	Calculated dissociation energies, rotational constants and electric dipole moment components of five conformers of PO–(H <sub>2</sub> O) <sub>3</sub> .	101
5-10	Calculated dissociation energies, rotational constants and dipole moment components of eight conformers of PO–(H <sub>2</sub> O) <sub>4</sub> .	101

5-11	Experimental spectroscopic constants of the parent and the deuterated isotopomers of PO–water complex.	105
5-12	Comparison between experimental and calculated rotational constants of PO–water complex.	106
5-13	Experimental spectroscopic constants of the two PO–(H <sub>2</sub> O) <sub>2</sub> conformers.	109
5-14	Hydrogen-bonding structural parameters of PO–H <sub>2</sub> O.	112
5-15	Structural parameters of two conformers of PO–(H <sub>2</sub> O) <sub>2</sub> .	115
5-16	Comparison of hydrogen-bonding force constants, stretching frequencies, and binding energies for several water–containing complexes.	117
6-1	Calculated dissociation energies, rotational constants and dipole moment components of PO dimer.	134
6-2	Comparison of calculated dissociation energies, rotational constants and dipole moment components of PO dimer using different basis sets.	135
6-3	Experimental spectroscopic constants of homochiral conformers of PO dimer.	141
6-4	Experimental spectroscopic constants of heterochiral conformers of PO dimer.	141
6-5	Comparison of experimental and calculated rotational constants of PO dimer.	143
6-6	Calculated secondary hydrogen-bonding structural parameters of PO dimer.	144
6-7	Experimental results and theoretical dissociation energies and chirodiastaltic energies of six conformers of PO dimer.	148

A1-1	Rotational transition frequencies of the PO–Ne complex.	162
A1-2	Rotational transition frequencies of PO–H <sub>2</sub> O.	164
A1-3	Rotational transition frequencies of the deuterated PO–water complex.	165
A1-4	Rotational transition frequencies of the PO–water system.	166
A1-5	Rotational transition frequencies of PO–(H <sub>2</sub> O) <sub>2</sub> .	167
A1-6	Measured rotational transition frequencies of enantiomeric PO.	170
A1-7	Measured rotational transition frequencies of racemic PO.	171
A1-8	Rotational transition frequencies of homochiral PO dimer.	173
A1-9	Rotational transition frequencies of heterochiral PO dimer.	175
A2-1	Cartesian coordinates of PO–H <sub>2</sub> O.	177
A2-2	Cartesian coordinates of PO–(H <sub>2</sub> O) <sub>2</sub> .	178
A2-3	Cartesian coordinates of PO dimer.	180

## LIST OF FIGURES

Figure		Page
2-1	Regions of the electromagnetic spectrum.	13
2-2	Correlation diagram of asymmetric rotor energy levels with those of the limiting prolate and oblate symmetric tops.	16
2-3	Illustration of <i>a</i> -, <i>b</i> -, and <i>c</i> -type transitions.	18
3-1	Diagram of the setup of the Fourier transform microwave spectrometer.	35
3-2	Schematic diagram of the Herriott multipass cell.	41
3-3	Picture of the Herriott multipass cell for reference gas.	42
3-4	Picture of the optical multipass between two astigmatic mirrors.	42
3-5	Theoretical pattern of the 90-pass configuration using two astigmatic mirrors.	43
3-6	Observed pattern of the 90-pass configuration on two astigmatic mirrors.	44
3-7	Experimental observation of the 182-spot configuration.	45
3-8	Schematic diagram of the rapid scan mid-infrared diode laser spectrometer.	46
3-9	Pulse sequence of the rapid scan data acquisition procedure.	50
3-10	Screen shot of the LabVIEW data acquisition operating program.	51
3-11	A portion of rovibrational spectrum of Ar-CO <sub>2</sub> near 2349 cm <sup>-1</sup> area.	54
3-12	A portion of rovibrational spectrum of C <sub>3</sub> H <sub>6</sub> -CO <sub>2</sub> near 2347 cm <sup>-1</sup> area.	55
4-1	Structure of the PO monomer and the PO-Ne complex.	60
4-2	Broadband low resolution Fourier transform infrared spectrum of PO.	62

4-3	Results for the CH <sub>3</sub> asymmetric stretching of PO.	68
4-4	Results for the CH <sub>3</sub> symmetric stretching of PO.	70
4-5	Rovibrational spectrum of PO in the area of 3000 cm <sup>-1</sup> .	71
4-6	Rotational spectra of PO- <sup>22</sup> Ne complex and PO monomer.	75
5-1	Optimized geometries of the <i>syn</i> -PO-H <sub>2</sub> O and <i>anti</i> -PO-H <sub>2</sub> O conformers.	86
5-2	The coordinate system for two dipoles $\mu_A$ and $\mu_B$ .	88
5-3	Optimized geometries of three conformers of PO-(H <sub>2</sub> O) <sub>2</sub> .	95
5-4	Optimized geometries of five conformers of PO-(H <sub>2</sub> O) <sub>3</sub> .	99
5-5	Optimized geometries of eight conformers of PO-(H <sub>2</sub> O) <sub>4</sub> .	100
5-6	Definition of the hydrogen-bonding parameters of PO-H <sub>2</sub> O.	111
6-1	Schematic view of PO binary conformers.	130
6-2	Optimized geometries of PO dimer.	132
6-3	Rotational transition spectrum of the PO dimer system.	140
6-4	Definition of hydrogen-bonding structural parameters of PO dimer.	143
6-5	Orientation of the six observed conformers of PO dimer.	150

## LIST OF SYMBOLS

Symbol	Meaning
$I_x, I_y, I_z$	moments of inertia in the molecular axis system
$I_a, I_b, I_c$	principal moments of inertia
$P_x, P_y, P_z$	planar moments of inertia
$A$	rotational constant with respect to $a$ -axis
$B$	rotational constant with respect to $b$ -axis
$C$	rotational constant with respect to $c$ -axis
$E_r$	rotational energy
$E_v$	vibrational energy
$J$	rotational quantum number
$K_a$	$K$ quantum number for prolate rotor
$K_c$	$K$ quantum number for oblate rotor
$\kappa$	asymmetry parameter
$D_J, D_{JK}, D_K, d_1, d_2$	quartic distortion constants for Watson's $S$ -reduction
$\Delta_J, \Delta_{JK}, \Delta_K, \delta_J, \delta_K$	quartic distortion constants for Watson's $A$ -reduction
$\mu_a, \mu_b, \mu_c$	dipole moments with respect to the principal axes
$\omega$	harmonic vibration frequency
$\nu$	vibrational quantum number
$x_e$	anharmonicity constant
$I_0$	incident laser intensity
$I_l$	exit laser intensity
f	lens focusing distance
fsr	free spectral range
$\sigma$	standard deviation
$R_{CM}$	intermolecular center-of-mass separation
$E_{int}$	interaction energy
$D_0$	dissociation energy
ZPE	zero-point vibrational energy
$\tau, \phi, \theta$	binding angles
$k_s$	force constant
$\mu$	reduced mass of molecular complex
$\Delta E_{chir}$	chirodiastaltic energy
$RR, SS$	homochiral dimer
$RS, SR$	heterochiral dimer



\*\*\*\*\*

## CHAPTER 1

### INTRODUCTION

\*\*\*\*\*

The concept of chirality dates back to 1848 when Louis Pasteur discovered the asymmetry of crystals. Pasteur noticed that the crystals came in two asymmetric forms that were mirror images of one another and solutions of one form rotated linearly polarized light clockwise, while the other form rotated light counterclockwise.<sup>1</sup> He deduced that the molecule in question was asymmetric and could exist in two different forms that resemble one another as would left and right hands. This was the first time anyone had demonstrated experimentally the phenomenon of chirality. 36 years later, Lord Kelvin named this asymmetry property *chirality* (from the Greek word for a hand):

*“I call any geometric figure, or group of points, chiral, and say it has chirality, if its image in a plane mirror, ideally realized, cannot be brought to coincide with itself.”<sup>2</sup>*

In chemistry, a chiral entity and its mirror image are called enantiomers. Chirality in chemistry is not merely a macroscopic concept but also has significant impact at the microscopic level considering the stunning fact that most of biochemistry is chiral.<sup>3</sup> Proteins, DNA, amino acids, sugars and almost all natural products possess the property of chirality. Indeed, a characteristic hallmark of life is

its homochirality: nature selects left-handed amino acids and right-handed sugars for life. Fischer in 1894 introduced the '*lock and key*' principle to explain the specificity of enzyme reactions.<sup>4</sup> This metaphor vividly describes the interactions taking place in nearly all biological processes: chiral recognition – a chiral molecule can recognize the difference between the two handed forms of another chiral molecule. Moreover, this recognition may result in a different preference for interactions depending on the environment. The best example would be our hands: a right hand prefers to shake another right hand in a formal meeting but would hold a left hand if two people are standing side by side.

Though homochirality of life is a fascinating phenomenon, its origin has been a puzzle for centuries. Additionally, the importance of chiral recognition in biological systems is underlined by the fact that most biological receptors and membranes are chiral and “wrong hand shaking” can have destructive effects. A classic case was the drug, thalidomide, which was developed in 1950s to prevent morning sickness during pregnancy. Thalidomide was sold in a racemic mixture containing equal amount of two enantiomers. One enantiomer of thalidomide prevented the proper growth of the fetus, resulting in birth defects in thousands of children around the world.<sup>5</sup> Due to the possibly disastrous consequences of using racemic mixtures, about 50 of the top 100 drugs today are marketed as single enantiomers, and 80 percent of drugs now entering the drug development process are single enantiomers.<sup>6</sup>

To fully understand molecular recognition effects in these complicated macroscopic processes, we have to start from the microscopic level and unveil the mystery step by step. One key question in chiral recognition is how the intermolecular

forces come together in a concerted way to enable a chiral molecule to differentiate another chiral entity and its mirror image. Therefore the ultimate goal of my thesis work is to understand the chiral discriminating forces at play in a model chiral molecular system. In order to achieve this goal, much preparation work needs to be completed to pave the road. The strategy was to begin with a chiral monomer, gradually moving forward to complexes of this monomer with one atom, one small molecule and then eventually with another chiral entity or a copy of the starting molecule itself.

Another important aspect at the macroscopic level is the interaction between the chiral entities and their surrounding environment, such as solute-solvent interactions. In particular, the interactions between water and chiral molecules are of significant interest since hydrogen bonding governs the solvation processes in many aqueous environments.<sup>7</sup> Fundamental knowledge of the underlying mechanism for the solvation of chiral molecules in water is a prerequisite for understanding of complex interactions in aqueous media. Therefore, water was chosen as a most abundant solvent to investigate these chiral solute-solvent interactions. This systematic approach to chiral discrimination interactions will allow me to gain detailed knowledge of complicated intermolecular interactions on a molecular basis. This is crucial for the fundamental understanding of macroscopic chirality in molecular systems.

The pioneering work of Johannes Diderik van der Waals<sup>8</sup> in the late 19th century established the fundamental connection between the properties of bulk matter and intermolecular forces. Since the time of van der Waals, our understanding of

intermolecular interactions has continued to improve. In condensed phases, chiral molecules may recognize suitable chiral partners through short-range electrostatic, dipole-dipole and/or steric interactions to form molecular complexes. Chemical properties of molecular complexes are probed by various spectroscopic methods to gain valuable insights into these interactions. Due to the different structures of homo- and heterochiral complexes, these conformers can be spectroscopically distinguished. However, the presence of solvent may hinder or affect such differentiation between these complexes.<sup>9</sup> A method to eliminate this undesired interference and to evaluate the intrinsic interactions is to probe the molecular recognition mechanism in the gas phase for a microscopic model system. By using laser-induced fluorescence excitation spectroscopy, Zehnacker and co-workers<sup>10</sup> provided the first example of chiral discrimination at the molecular level in isolated solute-solvent pairs (a naphthalene compound in the presence of alcoholic solvents). This opened an interesting window to explore the stereochemical effects in van der Waals complexes. Their work, in essence, drew attention to the importance of short range interactions in chiral discrimination in a non-condensed phase. Subsequently, more spectroscopic studies have been carried out on the phenomenon of chiral recognition by using ultraviolet (UV)/infrared (IR) double resonance,<sup>11, 12</sup> resonance-enhanced multiphoton ionization,<sup>13, 14</sup> and broad-band Fourier transform (FT) IR spectroscopy.<sup>15, 16, 17, 18</sup> With these techniques, homo- and heterochiral complexes can be identified and structural information can be extracted by comparing systematic experimental work.

One common problem with the studies mentioned above is that detailed structural information is limited due to the absence of rotationally resolved spectra.

Alternatively, high resolution spectroscopy can provide information about the energy level spacing in the molecular complexes which is sensitive to the subtlest differences in the structures. Therefore, high resolution spectroscopy is an attractive and indispensable technique to determine the three-dimensional structure of chiral entities and to probe the role of various interactions in chiral recognition. For example, Fourier-transform microwave (FTMW) spectroscopy is well known for its capability to distinguish structural changes and determine small energy differences in conformers.<sup>19</sup> The first high resolution spectroscopic study of a chiral molecular complex, butan-2-ol dimer, was investigated by FTMW spectroscopy,<sup>20</sup> before the FTIR spectroscopic studies.<sup>15, 16, 17, 18</sup> A few years afterwards, Howard's group at Oxford University measured the first rotational spectrum of a transient chiral system containing three conformations of the ethanol dimers.<sup>21</sup> Those are induced chiral dimers as ethanol can be a chiral molecule under some circumstances. The hydroxyl group can either be in one of the two equivalent positions gauche to the methyl group. These two gauche forms can interchange rapidly in an isolated monomer. However, if the hydroxyl group is involved in a hydrogen bond as in ethanol dimer, this interconversion can be quenched leading to experimentally differentiable forms of the dimer.

While FTMW spectroscopy can determine the ground state structure precisely, rotationally resolvable IR spectroscopy can investigate vibrationally excited states. Small chiral molecules, such as fluorooxirane<sup>22</sup> and thiran-1-oxide,<sup>23, 24</sup> have been investigated by gas phase IR spectroscopy with rotational resolution. Rotational and centrifugal distortion constants of both vibrationally ground and first excited states

were determined from their high resolution IR spectra. Despite their great potential, the combination of these two powerful yet complementary techniques has so far only been utilized in studies of single monomers, such as bromochlorofluoromethane (CHBrClF) – a model of the simplest chiral molecule.<sup>25</sup> The few spectroscopic data of chiral molecular systems highlights the fact that assignments of rotationally and/or rovibrationally resolved spectra of chiral molecular systems are still a daunting task.

Experimental studies of chiral molecules and/or molecular complexes are complicated by the large number of potential structural conformers and dense spectral patterns associated with these asymmetric molecules. Therefore, structural information is challenging to extract from the obtained spectroscopic data. High level *ab initio* calculations are essential to guide initial spectral searches and to interpret the observed spectroscopic data. One can in turn use the experimental analysis to judge the quality of the theoretical predictions and develop appropriate models for further calculations. In parallel to the experimental efforts, there is a small number of theoretical investigations that are dedicated to the studies of chiral recognition effects. Portmann *et al.* carried out detailed high level quantum chemistry studies of the interactions of oxirane and its derivatives with hydrogen peroxide.<sup>26</sup> Alkorta and co-workers used density functional theory and *ab initio* methods to study chiral discrimination in a number of hydrogen-bonded complexes consisting of compounds with axial chirality, such as  $\alpha$ -amino alcohols,<sup>27</sup> pyrrole derivatives,<sup>28</sup> hydrazine,<sup>29</sup> and performic acid.<sup>30</sup> However, there are very limited high resolution spectroscopic studies of these chiral molecular systems to confirm these calculations.

The aim of this thesis work is to probe chiral molecular systems using *ab initio* calculations and high resolution spectroscopic methods to investigate microscopic chirality. As a starting point, size and conformational flexibility of the concerned chiral molecule was considered to ensure the theoretical study of the system computationally affordable and the spectroscopic investigation practically amenable. Propylene oxide (PO), C<sub>3</sub>H<sub>6</sub>O, was chosen for my studies because of its chemical stability and structural rigidity. It is an ideal chiral building block as it is one of the simplest cyclic ether chiral molecules and can be regarded as truly “organic”. The presence of the epoxy oxygen atom is appealing as a potential proton acceptor in primary hydrogen bonding. PO has only one stereogenic centre, namely the carbon atom bonded with the methyl group. This molecule first attracted attention decades ago due to theoretical interests on the effects of hindered rotation of a methyl group.<sup>31,32</sup> PO has also been investigated by FTIR spectroscopy. The vibrational bands of the methyl group torsion, symmetrical and antisymmetrical stretching were observed by Winther and Hummel.<sup>33</sup> Afterwards, the ground state structure of PO was well determined by Kuczkowski and Imachi.<sup>34</sup> Recently, Caminati and co-workers have carried out a series of studies on the van der Waals complexes of PO with rare gas (Rg) atoms (Rg = Ne,<sup>35</sup> Ar,<sup>36</sup> Kr<sup>37</sup>) using millimeter wave spectroscopy. The correct identifications of the lowest energy structures of these complexes were only achieved through a detailed comparison between the theoretical and experimental results. This emphasizes the challenges associated with spectroscopic characterizations of PO containing complexes and the necessity of high level quantum chemistry calculations in assisting experimental search and analysis.

The remainder of this thesis is divided into six chapters. Chapter 2 provides a general overview of high resolution spectroscopy in the microwave and infrared region and of the methods used for *ab initio* calculations. Chapter 3 describes the experimental setup of FTMW spectroscopy and describes in detail the construction of a high resolution IR spectrometer. Chapter 4 reports the first observation of rovibrational spectra for four C–H stretching bands of the PO monomer. Measurements of rotational transitions of the PO–<sup>20</sup>Ne and PO–<sup>22</sup>Ne complexes using the FTMW spectrometer are discussed as the base work for later chapters. Chapter 5 is devoted to the rotational spectroscopic and high level *ab initio* studies of PO sequentially solvated by a few water molecules in the gas phase. Chapter 6 describes the detailed studies on the chiral self-recognition in PO dimer. A summary of the experimental and theoretical results obtained for the PO containing complexes is given in Chapter 7 along with several considerations for future research in this field.



## References

---

1. Pasteur, L. *Ann. Chim. Phys.* **1848**, III, 24, 442.
2. Lord Kelvin *Baltimore Lectures (1884) on Molecular Dynamics and the Wave Theory of Light*, Clay and Sons: London, **1904**, p. 449.
3. Stryer, L. *Biochemistry*, 4th ed., W. H. Freeman and Co.: New York, **1995**.
4. Fischer, E. *Ber. Dtsch. Chem. Ges.* **1894**, 27, 2985.
5. Blaschke, G., Kraft, H. P., Fickentscher, K., Köhler, F. *Drug Res.* **1979**, 29, 1640.
6. Stinson, S. C. *Chemical and Engineering News* **1998**, 76, 38.
7. Jeffrey, J. A.; Saenger, W. *Hydrogen Bonding in Biological Structures*, Springer-Verlag: Berlin, **1991**.
8. Van der Waals, J. D. *On the Continuity of the Gaseous and Liquid States*, North Holland, Amsterdam, **1988**.
9. Arnett, E. M.; Zingg, S. P. *J. Am. Chem. Soc.* **1981**, 103, 1221.
10. Al-Rabaa, A. R.; Bréhéret, E.; Lahmani, F.; Zehnacker-Rentien, A. *Chem. Phys. Lett.* **1995**, 237, 480.
11. Al-Rabaa, A. R.; Le Barbu, K.; Lahmani, F.; Zehnacker-Rentien, A. *J. Phys. Chem. A* **1997**, 101, 3273.
12. Le Barbu, K.; Brenner, V.; Millié, Ph.; Lahmani, F.; Zehnacker-Rentien, A. *J. Phys. Chem. A* **1998**, 102, 128.
13. Piccirillo, S.; Bosman, C.; Toja, D.; Giardini-Guidoni, A.; Pierini, M.; Troiani, A.; Speranza, M. *Angew. Chem, Int. Ed.* **1997**, 36, 1729.
14. Latinia, A.; Toja, D.; Giardini-Guidoni, A.; Piccirillo, S.; Speranza, M. *Angew. Chem, Int. Ed.* **1999**, 38, 815.
15. Borho, N.; Häber, Th.; Suhm, M. A. *Phys. Chem. Chem. Phys.* **2001**, 3, 1945.
16. Borho, N.; Suhm, M. A. *Phys. Chem. Chem. Phys.* **2002**, 4, 2721.
17. Borho, N.; Suhm, M. A. *Org. Biomol. Chem.* **2003**, 1, 4351.

- 
18. Adler, T. B.; Borho, N.; Reiher, M.; Suhm, M. A. *Angew. Chem. Int. Ed.* **2006**, *45*, 3440.
  19. Xu, Y.; Jäger, W. *J. Chem. Phys.* **1997**, *107*, 4788.
  20. King, A. K.; Howard, B. J. *Chem. Phys. Lett.* **2001**, *348*, 343.
  21. Hearn, J. P. I.; Cogley, R. V.; Howard, B. J. *J. Chem. Phys.* **2005**, *123*, 134324.
  22. Hollenstein, H.; Luckhaus, D.; Pochert, J.; Quack, M.; Seyfang, G. *Angew. Chem. Int. Ed.* **1997**, *36*, 140.
  23. Gross, H.; He, Y.; Jeitziner, C.; Quack, M.; Seyfang, G. *Ber. Bunsen-Ges. Phys. Chem.* **1995**, *99*, 358.
  24. Gross, H.; Grassi, G.; Quack, M. *Chem. Eur. J.* **1998**, *4*, 441.
  25. Bauder, A.; Beil, A.; Luckhaus, D.; Müller, F.; Quack, M. *J. Chem. Phys.* **1997**, *106*, 7558.
  26. Portmann, S.; Inauen, A.; Lüthi, H. P.; Leutwyler, S. *J. Chem. Phys.* **2000**, *113*, 9577.
  27. Alkorta, I.; Elguero, J. *J. Am. Chem. Soc.* **2002**, *124*, 1488.
  28. Picazo, O.; Alkorta, I.; Elguero, J. *J. Org. Chem.* **2003**, *68*, 7485.
  29. Picazo, O.; Alkorta, I.; Elguero, J.; Sundberg, M. R.; Valo, J. *Eur. J. Inorg. Chem.* **2007**, *2*, 324.
  30. Alkorta, I.; Elguero, J. *J. Chem. Phys.* **2002**, *117*, 6463.
  31. Swalen, J. D.; Herschbach, D. R. *J. Chem. Phys.* **1957**, *27*, 100.
  32. Herschbach, D. R.; Swalen, J. D. *J. Chem. Phys.* **1958**, *29*, 761.
  33. Winther, F.; Hummel, D. O. *Spectrochimica Acta* **1968**, *25A*, 417.
  34. Imachi, M.; Kuczkowski, R. L. *J. Mol. Struct.* **1982**, *96*, 55.
  35. Blanco, S.; Maris, A.; Melandri, S.; Caminati, W. *Mol. Phys.* **2002**, *100*, 3245.
  36. Blanco, S.; Maris, A.; Millemaggi, A.; Caminati, W. *J. Mol. Str.* **2001**, *612*, 309.

---

37. Blanco, S.; Melandri, S.; Maris, A.; Caminati, W.; Velino, B.; Kisiel, Z. *Phys. Chem. Chem. Phys.* **2003**, *5*, 1359.

\* \* \* \* \*

## CHAPTER 2

### THEORETICAL BACKGROUND

\* \* \* \* \*

The current chapter is divided into two parts. The first section gives a general overview of high resolution spectroscopy in the microwave and infrared regions and introduces the spectroscopic constants that will be used throughout this thesis. Secondly, the methods for *ab initio* calculations applied within the scope of this thesis are briefly described.

#### 2.1 Overview of high resolution spectroscopy

Molecular spectroscopy is the study of the interaction of light with matter. Light is an electromagnetic wave which can be represented by plane waves. Figure 2-1 shows the range of electromagnetic radiation from the spectroscopic perspective. There are different experimental techniques pertaining to each region of the electromagnetic spectra. The electromagnetic spectrum is divided into the following regions: radio, microwave (MW), millimeter, infrared (IR), visible, ultraviolet, X-ray and  $\gamma$ -ray regions. For example, energy differences between rotational states are on the order of several GHz. Therefore, pure rotational transitions are observed in the MW frequency range (1-100 GHz). My thesis will focus on the MW and IR regions of electromagnetic spectrum, specifically utilizing rotational and vibrational

spectroscopy to accurately probe molecular structure of chiral complexes. To fulfill this purpose, high resolution techniques are needed to resolve complicated spectra on the rotational level. This will provide accurate spectroscopic data for structural investigations, where quantum mechanics is necessary to interpret the data. For example, the narrow linewidths of diode lasers ( $\sim 10^{-5} \text{ cm}^{-1} \approx 0.3 \text{ MHz}$ ) in the mid-IR region allows for the measurement of rovibrational spectrum, in contrast to FTIR spectroscopy with resolution  $\sim 0.1 \text{ cm}^{-1}$ .

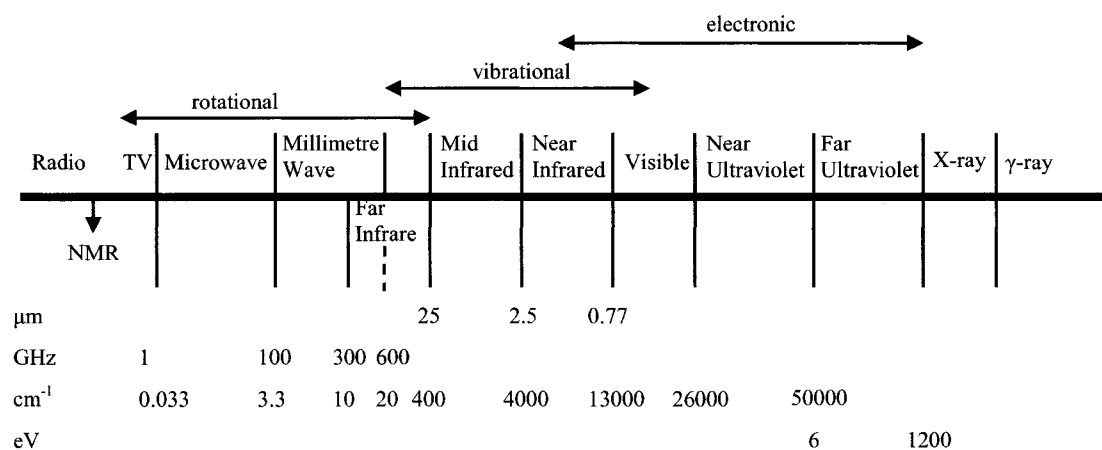


**Figure 2-1** Regions of the electromagnetic spectrum (redrawn from Figure 3.1 in Ref.2).

As this thesis work mainly concerns rotational and vibrational states of molecular systems, the corresponding theory within rotational spectroscopy and vibrational spectroscopy is briefly described in Sections 2.1.1 and 2.1.2. The details can be found in several books: Ref.1, 2, 3, 4.

### 2.1.1 Rotational spectroscopy

In this section, I will first separate various molecules into classes according to their principal moments of inertia, and then illustrate the quantization of rotational energy levels. Further, the most important spectroscopic constants will be introduced. Finally, the selection rules governing pure rotational transitions will be listed.

Each nucleus in a molecule is taken to be a point mass within any Cartesian axis system whose origin is at the centre of mass of the set of nuclei. The moments of inertia about  $x$ -,  $y$ -, and  $z$ - axes are given by:

$$\begin{aligned} I_x &= \sum_i m_i (y_i^2 + z_i^2) \\ I_y &= \sum_i m_i (x_i^2 + z_i^2) \\ I_z &= \sum_i m_i (x_i^2 + y_i^2) \end{aligned} \quad (2.1)$$

Alternative scheme labels the moments of inertia in the principle axis system, where the axes are labelled as  $a$ ,  $b$ , and  $c$  according to:

$$I_c \geq I_b \geq I_a \quad (2.2)$$

Molecules can be identified into classes according to their principal moments of inertia. A linear molecule has:

$$I_c = I_b > I_a = 0 \quad (2.3)$$

A symmetric rotor or symmetric top molecule has two equal moments of inertia and can be separated into two groups. A molecule is a prolate symmetric rotor if:

$$I_c = I_b > I_a \quad (2.4)$$

A molecule is an oblate symmetric rotor if:

$$I_c > I_b = I_a \quad (2.5)$$

An asymmetric rotor molecule has no equal principal moments of inertia:

$$I_c \neq I_b \neq I_a \quad (2.6)$$

The rotational constants  $A$ ,  $B$  and  $C$  in the unit of energy are related to the moments of inertia by:

$$A = \frac{\hbar^2}{2I_a}; B = \frac{\hbar^2}{2I_b}; C = \frac{\hbar^2}{2I_c} \quad (2.7)$$

For a rigid diatomic (linear) molecule, the rotational kinetic energy can be expressed by:

$$E_r = BJ(J+1) \quad (2.8)$$

The quantity  $J$ , which can take integer values from zero upwards, is a good quantum number which specifies rotational energy levels. For symmetric rotors, there are angular momenta along more than one inertial axis. Solving the Schrödinger equation for a prolate symmetric top results in:

$$E_r = BJ(J+1) + (A-B)K^2 \quad (2.9)$$

where the quantum number  $K$  represents the projection of the total angular momentum onto the principal symmetry axis, and can take the values  $J, J-1, J-2 \dots 0$ .

The solution to the Schrödinger equation for asymmetric top molecules does not give an analytical format of energy expression as compared to that for linear and symmetric top molecules. Thus, there is no closed expression for the asymmetric rotor wave functions. However, they may be represented by a linear combination of symmetric rotor functions. Conventionally, the rotational levels are labelled by  $J_{KaKc}$ ,

where  $K_a$  and  $K_c$  represent the  $K$  values of the limiting prolate and oblate symmetric tops, respectively. However, in contrast with  $J$  and  $K$ ,  $K_a$  and  $K_c$  are no longer good quantum numbers for asymmetric top molecules. Figure 2-2 shows the correlation diagram of the asymmetric rotor energy levels with respect to the prolate and oblate symmetric

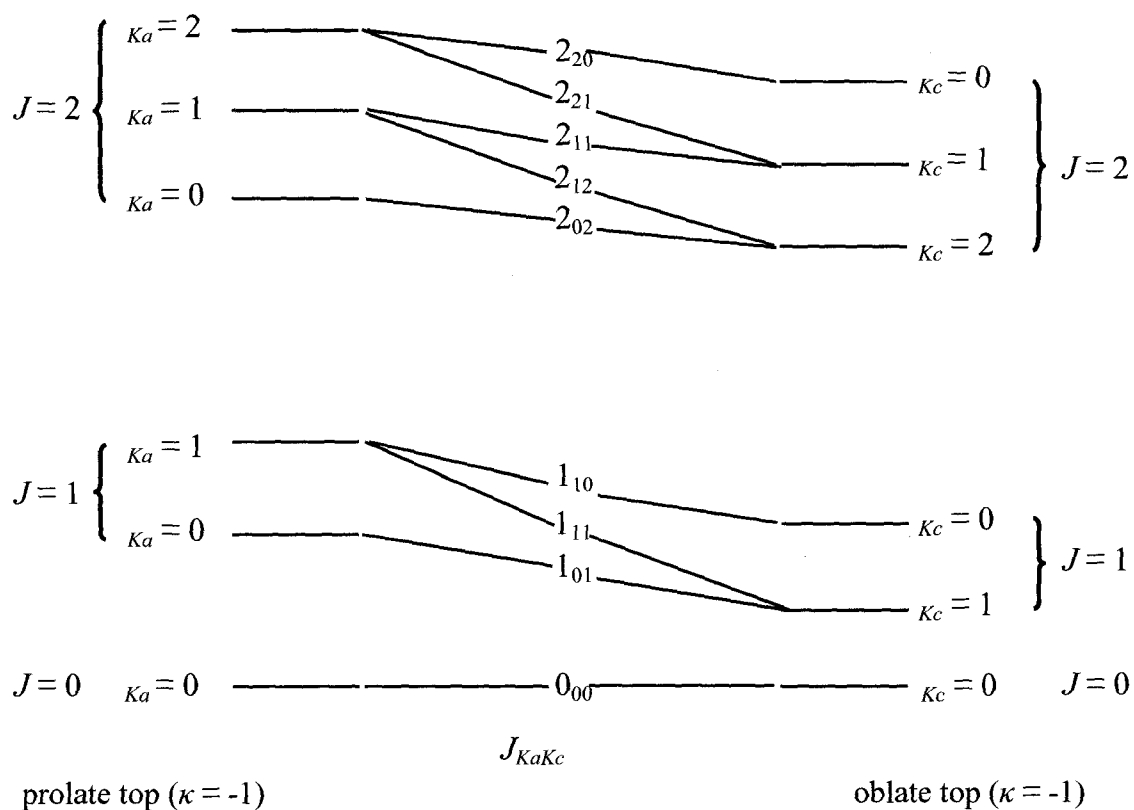


**Figure 2-2** A schematic diagram showing the correlation of asymmetric rotor energy levels with those of the limiting prolate and oblate symmetric tops (redrawn from Figure 6.33 of Ref. 1).

The degree of asymmetry can be quantified by an asymmetry parameter,  $\kappa$ , which equals -1 for a prolate top and +1 for an oblate top and is obtained by the following equation:



$$\kappa = \frac{2B - A - C}{A - C} \quad (2.10)$$

For example,  $\kappa$  is equal to zero for spherical tops. For the propylene oxide (PO)–(H<sub>2</sub>O)<sub>2</sub> complex, whose  $\kappa$  is equal to -0.75, is more asymmetric than the PO–H<sub>2</sub>O system with a  $\kappa$  value very close to -1 (near prolate top). There are several ways to identify the matrix elements of Hamiltonian operator for asymmetric rotor. Each identification has a particular advantage for certain ranges of  $\kappa$ : For an asymmetric oblate type top with  $\kappa$  close to -1, the  $I'$  type of matrix representation is the most useful form to employ for the Hamiltonian operator. The detailed description of the asymmetric rotor model can be found in the book by Gordy and Cook.<sup>4</sup>

The general requirement for rotational transitions is that the molecule must have a permanent dipole moment ( $\mu \neq 0$ ).

$$M = \int \psi_j \mu \psi_j d\tau \quad (2.11)$$

where  $M$  is the intensity of a pure rotational transition. The studies in this thesis mainly deal with chiral molecules which are asymmetric rotors and have  $C_1$  symmetry. Therefore, the specific selection rules in asymmetric tops are described here. An asymmetric rotor molecule has three dipole moment components  $\mu_a$ ,  $\mu_b$ , and  $\mu_c$  along each principal axis. Each non-zero component of the dipole moment allows for a certain set of transitions to be possible. The selection rule governing the changes in  $J$  is  $\Delta J = -1, 0, +1$ , which are labelled conventionally as  $P$ -,  $Q$ -, and  $R$ -branches, respectively. In addition, if  $\mu_a \neq 0$  and  $\mu_b = \mu_c = 0$ , then the molecule is said to obey  $a$ -type selection rules, with  $\Delta K_a = 0$ ,  $\Delta K_c = \pm 1$ ; if  $\mu_b \neq 0$ , then transitions with  $\Delta K_a = \pm 1$ ,  $\Delta K_c = \pm 1$  are allowed; if  $\mu_c \neq 0$ , the transitions with  $\Delta K_a = \pm 1$ ,  $\Delta K_c = 0$  are allowed.

The three possible types of transitions are illustrated in Figure 2-3. For example, the PO–Ne complex has non-zero dipole moments along the three principal axes, and as a result *a*-, *b*-, and *c*-type rotational transitions can all be observed.

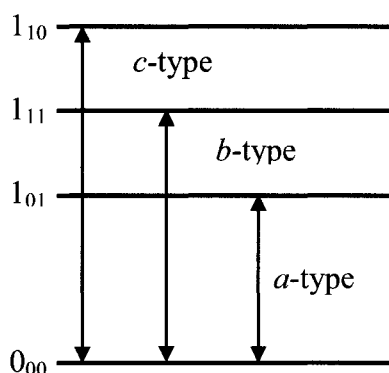


**Figure 2-3** Illustration of *a*-, *b*-, and *c*-type transitions (redrawn from Figure 6.36 of Ref. 1).

All of the above discussions are based on the rigid rotor approximation. However, a molecule is not strictly a rigid rotor as the chemical bonds can stretch and contract. The non-rigidity of the bonds results in the nuclei moving outwards from the centre of mass due to centrifugal forces during rotations. Therefore, centrifugal distortion constants such as quartic distortion,  $D_J$ , and sextic constant,  $H_J$ , are included in the energy expressions of diatomic or linear molecules to describe a non-rigid molecule:

$$E_r = BJ(J+1) - D_J[J(J+1)]^2 + H_J[J(J+1)]^3 \quad (2.12)$$

The centrifugal distortion constants are useful in estimating stretching force constants. The quartic distortion constant  $D_J$  is also related to  $B_0$  (ground state rotational constant) and the vibration frequency  $\omega$  by the Kratzer relationship:<sup>5</sup>

$$D_J = \frac{4B_0^3}{\omega^2} \quad (2.13)$$

The theory of centrifugal distortion is considerably more complex for asymmetric rotors than for linear or symmetric top molecules. The rotational Hamiltonian of an asymmetric top molecule contains more parameters than can be determined from the observed energy levels. Therefore, it is transformed to a reduced Hamiltonian, referred as *Watson's Hamiltonian*, which is suitable for fitting to observed energies.<sup>6</sup> There are two reduced Hamiltonians: a symmetric top reduction (*S*) for very slightly asymmetric tops ( $|\kappa|$  close to 1) or an asymmetric top reduction (*A*) for the asymmetric tops. Combinations of centrifugal distortion constants, i.e.  $D_J, D_{JK}, D_K, d_1, d_2$  for Watson's *S*-reduction or  $\Delta_J, \Delta_{JK}, \Delta_K, \delta_J, \delta_K$  for Watson's *A*-reduction, are used to describe centrifugal distortion.<sup>7</sup> For example, the former set was used for PO–H<sub>2</sub>O, and the later one for PO–(H<sub>2</sub>O)<sub>2</sub>.

One of the main applications of rotational spectroscopy is the determination of the ground state molecular structure. For a diatomic molecule of known atomic masses, the separation of lines in a rotational spectrum can be related directly to the rotational constants, which can be used to derive bond lengths. For an  $N$ -atom non-linear molecule ( $N > 2$ ), there are  $3N-6$  structural parameters and therefore,  $3N-6$  rotational constants are needed to derive the structure. This implies that one set of three rotational constants is inadequate for structural determination of polyatomic molecules.

Additionally, the effect of isotopic substitution on rotational transitions is also essential for structural derivation. When a particular atom in a molecule is replaced by its isotope, there is a change in total mass, hence in the moment of inertia (refer to Equation 2.1). If there is no appreciable change in the internuclear distance, the change in the rotational constants (refer to Equation 2.7) for the molecule upon isotopic substitution can be used to derive bonding parameters related to that particular atom. This method will be demonstrated in Chapter 5 where hydrogen and oxygen atoms are isotopically substituted in PO–H<sub>2</sub>O and PO–(H<sub>2</sub>O)<sub>2</sub> systems, respectively. For example, the PO–H<sub>2</sub>O complex needs six additional structural parameters to describe the relative orientation of the two monomers assuming the structures of water and PO remain unchanged upon complex formation. By analysing the rotational spectra of normal and deuterium-substituted isotopomers, four sets of rotational constants were fitted, from which the values of the six parameters were derived. The derivation of the three rotational constants, *A*, *B*, and *C* from rotational spectra is a multi-dimensional problem and an iterative procedure is needed. A special fitting program was utilized in Chapters 4, 5, and 6 to obtain the rotational constants from measured rotational transition frequencies.

### **2.1.2 Vibrational spectroscopy**

A molecular system must have a permanent dipole moment to be probed by pure rotational spectroscopy. Spectroscopic studies of molecules possessing non-permanent dipole moment, for example, *C<sub>i</sub>* symmetry species can be performed using vibrational spectroscopy, which only requires change of dipole moments during the

course of vibrational motions. In principal, rotationally-resolved vibrational spectroscopy can provide accurate information about rotational energy levels in both ground and vibrationally excited states. In this section, quantization of vibrational energy will be described briefly. First, the harmonic oscillator approximation for describing diatomic molecules will be introduced. Subsequently, molecules undergoing vibration and rotation simultaneously will be described.

Simplistically speaking, the vibration of a diatomic molecule can be described by a harmonic oscillator of two particles of point mass connected by a spring with a force constant:

$$\nu = \frac{1}{2\pi} \sqrt{\frac{k}{\mu}} \quad (2.14)$$

This approximation leads to vibrational energy levels in units of frequency given by:

$$E_v = \omega_e \left( v + \frac{1}{2} \right) \quad (2.15)$$

where  $\omega_e$  is the equilibrium vibration frequency, related to the force constant  $k$  and reduced mass  $\mu$ . The vibrational quantum number  $v$  can take any positive integer value including zero. In particular, the lowest vibrational energy is  $\frac{1}{2} \omega_e$ , which is known as the zero-point energy. The requirement for vibrational transitions is that the electric dipole moment of the molecule must change in the course of the vibrational motion. For example, homonuclear diatomics are infrared inactive as stretching of the bond does not alter the dipole moment of the molecule. The vibrational selection rule is  $\Delta v = \pm 1$ .

Certainly, real molecules do not follow exactly the laws of harmonic motion. An anharmonicity constant,  $x_e$ , which is normally small and positive, can be introduced to describe the motion quantitatively:

$$E_v = \omega_e(v+1/2) - x_e\omega_e(v+1/2)^2 \quad (2.16)$$

The anharmonicity brings the vibrational levels more closely together with increasing  $v$ . The anharmonic oscillator selection rule is  $\Delta v = \pm 1, \pm 2, \pm 3, \dots$ .

As discussed in the previous section, pure rotational spectroscopy probes transitions between rotational energy levels of vibrational ground state. In rovibrational spectroscopy, we observe the transitions between the stacks of rotational energy levels associated with two different vibrational levels. Rovibrational transitions of asymmetric tops can also be classified as  $a$ -,  $b$ -, and  $c$ -type, depending on the orientation of the transition dipole moment relative to the principal axes. The selection rules are similar as in rotational spectroscopy. It is common practice to label rovibrational transitions of asymmetric tops P, Q, R as the main letter for  $\Delta J = (J' - J'') = -1, 0, +1$ , respectively. Here  $J'$  and  $J''$  represent the rotational level within the vibrationally higher and lower states, respectively. The value of  $\Delta K_a$  is taken as a preceding superscript and the vibrationally lower state  $K_a$  as a following subscript. For example, the label  ${}^P Q_1$  represents the stack of transitions:  $J_{K_a K_c} - J'_{K_a' K_c'} = 101-110; 202-211; 303-312; \text{etc.}$

Considering a molecule containing  $N$  atoms, the position of each atom can be referred to by specifying three Cartesian coordinates. Thus, the total number of coordinates is  $3N$  and the molecule has  $3N$  degrees of freedom. Among the movements in three-dimensional space, three are translational and three are rotational

for non-linear molecules. Therefore, a non-linear  $N$ -atomic molecule can have  $3N-6$  fundamental vibrational motions. Each motion can be labelled as either symmetric or antisymmetric if applicable. It is convention to label the modes in decreasing frequency within their symmetry type as  $\nu_1, \nu_2, \nu_3$ , etc. The PO molecule,  $C_3H_6O$ , consists of 10 atoms, and possesses 24 modes. The six C–H stretching modes have the largest vibrational frequency, around  $3000\text{ cm}^{-1}$ .

## 2.2 Theoretical methods: *Ab initio* calculations

High resolution spectroscopy is used to obtain accurate structural information, which in turn provides impetus for theory to reproduce and account for the information. The real test of any quantum mechanical theory lies in its ability to reproduce the experimental data and provide accurate predictions for unknown systems. High level *ab initio* calculations were carried out in this thesis work to aid the search and analysis of the anticipated dense high resolution spectra of these chiral complexes.

### 2.2.1 Born-Oppenheimer approximation

In quantum chemistry, the computation of the energy of any molecule other than the lightest one,  $H_2$  is a formidable task. For example, the proplene oxide (PO) molecule consists of 10 nuclei and 32 electrons. The time independent Schrödinger equation contains 126 variables – the coordinates of the nuclei and the electrons. The Born-Oppenheimer (BO) approximation makes it possible to calculate the wavefunction and obtain the energy in two steps.<sup>8</sup> In the first step the nuclear kinetic

energy is neglected based on the fact that the heavy nuclei move much more slowly than the light electrons considering the high ratio between nuclear and electronic masses ( $M/m \cong 2000$ ). In the remaining electronic Hamiltonian, the nuclear positions are parameters instead of variables. The set of electronic energies thus computed becomes a function of the nuclear coordinates. For PO, the number of variables reduces to 96 – electronic coordinates. In the second step of the BO approximation this function serves as a potential in the Schrödinger equation containing only the nuclei – for PO an equation in 30 variables. The BO approximation is often considered as being synonymous with the adiabatic approximation.

Under the BO approximation, potential energy surface (PES) for movement of the relatively massive nuclei is used to describe the total electronic energy of a molecular system as a function of the coordinates of the nuclei. Theoretical PESs are constructed using quantum chemistry computation. It is still very difficult to obtain a complete PES except for the smallest systems because of formidable time consumption. There are two electronic structure methods making the BO approximation: the perturbation theory and the variation theory.<sup>9</sup>

### **2.2.2 Level of theory**

Highly correlated treatment of electrons is essential in the theoretical studies of intermolecular interactions where the dispersion interaction plays a significant role in the dissociation energy.<sup>10</sup> Widely used methods which accounts for electron correlation effects are the Møller-Plesset (MP) perturbation theory,<sup>11</sup> configuration interaction (CI),<sup>12, 13</sup> and the coupled-cluster (CC) methods.<sup>14-20</sup> MP-theory is a special



application of Rayleigh-Schrödinger perturbation theory, which considers a small (often external) perturbation to an unperturbed Hamiltonian for correlation potential. CI is a linear variational method where different electronic configurations (states) are mixed. Recent advances of density functional theory (DFT) allows one to include electron correlation at lower computational costs and obtain good agreements with experimental results.<sup>21, 22, 23, 24</sup> In addition, the accuracy of the methods employed for geometry optimizations needs to be carefully assessed when dealing with systems that involve intermolecular hydrogen bonds and dispersion interactions. *Ab initio* geometry optimizations for a number of chiral molecular complexes have been reported.<sup>25</sup> For smaller complexes, such as PO–hydrogen peroxide, the second order Møller-Plesset (MP2) perturbation theory was used for geometry optimizations.<sup>25</sup> For larger complexes such as uracil–HOOH, the optimization was performed with DFT method at the B3LYP level.<sup>26</sup> Given this background, MP2 theory has been chosen for the majority of computational work within this thesis of PO containing systems.

### 2.2.3 Basis set

The selection of a basis set depends on the nature of the interactions being studied and the available computational resources. To accurately describe the polarizability of chiral molecular monomers and the multipole moments and dispersion energy of the complex, diffuse and polarization functions should be included in the basis set. Though generally the results obtained using larger basis sets are more reliable, the use of larger basis sets quickly leads to a dramatic increase in the computational costs. Specifically, two types of basis sets, the Dunning's augmented

basis sets<sup>27</sup> and John Pople’s Gaussian functions,<sup>28</sup> have been chosen for trial and their quality are compared within the molecular systems being studied.

#### 2.2.4 Dissociation energy

The interaction energy of two molecules is defined by:<sup>29, 30</sup>

$$E_{\text{int}} = E_{AB} - E_A - E_B \quad (2.17)$$

where  $E_{AB}$  is the total energy of the dimer,  $E_A$  ( $E_B$ ) is the total energy of monomer A (B). This quantity can be directly calculated using perturbation theory.<sup>31</sup> In the supermolecule approach, the subunit energy  $E_A$  ( $E_B$ ) is calculated with the basis set of  $A$  ( $B$ ) while the complex energy  $E_{AB}$  is calculated using both subunits  $A$  and  $B$ ’s basis set:

$$\Delta E = E_{AB}(AB) - E_A(A) - E_B(B) \quad (2.18)$$

Therefore basis functions of each unit in the associated complex may augment the other unit, resulting in a lower  $E_{AB}$ . This effect is termed as basis set superposition error (BSSE).<sup>32</sup> One of the most popular methods to correct BSSE is the counterpoise (CP) correction method proposed by Boys and Bernardi,<sup>33</sup> which calculates each of the units with its own basis set and also the basis functions of the other (but without the nuclei or electrons, using so-called “ghost orbitals”):

$$CP = E_A(A) + E_B(B) - E_A(AB) - E_B(AB) \quad (2.19)$$

The CP correction method is utilized upon the completion of geometry optimizations in *ab initio* calculations throughout the whole thesis to correct the BSSE. The quantity  $\Delta E$  is referred as *raw* dissociation energy, denoted as  $D_e$  in later chapters to differentiate from the *dissociation energy*,  $D_0$ , which includes the zero-point energy

correction. The contribution of zero-point vibration to the interaction energy is obtained through harmonic frequency calculations. The frequency calculation results also contain information on the state of the optimized geometry: absence of negative (imaginary) frequency values indicates a local minimum on a potential energy surface; the presence of one imaginary frequency confirms a first-order saddle point; etc.<sup>34</sup>

## References

---

1. Bernath, P. F. *Spectra of Atoms and Molecules*, Oxford University Press: New York, **1995**.
2. Hollas, J. M. *High Resolution Spectroscopy*, 2nd edition, Wiley, **1998**.
3. Banwell, C. N.; McCash, E. M. *Fundamentals of Molecular Spectroscopy*, 4th edition, McGraw-Hill International, **1994**.
4. Gordy, W.; Cook, R. L. *Microwave Molecular Spectra*, 3rd edition, Wiley-Interscience, **1984**.
5. Herzberg, G. *Spectra of Diatomic Molecules*, New York: Van Nostrand, **1950**.
6. Watson, J. K. G. *J. Chem. Phys.* **1967**, *46*, 1935.
7. Watson, J. K. G. *Vibrational Spectra and Structure: A Series of Advances*, edited by Durig, J.R.; Elsevier, New York, **1977**, Vol. 6, pp. 1-89.
8. Jensen, P.; Bunker, P. R. *Computational Molecular Spectroscopy*, Wiley: West Sussex, **2000**.
9. Born, M.; Huang, K. *Dynamical Theory of Crystal Lattices*, Oxford University Press: New York, **1954**.
10. Kim, K. S.; Tarakeshwar, P.; Lee, J. Y. *Chem. Rev.* **2000**, *100*, 4145.
11. Møller, C.; Plesset, M. S. *Phys. Rev.* **1934**, *46*, 618.
12. Shavitt, I. in *Methods of Electronic Structure Theory*, Schaefer, H. F. III (ed); Plenum Press: New York, **1977**.
13. Siegahn, P. E. M. in *Methods in Computational Molecular Physics*, Diercksen, G. H. F.; Wilson, S.(eds); D. Reidel: Dordrecht, **1983**.
14. Pople, J. A.; Krishnan, R.; Schlegel, H. B.; Binkley, J. S. *Int. J. Quantum Chem.* **1978**, *14*, 545.
15. Cizek, J. *Adv. Chem. Phys.* **1969**, *14*, 35.
16. Bartlett, R. J.; Purvis, G. D. *Int. J. Quantum Chem.* **1978**, *14*, 516.
17. Purvis, G. D.; Bartlett, R. J. *J. Chem. Phys.* **1982**, *76*, 1910.

- 
18. Scuseria, G. E.; Janssen, C. L.; Schaefer, H. F., III *J. Chem. Phys.* **1988**, *89*, 7382.
  19. Scuseria, G. E.; Schaefer, H. F., III *J. Chem. Phys.* **1989**, *90*, 3700.
  20. Crawford, T. D.; Schaefer, H. F., III *Rev. Comput. Chem.* **2000**, *14*, 33.
  21. Hohenberg, P.; Kohn, W. *Phys. Rev.* **1964**, *136*, B864.
  22. Kohn, W.; Sham, L. J. *Phys. Rev.* **1965**, *140*, A1133.
  23. Parr, R. G.; Yang, W. *Density Functional Theory of Atoms and Molecules*, Oxford University Press: Oxford, **1989**.
  24. Labanowski, J. K., Andzelm, J. W. *Density Functional Methods in Chemistry*, Springer-Verlag: New York, **1991**.
  25. Portmann, S.; Inauen, A.; Lüthi, H. P.; Leutwyler, S. *J. Chem. Phys.* **2000**, *113*, 9577.
  26. Wysokiński, R.; Michalska, D.; Bieńko D. C.; Zeegers-Huyskens, T. *J. Phys. Chem. A* **2003**, *107*, 8730.
  27. Woon, D. E.; Dunning, T. H. Jr. *J. Chem. Phys.* **1993**, *98*, 1358.
  28. Krishnan, R.; Binkley, J. S.; Seeger, R.; Pople, J. A. *J. Chem. Phys.* **1980**, *72*, 650.
  29. Hirschfelder, J. O.; Curtiss, C. F.; Bird, R. B. *Molecular Theory of Gases and Liquids*, Wiley: New York, **1964**, p. 921.
  30. Szalewicz, K.; Jeziorski, B. *J. Chem. Phys.* **1998**, *109*, 1198.
  31. Szalewicz, K.; Jeziorski, B. *Molecular Interactions-From van der Waals to Strongly Bound Complexes*, edited by Scheiner, S.; Wiley: New York, **1997**, p. 3.
  32. Liu, B.; McLean, A. D. *J. Chem. Phys.* **1973**, *59*, 4557.
  33. Boys, S. F.; Bernardi, F. *Mol. Phys.* **1970**, *10*, 553.
  34. Cramer, C. J. *Essentials of Computational Chemistry: Theories and Models*, 2<sup>nd</sup> edition, Wiley, **2002**.

\*\*\*\*\*

## CHAPTER 3

### EXPERIMENTAL APPROACHES

\*\*\*\*\*

The rotational spectra of the PO containing complexes have been recorded using a pulsed molecular beam Fourier transform microwave (FTMW) spectrometer. Before presenting these studies in detail, I will provide a description of the spectrometer used for this research. As part of my thesis work, I contributed mainly to the construction of a rapid scan mid-infrared (IR) lead salt diode laser spectrometer. Since molecular expansion is used in both experimental instruments, this technique will be introduced first, followed by description of the two spectrometers.

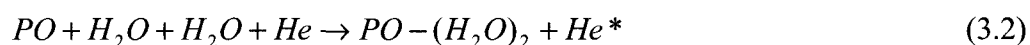
#### 3.1 Supersonic expansion

PO containing complexes are generated and stabilized in a pulsed molecular supersonic expansion. A supersonic expansion is produced by releasing gas phase molecules from a high pressure ( $> 1$  bar) gas reservoir into a low pressure ( $< 10^{-5}$  torr) region through a pulsed nozzle. During the course of such a rapid (in the order of millisecond) adiabatic expansion, the translational temperature of the carrier monatomic gas falls to very low value, less than 0.03 K in some cases.<sup>1</sup> Binary collisions between carrier gas atoms and seeded molecules lead to coupling between the translational temperature of the expansion and the translational, rotational and

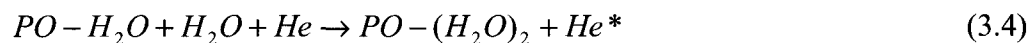
vibrational temperatures,  $T_{\text{rot}}$  and  $T_{\text{vib}}$  of the molecules. The cooling of  $T_{\text{rot}}$  is more efficient compared to  $T_{\text{vib}}$ , and only the lowest rotational energy levels of the molecular system are significantly populated. For example, a gas mixture of 0.1% benzene in 5 bar of helium pulsed to the vacuum chamber ( $\sim 5 \times 10^{-6}$  torr) through a nozzle of diameter 660  $\mu\text{m}$  was measured to have  $T_{\text{rot}} = 0.3 \text{ K}$ .<sup>2</sup> The rapidly decreasing temperature ( $\gg 3 \times 10^5 \text{ K/s}$ ) and density ( $\gg 3.8 \times 10^6 \text{ torr/s}$ ) in the supersonic jet bring the expanding gas into a free and stable flow in less than 1 ms. Both pinhole and slit nozzles can be used. Narrower linewidths are obtained from a slit nozzle because the velocity component of the expanding gas has a narrower distribution along the probing radiation. This is desirable for assignment of congested spectra. A molecular complex is formed at the initial phase of the expansion and can last in the near collisionless environment for measurements before the supersonic expansion breaks down. It is generally understood that binary complexes are formed via a three-body collision. For example:



where the third body, usually a rare gas atom like Ne, is necessary to carry away the excess kinetic energy.<sup>3, 4, 5, 6, 7, 8</sup> The mechanism of ternary complex formation is still under debate. One possibility is a four-body collision, for example:



or two successive three-body collision:



The short description above shows that a supersonic expansion provides a cold and nearly collisionless environment, which is particularly useful for the investigations of short-lived complexes. The characteristics of molecular expansion and its general applications in spectroscopy have been discussed in detail, for example in refs.1, 9 and 10.

### 3.2 Fourier transform microwave spectrometer

FTMW spectroscopy is based on the excitation of an ensemble of molecular systems with a coherent pulse of microwave radiation at an appropriate frequency and the subsequent detection of the coherent molecular emission signal as a function of time. The dipole moments of  $N$  individual molecules, upon interaction with a pulse of microwave radiation, are aligned in the electric field resulting in a macroscopic polarization,  $P(t)$ , of the ensemble of molecules. The molecules rotate in phase with each other as a result of the coherence property of the excitation microwave radiation pulse. The oscillating dipole moment,  $\mu$ , with the rotational transition frequency,  $\omega_0$ , of the molecules is recorded as a function of time:<sup>11</sup>

$$P(t) = N\mu \sin(\omega_0 t) \quad (3.5)$$

A mathematical operation, called Fourier transformation, converts the time-domain signal to the frequency-domain spectrum.<sup>12, 13</sup> The analysis of spectrum can be used to determine rotational constants, from which the geometry of the molecular complex can be derived with the support of *ab initio* calculations and/or isotopic substitution experiments. Therefore, FTMW spectroscopy is a powerful technique to provide accurate and detailed information about the structure and the dynamics of molecular



systems with fewer than twenty or thirty heavy atoms.<sup>14, 15, 16, 17, 18</sup> Furthermore, the high resolution capability of FTMW spectroscopy allows for the detection of fine and hyperfine spectral structures, such as small tunneling splitting, that might not be resolvable with other techniques. For example, in the study of the internal rotation tunneling motion of the cyclopropane ( $C_3H_6$ ) unit within the  $C_3H_6$ -Ne complex, small tunneling splittings with separations of a few hundred kHz ( $< 0.00003 \text{ cm}^{-1}$ ) were measured to the accuracy of 1 kHz using FTMW spectroscopy.<sup>19</sup>

A molecular beam FTMW spectrometer,<sup>19</sup> which combines the features of supersonic expansion and the high sensitivity of MW spectroscopy, was used for most experimental work in this thesis. The basic design of the spectrometer, depicted in Figure 3-1, follows that of the original Balle-Flygare spectrometer.<sup>3</sup> The central part of the spectrometer is a MW cavity that consists of two spherical aluminum mirrors. This also serves as sample cell. The mirror separation can be adjusted from 20 to 40 cm. The cavity assembly is housed in a vacuum chamber that is pumped by a diffusion pump backed up by a roughing pump. The pulsed nozzle is mounted near to the centre of one of the MW mirrors and the free-jet expansion of molecular complexes propagates parallel to the MW cavity axis.<sup>20</sup> The coherent MW pulse is generated using a MW synthesizer with a built-in 10 MHz reference crystal. The synthesizer generates radiation between 1 to 20 GHz. To generate the maximum polarization of the molecular sample for detection, the MW pulse length must be optimized. This requires consideration of the magnitude of the dipole moment of the molecular system under investigation (Equation 3-5). Typical MW pulse lengths for the study of PO containing complexes were 0.8-1.0  $\mu\text{s}$  for strong dipole moment transitions ( $\mu > 1.0$

Debye), 2.0-4.0  $\mu\text{s}$  for medium dipole moment transitions ( $\mu \sim 0.5$  Debye) and  $\sim 8.0$   $\mu\text{s}$  for weak transitions ( $\mu \sim 0.2$  Debye). The MW pulse is coupled into the MW cavity via a home-made wire antenna, which is also used to detect the molecular emission signal. A second antenna couples the MW radiation out of the chamber for tuning the MW cavity into resonance. The emission signal is amplified, digitized and Fourier transformed to a frequency spectrum via a home-written program in LabVIEW. As both the “forward” and “backward” (relative to the antenna) components of the emission signal are detected, each rotational transition line appears as a pair of Doppler doublets in the frequency spectrum. The distance between the Doppler splitting is proportional to the rotational transition frequency. For example, the separation of the doublets of a transition at 7.0 GHz is  $\sim 30$  kHz. The transition frequency is the average of the Doppler pair. As the velocity of a gas is inversely proportional to the square root of its mass, Ne gas travels slower ( $\sim 800$  m/s) than He ( $\sim 1800$  m/s). For a typical operating length of 30 cm of the MW cavity, a Ne expansion takes  $\sim 0.38$  ms while an expansion of He atoms traverses the same distance in  $\sim 0.17$  ms. Therefore linewidths of species using He as a carrier gas are typically wider compared to using Ne due to the shorter observation time of species in a He expansion. For example, in my measurement of PO–water complexes, linewidth of 7 kHz and 18 kHz was achieved using Ne and He as carrier gases, respectively.

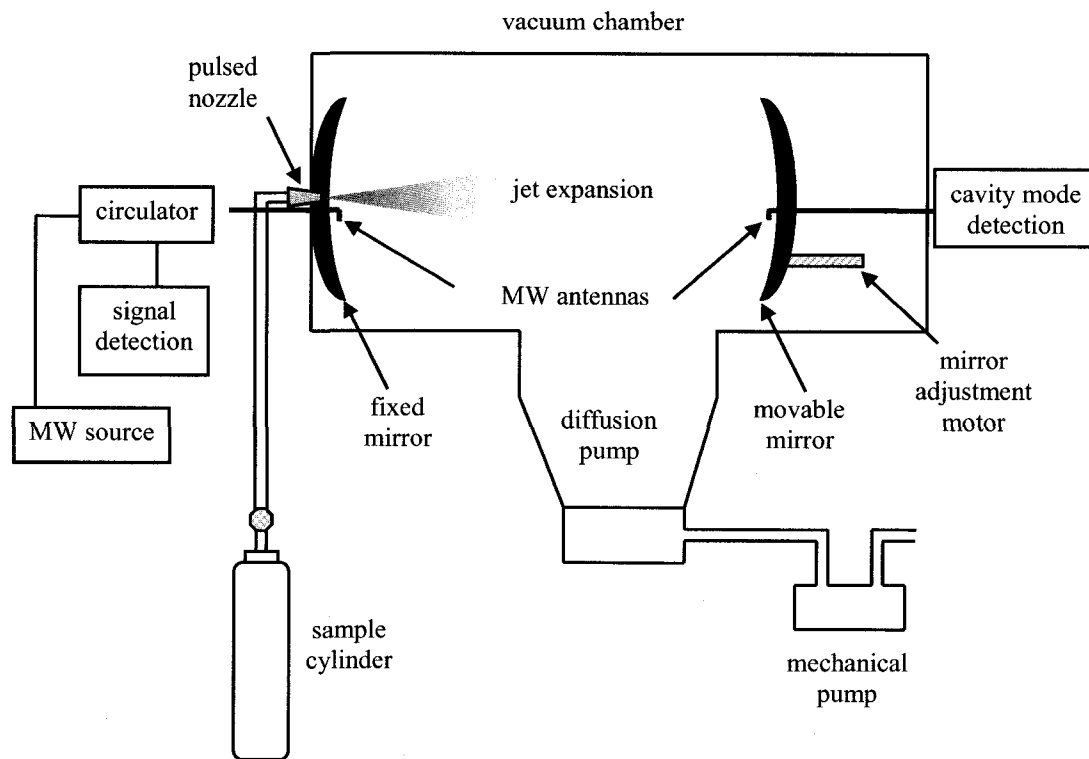


**Figure 3-1** A simplified diagram of the setup of the FTMW spectrometer.

### 3.3 Mid-infrared diode laser spectrometer

In order to be detected with FTMW spectrometer, a molecular system must have a permanent dipole moment. Therefore, studies of molecules possessing non-permanent dipole moment, for example,  $C_i$  symmetry species, demand other spectroscopic techniques. IR spectroscopy, which only requires change of dipole moments during the course of vibrational motions, therefore, has intrinsic advantages. In principal, rotationally-resolved vibrational spectroscopy can provide accurate information about rotational energy levels in both ground and vibrationally excited states. Therefore, the band origin of a vibrational motion,  $\nu_0$ , and the rotational

constants of the ground and vibrationally excited states can be derived from a rovibrational spectrum. In addition, information on the vibrational shifts that are signatures of the particular functional groups involving in the chiral recognition interactions can be extracted using IR spectroscopy.

In the past decades, high resolution IR spectroscopy of van der Waals complexes has emerged as one of the most direct and precise methods to the investigations of intermolecular forces. The first experiment using a tunable IR diode laser to study direct absorption spectra of complexes in a pulsed supersonic jet expansion was reported by Hayman *et al.* in 1985.<sup>21</sup> Since then, many other researchers have applied this technique to measure rovibrational spectra of weakly bound complexes in molecular beams.<sup>22, 23, 24, 25, 26, 27</sup> In all these cases, lead salt diode lasers are the radiation source. The molecular expansion, as already discussed in Section 3.1, greatly enhances sensitivity by redistributing the molecules into the lowest rovibrational energy levels. Further sensitivity enhancement is achieved by increasing the absorption path length significantly from the development of various multipass cells, e.g. Herriott,<sup>28, 29, 30</sup> White,<sup>31, 32</sup> Perry,<sup>33</sup> and astigmatic designs.<sup>34, 35</sup>

In this section, a molecular beam rapid scan mid-IR lead salt diode laser spectrometer coupled to an astigmatic multipass sample cell is described. The instrument has three main parts and each part will be described separately in the following description. First, lead salt diode lasers serving as the mid-IR light source are discussed. Second, two types of multi-pass cell for optical path length enhancements are introduced: Herriott-type for reference gas to enhance the precision of the frequency calibration and astigmatic type for molecular expansion. Third, the

arrangement of the components of the instrument including the alignment of the laser beam is shown in detail. Finally, detection schemes of signals are described: three measurement channels have been implemented to improve the efficiency of the experiment. The fast scanning technique has been utilized for spectral acquisition.<sup>36</sup>

### 3.3.1 Lead salt diode laser

Currently, there is a limited number of commercially available continuous wave (cw) tunable laser sources in the mid-IR region. Lead salt diode lasers are the most common and affordable ones for high resolution spectroscopic studies. They are available in the frequency region from about 100 to 3250  $\text{cm}^{-1}$ . Each diode may have a frequency span of tens of wavenumbers. Recently, cw distributed feedback quantum cascade (QC) lasers have been developed as viable alternatives to lead salt diodes.<sup>37</sup> However, the cost for each QC diode is substantially higher and the frequency coverage is usually only a few wavenumbers, whereas broad frequency coverage is essential to search for the IR spectra of chiral molecules and their complexes. Lead salt diode lasers are overall a good choice as mid-IR sources. Stable current sources with built-in modulation scheme and liquid-nitrogen dewar for temperature stabilization are commercially available, which make lead salt diode systems easy to implement. The narrow linewidths of the diodes ( $\sim 10^{-5} \text{ cm}^{-1}$ ) allows for high resolution spectroscopic studies.

### 3.3.2 Optical path length enhancement

For our spectrometer, the Herriott design is chosen for the static reference gas cell because it is the easiest among the choices to construct and fairly robust after alignment for multi passes. The heart of the spectrometer consists of a pair of astigmatic mirrors in the supersonic jet. The main advantage of this setup is that for a given number of passes through the cell, the beam spots are more widely spaced than in any other types of cells. Before the detailed discussion of the multipass cells, the fundamental concepts of absorption spectroscopy are briefly summarized.

#### 1) Beer-Lambert Law

The fundamental concept of IR spectroscopy is direct absorption of IR radiation by molecules or molecular complexes. In this technique, the Beer-Lambert Law is an empirical relationship that relates the absorption of radiation to the properties of the matter through which the light is traveling. It is generally expressed as:

$$A = \alpha lc \quad (3-6)$$

where,

$$A = \log_{10}(I_0 / I_1) \quad (3-7)$$

Here,  $A$  is absorbance;  $I_0$  is the intensity of the incident light;  $I_1$  is the intensity after passing through the matter;  $l$  is the distance that the light travels through the matter (the absorption path length);  $c$  is the concentration of the absorbing species; and  $\alpha$  is the absorption coefficient of the species.<sup>38</sup>

It is self-evident from the Beer-Lambert Law (Equation 3-6) that the sensitivity of a spectrometer depends on the absorption path length. Various schemes exist to increase the optical path length in direct absorption measurements. Since the development of the White cell,<sup>31</sup> spectroscopists have been using spherical mirrors to achieve long absorption path length, thus greatly enhancing the sensitivity in conditions of low optical density. The maximum possible optical path length in each cell is limited primarily by the radius of curvature and the mirror reflectivity. In principal, the light is introduced into the cell through one mirror at a certain angle and position, and is reflected between the two mirrors to trace out a proper pattern on the mirrors before it leaves the cell. The location and the spacing of the reflecting points along the pattern define various types of multi-pass cells. In the White cells,<sup>31,32</sup> which use three mirrors, the front and rear mirrors are separated by their radius of curvature,  $R$ , and can offer more than 100 passes. Two-spherical mirror multipass cells<sup>28, 29, 30</sup> with mirror spacing in the range of  $R/2 \leq L \leq 2R$  can also achieve a large number of passes (50-100). Uses of these cells are found popular in various areas, such as absorption spectroscopy,<sup>29,33</sup> Raman spectroscopy,<sup>39,40,41,42</sup> and laser resonators.<sup>28</sup>

## **2) Herriott-type multipass cell for reference gas**

The Herriott cell is constructed from two spherical gold-coated mirrors (2" diameter, reflectivity > 95%) and requires an off-axis coupling hole through which the laser beam enters and exits (Figure 3-2). The number of spots on each mirror and hence the number of optical absorption passes can be controlled by adjusting the separation of the two mirrors. The relative orientation of the two mirrors does not need

to be changed during the adjustment. This procedure allows robust operation of the reference gas cell upon changes of the incoming laser beam.

The patterns of spots on the mirror surfaces can be explained theoretically (see Ref. 28). In this instrument, the two mirrors are kept at a distance of about half of their common focal length which yields up to 40 spots on each mirror, corresponding to 80 passes of the laser beam. Since the focal length is approximately 50 cm, the maximum total optical absorption path length is 20 m. The whole cell including the rail and clamps is housed inside a home-made stainless steel box. The top of the box is covered by a plastic glass plate for convenient visualization while adjusting the laser beam pattern (Figure 3-3). A  $\text{CaF}_2$  Brewster angle window is mounted on one side of the box to allow the entrance and the exit of the beam. The cell is filled with 2 – 5 torr of appropriate reference gas. Line broadening was not noticeable within several weeks indicating a very small leak rate. This reference cell enables the observation of weak reference absorption lines, and thus the frequency calibration when there are only a few lines.



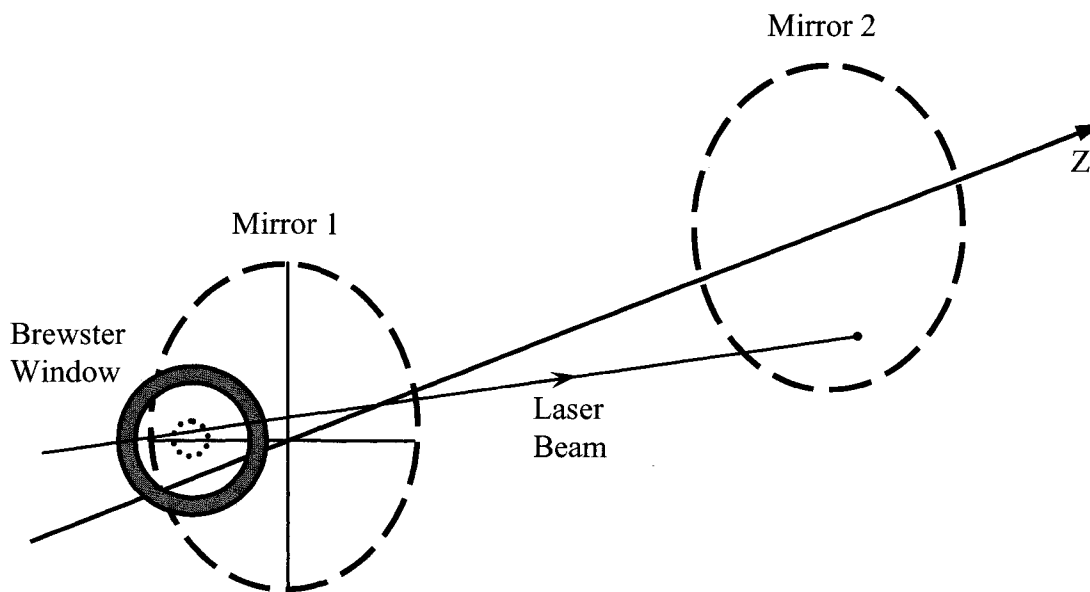
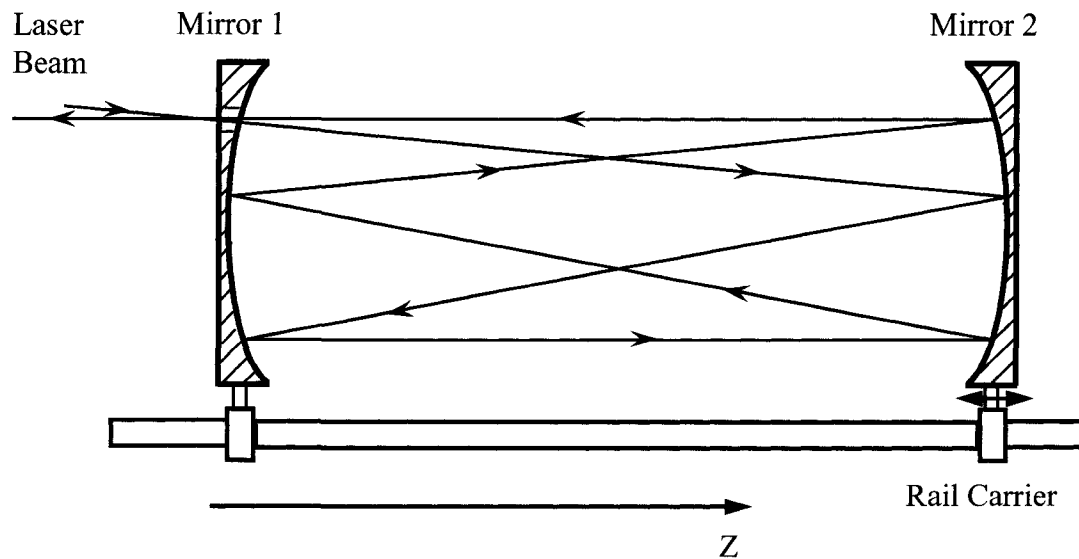


**Figure 3-2** Schematic diagram of the Herriott multipass cell (redrawn from Ref. 29), viewing from side direction. The laser spot pattern on the mirror surfaces can be altered by changing the separation between the two mirrors using the movable Mirror 2.

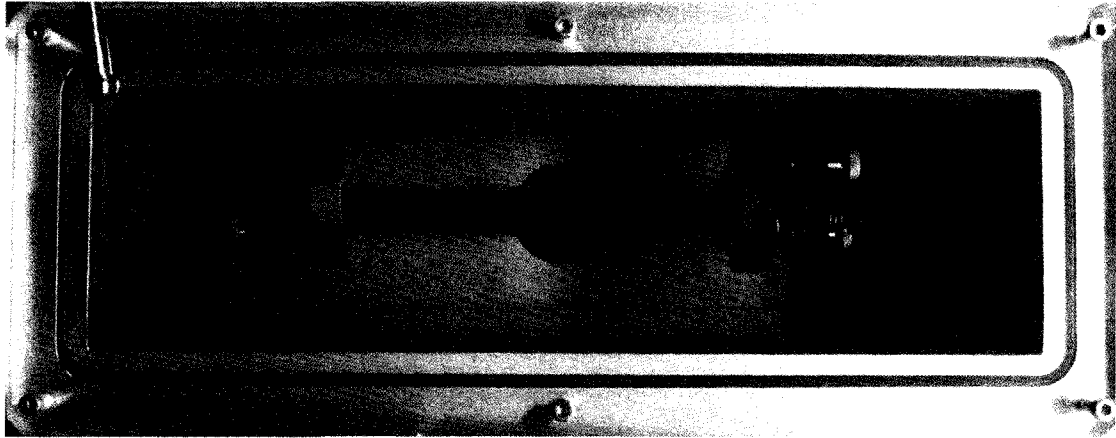


**Figure 3-3** Picture of the Herriott multipass cell for reference gas.

### **3) Astigmatic mirror multipass for molecular expansion**

The core component of this spectrometer is an astigmatic multi-pass cell consisting of a pair of astigmatic mirrors (Aerodyne Research), which have different radii of curvature along the two orthogonal axes.<sup>43, 44</sup> The main advantage of this variant is the large number of passes and therefore, significant enhancement of absorption path length. The two mirrors are mounted inside the vacuum chamber on a homemade optical bench, separated with a distance of about twice their common focal length (see Figure 3-4).



**Figure 3-4** Picture of the optical multipass between two astigmatic mirrors using a He-Ne laser (provided by Dr. O. Sukhorukov).

Although the cell works with a collimated beam, it is recommended to use a slightly focused beam, which should facilitate the observation of the beam spots on the mirrors and identify the spot pattern using a He-Ne laser. Therefore the input beam is mildly focused with a 50 cm focal length lens approximately to the centre of the cell, which is situated at the center of vacuum chamber. The input and the output beams enter and exit the cell at an approximate angle of  $\pm 3^\circ$  to the horizontal plane of the cell, respectively. The angle should be chosen so the first spot hits the edge of the back mirror. The alignment of the multipass cell is performed with the back mirror assembly, which can be tilted, translated and rotated. The important alignment parameters are the mirror separation and the twist angle between the mirrors. The tilt of the back mirror is only needed for fine tuning. Typically, the cell was first aligned to a 90-spot pattern.

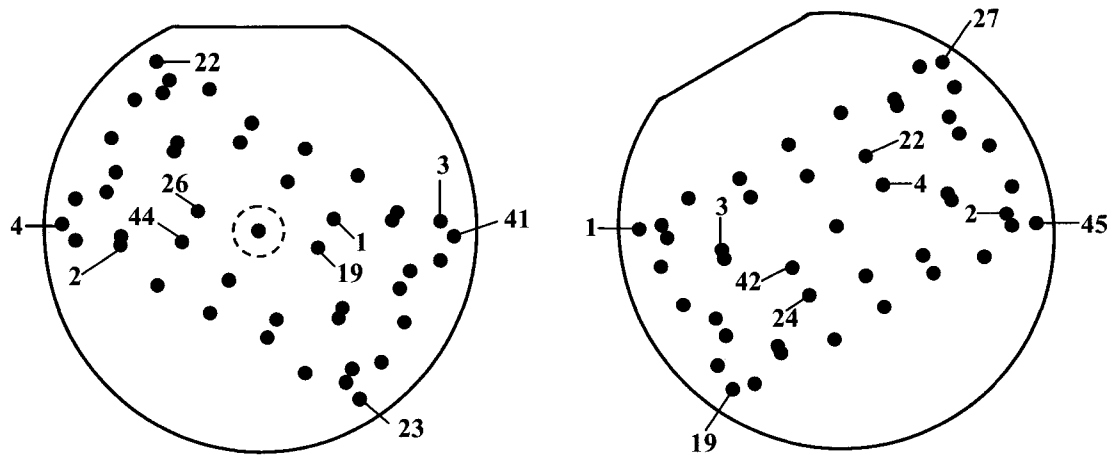


**Figure 3-5** Theoretical spot pattern of the 90-pass configuration with two astigmatic mirrors: front (left) and back (right) ones (redrawn from Figure 6 in Ref.45).

Counting the number of spots is normally very difficult even with focused visible beam. The correct alignment can be identified by matching the spot pattern to the theoretical one given in Figure 3-5 for 90-spot configuration. The actually observed spot patterns for the 90-spot configuration with spot ordering number are shown in Figure 3-6.

To achieve 182 multipasses, the back mirror was translated by 1-2 cm toward the other mirror from its 90-spot configuration. Though it is hard to trace 91 spots on each mirror sequentially, the 182-spot configuration can be recognized as a “mushroom” shape of the spot pattern on the mirror. The experimental observation of this configuration is illustrated in Figure 3-7. A pair of glass tubes was installed to protect the mirrors from being contaminated by diffusion pump oil during operation.

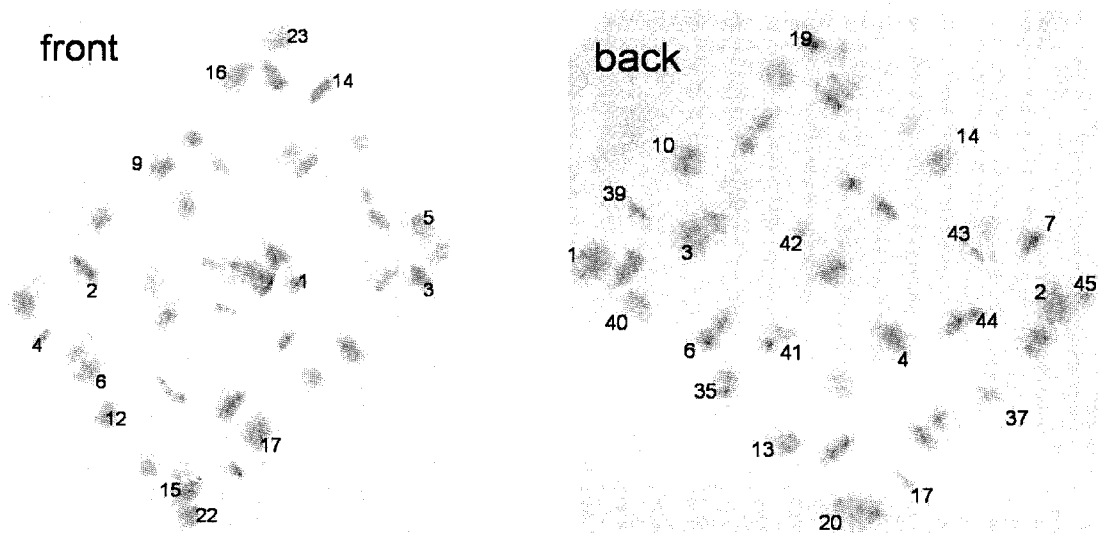


**Figure 3-6** Observed spot pattern of the 90-spot configuration with two astigmatic mirrors with empirical settings at 2.75 cm of the micrometer for the translational direction and about 20 degree of rotation (provided by Dr. N. Borho).

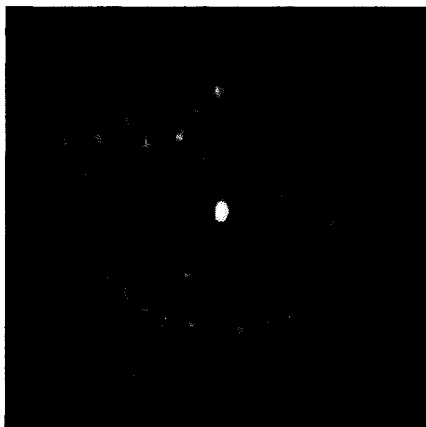


**Figure 3-7** Experimental observation of the 182-spot configuration. The spot pattern on each mirror traces out a “mushroom” shape.

### **3.3.3 Spectrometer design**

A schematic diagram of the instrument is shown in Figure 3-8. Up to four tunable lead salt diodes (Laser Components, Wilmington, MA), to cover wider frequency range, can be housed inside a liquid-nitrogen ( $N_2$ )-cooled dewar (Laser Photonics L5740). The laser temperature and hence its coarse and fine frequency tunings are achieved with a Laser Components L5830 control unit. The operating temperature can be further lowered to the minimum about 65 K (the triple point of  $N_2$ ) by reducing the pressure above the liquid nitrogen through a home-made vacuum pump system. A Stanford Research Systems (Sunnyvale, CA) function generator (DS345) is used to generate the laser current modulation signal.

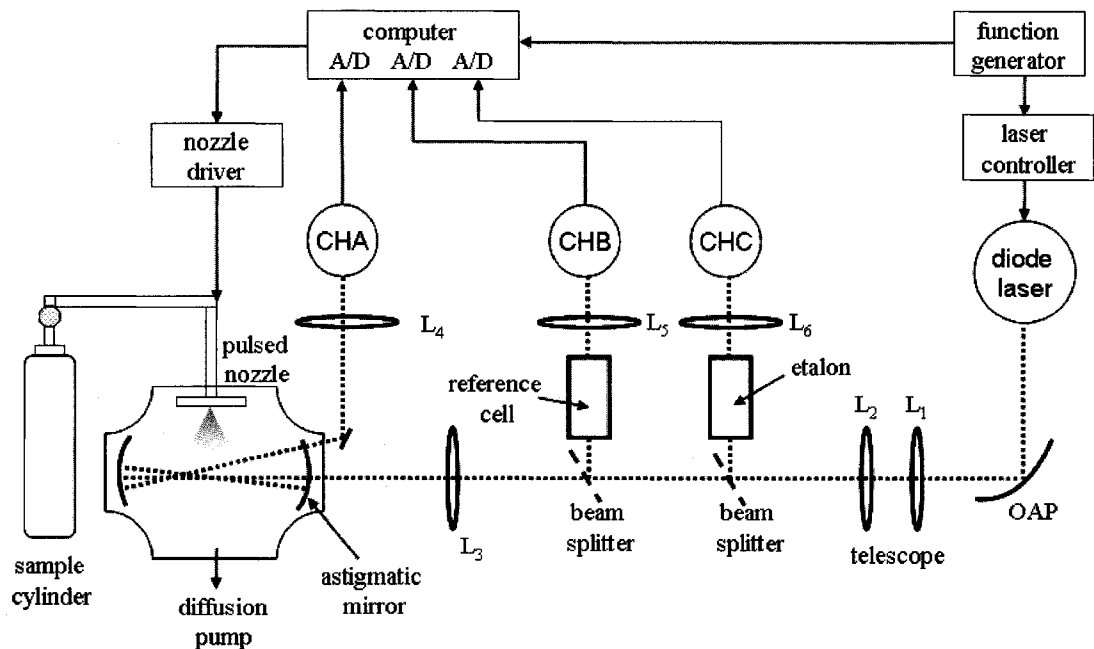


**Figure 3-8** Schematic diagram of the rapid scan mid-IR diode laser spectrometer.

The laser output is first collimated with an off-axis parabolic (OAP) mirror and the width of the laser beam was further reduced by using a telescope with a focusing ratio of 2.5:1 (CaF<sub>2</sub> lenses with focal length 250:100 mm). A mode selecting monochromator (L5110) can be implemented in the optical path for single-mode operation. Due to the intensity loss of the monochromator, this component is bypassed for single-mode lasing diodes. After the collimation and possible mode selection, the beam is then directed through two pellicle beam splitters which divert small portions (~ 8%) of the beam to separate reference gas and etalon wavelength calibration channels. Etalon is a spectroscopic device that has two flat parallel reflecting surfaces. It is used to measure distances in terms of wavelengths of spectral lines. Details of frequency calibration utilizing those two channels are given in the next section. The

solid 3" germanium etalon is temperature stabilized and has a free spectral range (fsr) of about  $0.0162 \text{ cm}^{-1}$ . The calibration beams are focused with a 100 mm focal length  $\text{CaF}_2$  lens onto a liquid- $\text{N}_2$ -cooled InSb detector (Infrared Associates, Stuart, FL), corresponding to CHB and CHC as shown in Figure 3-8 for reference gas and etalon calibrations, respectively. Also included in the optical path are two iris diaphragms with fixed positions which serve to define the path of the (invisible) IR beam. A He-Ne (visible) laser is introduced by a pair of two-dimensionally adjustable mirrors, one of which is removable, to guide the alignment of the IR beam with the aid of the two irises. The main portion of the beam is directed to a  $\text{CaF}_2$  Brewster angle window and mildly focused with a lens of 500 mm focal length to the centre of the vacuum chamber which houses the multipass sample cell. The sample and reference signals are collected by three InSb detectors, one each for the supersonic jet, reference gas, and etalon channels. The three channels of signals are then amplified, digitized with an A/D card (Gage Compuscope 1250) and stored in a personal computer (PC). The PC also controls the data acquisition and the operation of the spectrometer. All the optical components outside the vacuum system were placed inside a dry  $\text{N}_2$  purging box and the whole system can be purged if needed. .

The vacuum chamber is evacuated by a diffusion pump with liquid- $\text{N}_2$  baffle (Edwards Cryo-cooled Diffstak CR 160/700M, Wilmington, MA) backed by a dual-stage rotary pump (Edwards E2M30).<sup>46</sup> The gas mixture is injected into the sample cell using a pulsed nozzle (General Valve Series 9, Brookshire, TX) controlled by a nozzle driver (Parker Hannifin Corporation, Iota One). The distance from the jet

nozzle to the probing laser beam can be adjusted. During pulse expansion, the flow speed of a gas mixture can be monitored by a thermocouple vacuum gage.

### 3.3.4 Laser modulation and detection schemes

#### 1) Fast scan technique and data acquisition scheme

The optimum scan rate is a compromise between data acquisition speed and resolution. Although a spectrometer operating in a “slow scan” ( $\sim 0.001 \text{ cm}^{-1}\text{s}^{-1}$ ) does give excellent results,<sup>26, 27</sup> it generally requires a cw jet expansion where a very big vacuum pumping system is necessary and sample gas consumption is large. We chose to use the rapid scan technique introduced by De Piante *et al.*<sup>36</sup> The laser scan was found to be highly nonlinear when the internal ramp of the diode laser controller L5830 was used. Instead, an external function generator (DS345) is employed to generate a ramp of  $\sim 1.6 \text{ ms}$  duration at a rate of 580 Hz with a built-in 0.4 ms recovery time at the end of each ramp. This was written by Arbitrary Waveform Composer (AWC) and loaded to DS345,<sup>47</sup> which helped alleviate the problem of nonlinearity. The laser temperature and current are selected to give the desired frequency range. A typical scan covers  $\sim 1 \text{ cm}^{-1}$  and 100 – 1000 scans are averaged for each spectrum. Consecutive runs can be locked at the first run of the reference spectrum to reduce line broadening due to small laser drift over the data collection period.

A similar pulse sequence as reported by Brookes *et al.*<sup>48</sup> is used here, shown in Figure 3-9. A LabVIEW program is written to execute the pulse sequence and the data acquisition process.<sup>49</sup> The triggers from the function generator are masked with an



AND gate and are passed to the National Instrument (NI) DAQ and the gage A/D cards only when the gate drops to 0 V. The NI card counts the triggers and the software generates a waveform which is sent to the nozzle driver and to the two-channel multiplexer to alternate the collection of the reference and etalon data. Iota pulse is designed to trigger the nozzle. The spectra of the molecular complex are obtained by subtracting the background (without molecular pulses) from the signal (with molecular pulses). The delay time between the nozzle opening and the ramp for laser current can be optimized experimentally. The length of the jet opening (typically 2 ms) is adjustable by the setting on the front panel of the Iota One.

The sequence of Figure 3-9 is repeated at a rate of 1–4 Hz. The computer screen captured during data acquisition is shown in Figure 3-10. The top left window shows each single jet spectrum, and the one below it contains the accumulated spectrum from the most recent  $N$  scans. The top right and the bottom right windows display the average reference gas and etalon spectra, respectively.

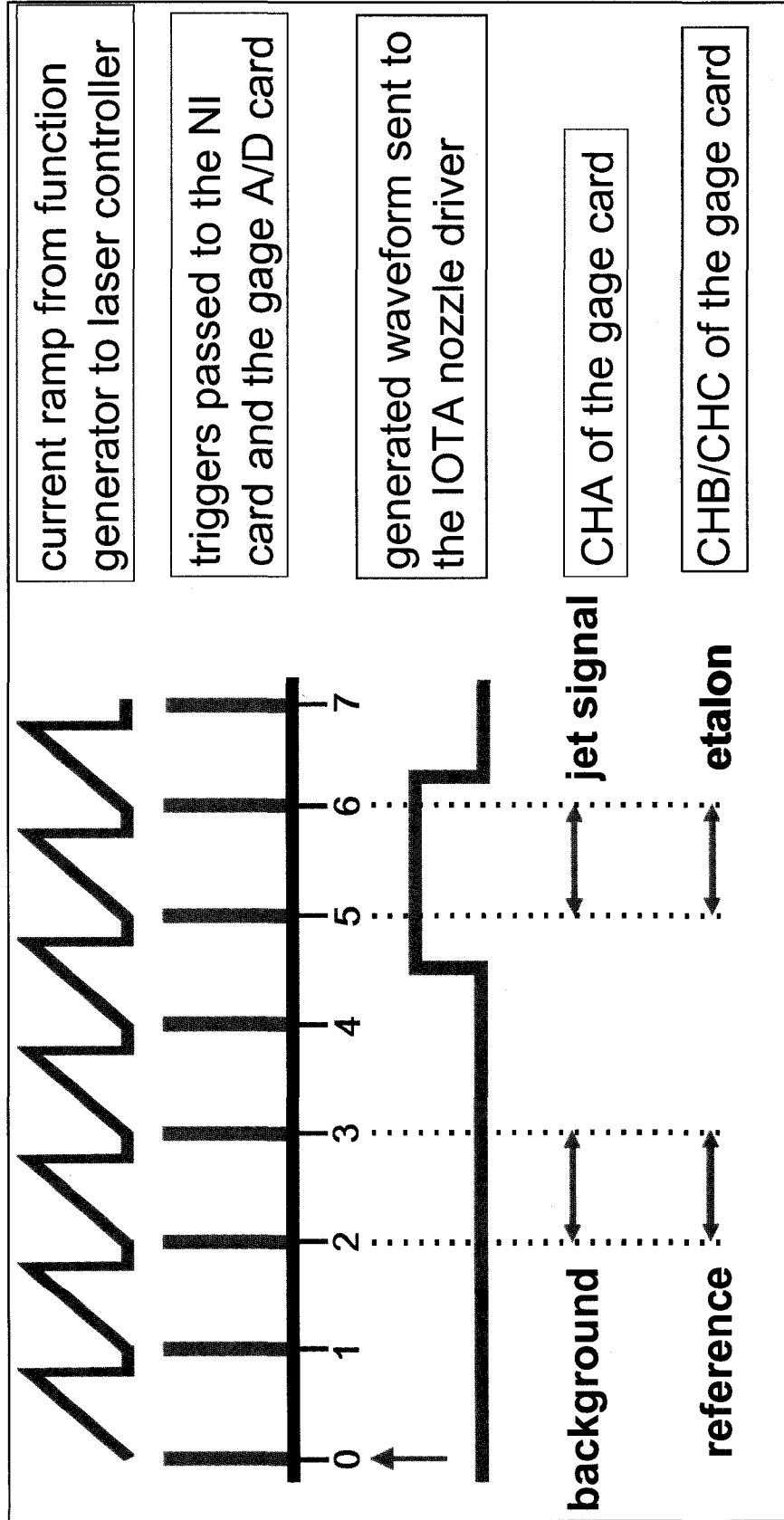


Figure 3-9 Pulse sequence of the rapid scan data acquisition procedure.

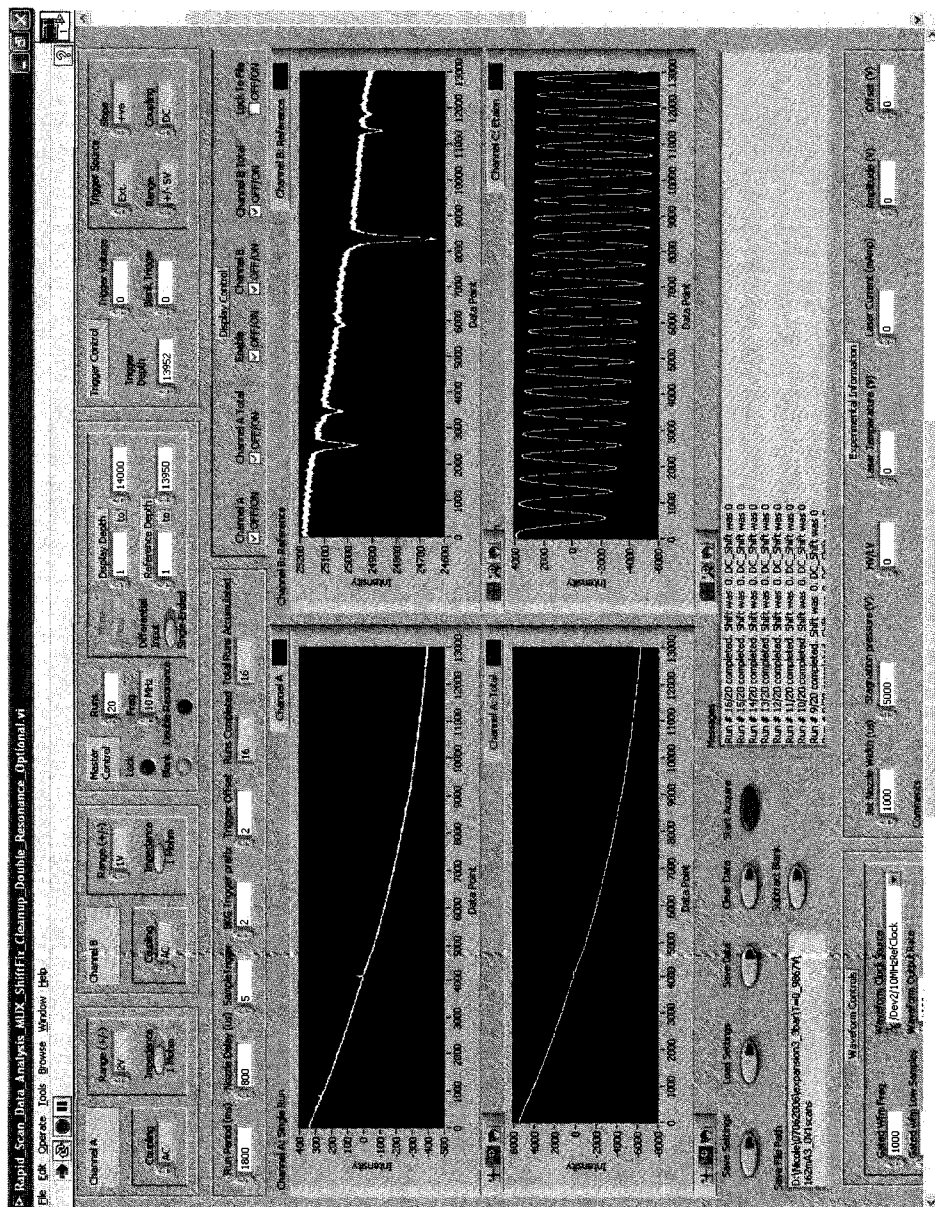


Figure 3-10 The computer screen display of the LabVIEW data acquisition operating program. <sup>49</sup>

## 2) Frequency calibration

Each data file contains 16300 data points for a particular channel (jet, reference gas or etalon). Post experiment data analysis is required to convert this information into a spectrum in the unit of wavenumber. The need for frequency calibration arises from the nonlinear scaling of the TDL frequency output with the applied current. Occasionally, the frequency output of the diode may result in a gap, commonly referred to mode hop, and/or multimode lasing, which both can be detected by the non-consistency of etalon fringes. The transitions in the simultaneously recorded reference spectrum serve as frequency markers for the calibration. First, peak locations in the reference gas file and each fringe in the etalon file need to be measured. Since this procedure is carried out manually, any additional desired peaks can be added, and undesired ones deleted. Normally, five to eight reference gas lines, which ideally are well distributed across the spectrum, are chosen for a polynomial fit. If there are too few reference peaks available or the peaks are too concentrated in one small section of a scan, it is necessary to use etalon peaks. Next, a program written in Fortran<sup>50</sup> calibrates the frequency scale of a laser spectrum using only the *reference* measurement or *reference + etalon*, where the data can be fitted polynomially or a linear interpolation between etalon fringes can be used, respectively. The wavenumber of each data point in the jet spectrum is then determined by a polynomial interpolation, at least to the 3<sup>rd</sup> or 4<sup>th</sup> order of fitting. Its standard deviation should be checked by the experimentalist in order to evaluate the quality of the resulting calibration. The acceptable accuracy is about 0.0006 or 0.0007 cm<sup>-1</sup>, which is consistent with the claimed laser linewidth of 20 MHz.

### 3) Measurement of rovibrational spectra

After installation of a new diode into the liquid-N<sub>2</sub>-cooled dewar, the laser current and temperature are adjusted to produce single mode output, which is verified using the etalon calibration. Single mode diode operation is advantageous as it eliminates the need for a monochromator, whose insertion usually reduces the laser power significantly. The apparatus described in this chapter has been used to study a few monomers and weakly-bound complexes using a few diodes.<sup>51</sup> The lowest observed full width at half maximum (FWHM) in the experiments was about 100 MHz (C<sub>3</sub>H<sub>6</sub>-CO<sub>2</sub> in 3 bar of Ne using Astigmatic mirror cell). For example, a portion spectrum of Ar-CO<sub>2</sub>, measured with Herriott multi-pass cell set up, as well as its assignment is shown in Figure 3-11.<sup>52</sup> The sample consisted of 0.5% CO<sub>2</sub> in 1.5 bar of Ar. A section of the spectrum of C<sub>3</sub>H<sub>6</sub>-CO<sub>2</sub> near the band origin of the complex is depicted in Figure 3-12, together with the quantum number assignments. The sample consisted of 0.5% CO<sub>2</sub> and 1.5~2% C<sub>3</sub>H<sub>6</sub> in 3 bar of Ne. As the spectrometer performance largely depends on the molecular system under investigation and its demonstration is beyond the scope of this thesis, I have chosen not to compare their resolution nor with literature data here.

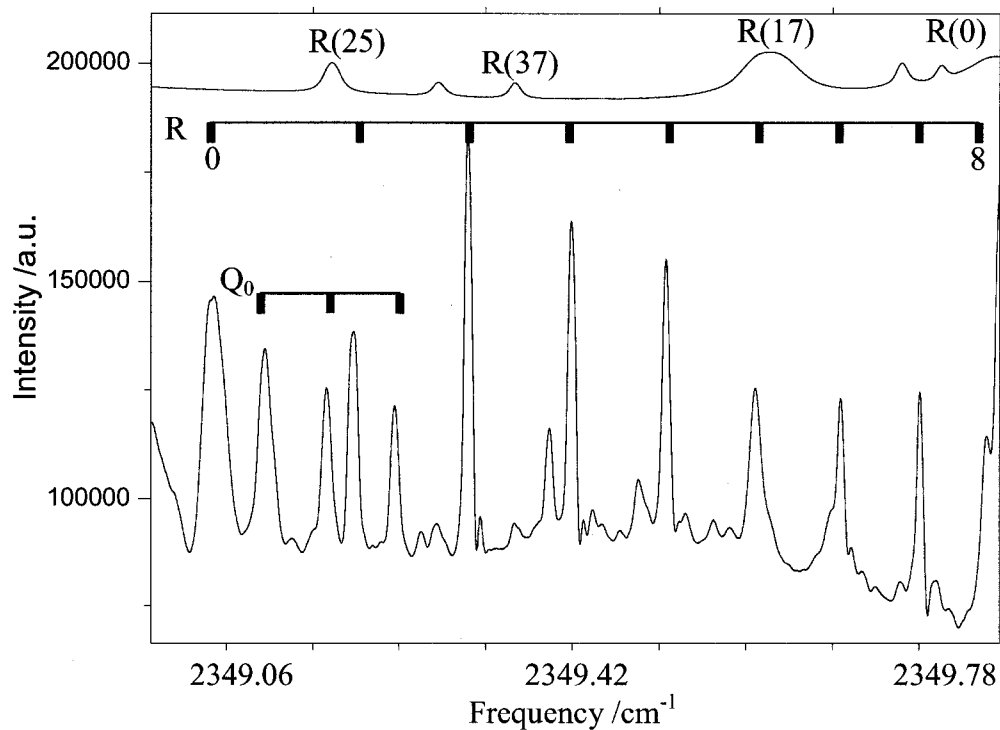


**Figure 3-11** Rotationally resolved IR spectrum of Ar-CO<sub>2</sub> near 2349 cm<sup>-1</sup> area. The quantum number assignments of the branches are indicated.<sup>52</sup> The sample consisted of 0.5% CO<sub>2</sub> in 1.5 bar of Ar. 100 scans were averaged. The *x*-axis shows the frequency in wavenumber and the vertical axis gives the relative intensity in arbitrary unit. The top curve is the CO<sub>2</sub> reference spectrum, which provides the frequency calibration.

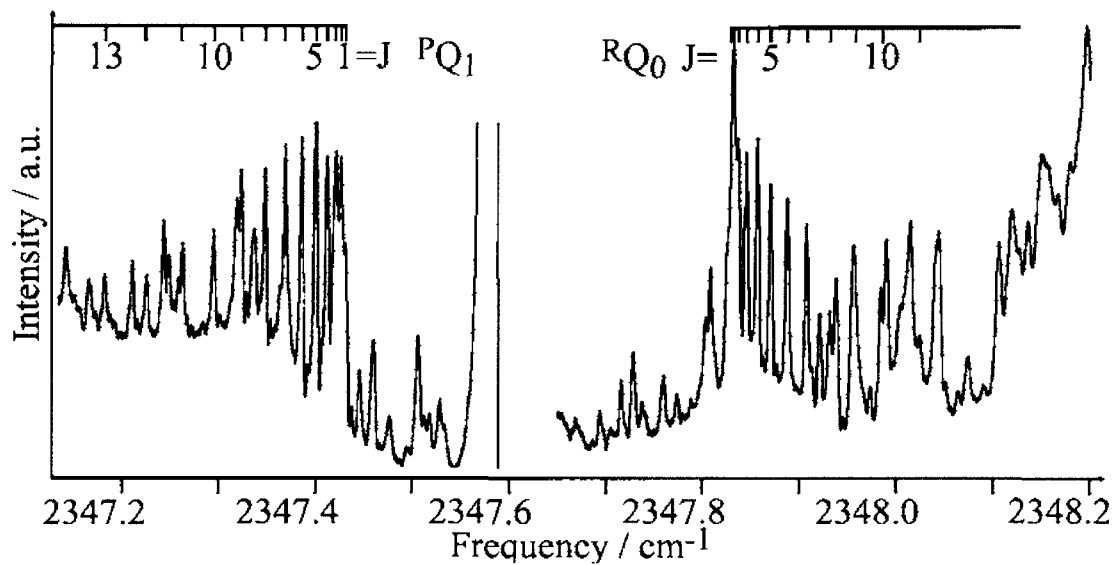


**Figure 3-12** A portion of the infrared spectrum of C<sub>3</sub>H<sub>6</sub>-CO<sub>2</sub> near the band origin of the complex. It is a composite spectrum of two rapid scan files. The quantum number assignments of the two *b*-type <sup>R</sup>Q<sub>0</sub> and the <sup>P</sup>Q<sub>1</sub> branches are indicated. The broad feature between 2347.55 and 2347.64 cm<sup>-1</sup> is the *P*(2) transition of the CO<sub>2</sub> monomer.

## References

---

1. Smalley, R. E.; Wharton, L.; Levy, D. H. *Acct. Chem. Res.* **1977**, *10*, 139.
2. Beck, S. M.; Livermann, M. G.; Monts, D. L.; Smalley, R. F. *J. Chem. Phys.* **1979**, *70*, 232.
3. Balle, T. J.; Flygare, W. H. *Rev. Sci. Instrum.* **1981**, *52*, 33.
4. Legon, A. C. *Ann. Rev. Phys. Chem.* **1983**, *34*, 275.
5. Hagen, O. F.; Gert, W. O. *J. Chem. Phys.* **1972**, *56*, 1793.
6. Golomb, D.; Good, R. E.; Brown, R. F. *J. Chem. Phys.* **1970**, *52*, 1545.
7. Golomb, D.; Good, R. E.; Bailey, A. B.; Busby, M. R.; Dawbarn, R. *J. Chem. Phys.* **1972**, *57*, 3844.
8. Calo, J. M. *J. Chem. Phys.* **1975**, *62*, 4904.
9. Levy, D. H. *Ann. Rev. Phys. Chem.* **1980**, *31*, 197.
10. Scoles, G. *Atomic and Molecular Beam Methods*, Oxford University Press: London, **1988**, Vol. 1, Chapter 2.
11. van Wijngaarden, J. *Dynamics of NH<sub>3</sub> Containing van der Waals Complexes*, PhD thesis, University of Alberta, **2002**.
12. McGurk, J. C.; Schmalz, T. G.; Flygare, W. H. *Adv. Chem. Phys.* **1974**, *25*, 1.
13. Ekkers, J.; Flygare, W. H. *Rev. Sci. Instrum.* **1976**, *47*, 448.
14. Campbell, E. J.; Buxton, L. W.; Balle, T. J.; Flygare, W. H. *J. Chem. Phys.* **1981**, *74*, 813.
15. Campbell, E. J.; Buxton, L. W.; Balle, T. J.; Keenan, M. R.; Flygare, W. H. *J. Chem. Phys.* **1981**, *74*, 829.
16. Dreizler, H. *Mol. Phys.* **1986**, *59*, 1.
17. Shoemaker, R. L. *Laser and Coherence Spectroscopy*, Plenum Press: New York, **1978**, p. 198.



- 
18. Dreizler, H.; Bunsenges, B. *Phys. Chem.* **1995**, *99*, 1451.
  19. Xu, Y.; Jäger, W. *J. Chem. Phys.* **1997**, *106*, 7968.
  20. Grabow, J.-U.; Stahl, W. *Z. Naturforsch.* **1990**, *45*, 1043.
  21. Hayman, G. D.; Hodge, J.; Howard, B. J.; Muentner, J. S.; Dyke, T. R. *Chem. Phys. Lett.* **1985**, *118*, 12.
  22. Lovejoy, C. M.; Schuder, M. D.; Nesbitt, D. J. *Chem. Phys. Lett.* **1986**, *127*, 374.
  23. Wang, Z.; Eliades, M.; Carron, J.; Bevan, J. W. *Rev. Sci. Instrum.* **1991**, *62*, 21.
  24. Hu, T. A.; Chappell, E. L.; Munley, J. T.; Sharpe, S. W. *Rev. Sci. Instrum.* **1993**, *64*, 3380.
  25. Pak, I.; Hepp, M.; Roth, D. A.; Winnewisser, G. *Rev. Sci. Instrum.* **1996**, *68*, 1668.
  26. Xu, Y.; McKellar, A. R. W. *J. Chem. Phys.* **1996**, *104*, 2488.
  27. Xu, Y.; McKellar, A. R. W. *Mol. Phys.* **1996**, *88*, 859.
  28. Herriott, D.; Kogelnik, H.; Kompfiner, R. *Appl. Opt.* **1964**, *3*, 523.
  29. Altmann, J.; Baumgart, R.; Weitkamp, C. *Appl. Opt.* **1981**, *20*, 995.
  30. McManus, J. B.; Keabian, P. L. *Appl. Opt.* **1990**, *29*, 898.
  31. White, J. U. *J. Opt. Soc. Am.* **1942**, *32*, 285.
  32. White, J. U. *J. Opt. Soc. Am.* **1976**, *66*, 411.
  33. Kaur, D.; de Souza, A. M.; Wanna, J.; Hammad, S. A.; Mercorelli, L.; Perry, D. S. *Appl. Opt.* **1990**, *29*, 119.
  34. McManus, J. B.; Keabian, P. L.; Zahniser, M. S. *Appl. Opt.* **1995**, *34*, 3336.
  35. Hao, L.-Y.; Qiang, S.; Wu, G.-R.; Qi, L.; Feng, D.; Zhu, Q.-S.; Hong, Z. *Rev. Sci. Instrum.* **2002**, *73*, 2079.
  36. De Piante, A.; Campbell, E. J.; Buelow, S. J. *Rev. Sci. Instrum.* **1989**, *60*, 858.
  37. Faist, J.; Capasso, F.; Sivco, D. L.; Sirtori, C.; Hutchinson, A. L.; Cho, A. Y.

---

*Science* **1994**, 264, 553.

38. Banwell, C. N.; McCash, E. M. *Fundamentals of Molecular Spectroscopy*, 4th edition, McGraw-Hill International, **1994**.
39. Owyong, A.; Patterson, C. W.; McDowell, R. S. *Chem. Phys. Lett.* **1978**, 19, 301.
40. Müller, G.; Weimer, E. *Optik* **1980**, 56, 1.
41. Trutna, W. R.; Byer, R. L. *Appl. Opt.* **1980**, 19, 301.
42. Hill, R. A.; Mulac, A. J.; Hackett, C. E. *Appl. Opt.* **1977**, 16, 2004.
43. Herriott, D. R.; Schulte, H. J. *Appl. Opt.* **1980**, 4, 883.
44. Keabian, P. L.; U. S. Patent 5,291,265 (1 March **1994**).
45. User's Manual of Models 5611 and 5612, Aerodyne Research Inc., Patent #5,291,265.
46. Osthoff, H. D. *Axial Molecular-Beam Tunable Diode Laser Spectrometer*, PhD thesis, University of Alberta, **2004**.
47. Osthoff, H. D.; Jäger, W.; Walls, J.; Wijngaarden, W. *Rev. Sci. Instrum.* **2004**, 75, 46.
48. Brookes, M. D.; Xia, C.; Tang, J.; Anstey, J. A.; Fulsom, B. G.; Yong, K. A.; King, J. M.; Mckellar, A. R. W. *Spectrochim. Acta Part A* **2004**, 60, 3235.
49. Mok, C.; Xu, Y. *Rapid Scan Data Analysis Manual and Report*, self-written program, University of Alberta, **2005**.
50. Bremm, D.; Xu, Y. *Diode Laser Frequency Calibration Program*, self-written program, University of Alberta, **2005**.
51. Borho, N.; Xu, Y.; private communication on for example, methyl lactate, formaldehyde dimer.
52. Sharpe, S. W.; Sheeks, R.; Wittig, C.; Beaudet, R. A. *Chem. Phys. Lett.* **1988**, 151, 267.

\*\*\*\*\*

## CHAPTER 4

### SPECTROSCOPIC INVESTIGATION OF PROPYLENE OXIDE

#### (PO) MONOMER AND PO-NE VAN DER WAALS DIMER

\*\*\*\*\*

#### 4.1 Introduction

Propylene oxide (PO), i.e.  $C_3H_6O$  as depicted in Figure 4-1, is one of the smallest, rigid, and chemically stable chiral molecules. It has one stereogenic centre, namely the carbon atom bonded with the methyl group. Because of its small size, it is a valuable prototype for theoretical and experimental studies of chiral recognition effect.<sup>1, 2</sup> A series of rotational spectroscopic studies of this molecule/molecular complex have been carried out, including the early investigations of the monomer,<sup>3, 4, 5</sup> and the later studies of the PO-rare gas (rare gas = Ne,<sup>6</sup> Ar,<sup>7</sup> Kr<sup>8</sup>) van der Waals complexes. These studies provided detailed and precise information about the ground state structures of the molecular system containing PO. On the other hand, *no* high resolution infrared (IR) spectroscopic studies of the PO monomer itself or the PO containing complexes have been reported so far. In fact, very few medium size organic molecules and even fewer chiral molecules have been studied using high resolution IR spectroscopy. Recently, spectra of some planar organic molecules, such as benzene<sup>9</sup> and formyl fluoride,<sup>10</sup> have been recorded in a supersonic jet using diode laser spectroscopy.

Martin Quack and co-workers reported the detailed high resolution investigation of CHBrClF using both a FTMW spectrometer and an FTIR spectrometer.<sup>11</sup> They have also investigated other small chiral molecules, such as fluorooxirane<sup>12</sup> and thiran-1-oxide,<sup>13, 14</sup> using high resolution IR spectroscopy. Rotational and centrifugal distortion constants of the ground and several first excited vibrationally states were determined from their IR spectra.

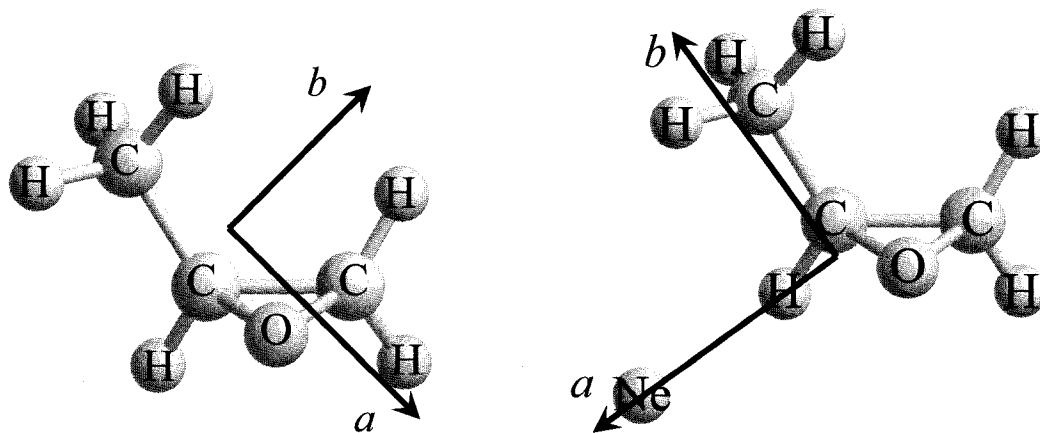


**Figure 4-1** Structure of the PO monomer (left) and the PO–Ne complex (right) in their respective principal axis systems.

In this chapter, the first observation of the rovibrational spectra of C–H stretching bands of PO with a rapid scan mid-IR diode laser spectrometer is discussed. Secondly, measurements of rotational transitions of the PO–<sup>20</sup>Ne and PO–<sup>22</sup>Ne complexes (shown in Figure 4-1) using the FTMW spectrometer are reported. Though this molecular system was studied using millimeter wave spectroscopy, we believe measurements in the microwave region contain new spectroscopic information and could be used to refine the existing spectroscopic constants.<sup>6</sup> The results also serve as

the base for the later work on the PO containing complexes seeded in the Ne carrier gas.

## **4.2 Investigation of the PO monomer**

### **4.2.1 Previous infrared studies of the C–H stretching modes of PO**

PO has 24 vibrational fundamental modes, among which, are six C–H stretching modes. There exists the possibility of strong couplings among the C–H vibrational modes and with the vibrational modes of the three-membered ring. The broadband low resolution spectrum of PO was recently measured using a filet-jet FTIR cluster spectrometer.<sup>15, 16</sup> This information has been used to guide the high resolution spectroscopic search and to aid the identification of the stretching motions responsible for the observed spectra. The frequencies, of the two strongest bands at 3051.2 and 3001.6  $\text{cm}^{-1}$  and of one weaker band at 2942.3  $\text{cm}^{-1}$ , agree very well with the previous static gas FTIR experiments.<sup>17</sup> The results are shown in Figure 4-2.

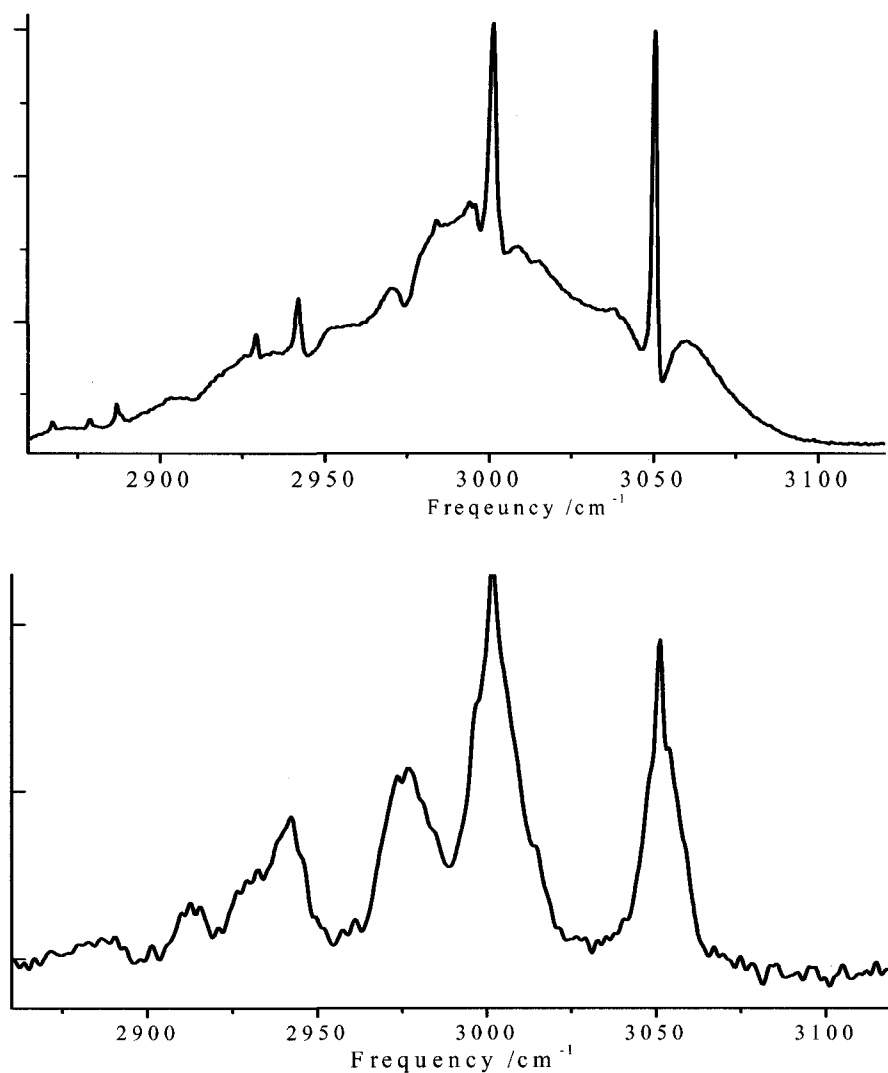


**Figure 4-2** Broadband low resolution FTIR spectrum of PO in the C–H stretching region. Top: 2 torr static gas spectrum at room temperature, 10 cm cell; bottom: slit jet expansion with 1% PO in He. The rotational temperature was estimated to be  $\sim 20$  K (copyright with Ref.18).

#### 4.2.2 *Ab initio* calculations

To assist the spectral search and assignment, calculations of harmonic frequencies and anharmonic vibrational-rotational couplings<sup>19, 20, 21</sup> were carried out using the GAUSSIAN03 software package.<sup>22</sup> Second-order Møller-Plesset perturbation theory (MP2)<sup>23</sup> with the basis set 6-311++G(d,p)<sup>24</sup> was chosen. The obtained frequency values of the band centres and their assignments are given in Table 4-1, together with the results from previous FTIR experiments.<sup>17</sup> The calculated rotational and centrifugal distortion constants of the ground and the first vibrationally excited states of the six C–H stretching modes of PO are listed in Table 4-2 compared with the FTMW spectroscopic results of the ground state.<sup>3</sup> In general, the calculations agree with the previous experimental work and can be used to guide high resolution rovibrational investigations. The rotational constants of the ground and the first vibrationally excited states are predicted to be similar, indicating that there is little structural difference between these two states.

#### 4.2.3 Experimental details

The rovibrational spectrum of the PO monomer was recorded using the rapid scan mid-IR lead salt diode laser spectrometer as described in Chapter 3. A lead salt diode laser around the 3.3  $\mu\text{m}$  region with single-mode operation in most frequency regions was used. The line positions are calibrated to be accurate to  $0.0006\text{ cm}^{-1}$  in most cases and to  $0.001\text{ cm}^{-1}$  as minimum accuracy. A pinhole nozzle (General Valve Series 9) fitted with two homemade slit plates which form a  $2\text{ cm} \times 60\ \mu\text{m}$  slit was used to generate the molecular expansion.

**Table 4-1** Harmonic frequencies (scaling factor of 0.94) of the six C–H stretching modes of PO obtained with MP2/6-311++G(d,p) calculations, together with the experimental values.

Stretching mode	Calculations				Broadband FTIR experimental				Tentative new assignment	
	Band type	Band centre /cm <sup>-1</sup>	Intensity	Band type <sup>a</sup>	Band centre /cm <sup>-1</sup> <sup>a</sup>	Band centre /cm <sup>-1</sup> <sup>b</sup>	Band centre /cm <sup>-1</sup> <sup>c</sup>	Band centre /cm <sup>-1</sup> <sup>d</sup>		Band type
$\nu_a(\text{CH}_2)$	<i>c</i>	3053	strong	<i>c/a</i>	3050.5	3051.2	3050.6	3050.1	-	-
$\nu(\text{CH})$	<i>c</i>	2990	strong	<i>C</i>	3001.0	3001.6	3001.3	3000.8	<i>c</i>	~3000
$\nu_s(\text{CH}_2)$	<i>b</i>	2957	strong	<i>b/a</i>	2995.8	2997.0	2994.0	2993.5	-	-
$\nu_{1a}(\text{CH}_3)$	<i>b/c</i>	2972	strong	<i>c</i>	2983.6	2977.0	2984.0	2988.3	<i>b</i>	2974
$\nu_{2a}(\text{CH}_3)$	<i>a/b</i>	2971	weak	<i>b</i>	2974	2973.7	2970.8	2970.9	<i>b</i>	2974
$\nu_s(\text{CH}_3)$	<i>a</i>	2889	medium	<i>a</i>	2941.7	2942.3	2942.0	2941.5	<i>a</i>	2942.5

<sup>a</sup> Ref. 17. The band shape data are estimations from the MW geometry of PO, not observation.

<sup>b</sup> Ref. 18: slit jet expansion spectrum.

<sup>c</sup> Ref. 25, 15 torr, 15 cm cell, 0.5 cm<sup>-1</sup> resolution.

<sup>d</sup> Ref. 26.



**Table 4-2** Rotational and centrifugal distortion constants of the ground and vibrationally first excited states of the six C–H stretching modes of PO obtained with MP2/6-311++G(d,p) calculations, together with the values of the ground state from FTMW experimental work.<sup>a</sup>

Parameter	Experimental	MP2/6-311++G** calculations						
		v = 0			v = 1			
		$\nu_a(\text{CH}_2)$	$\nu_s(\text{CH}_2)$	$\nu(\text{CH})$	$\nu_s(\text{CH}_2)$	$\nu_{1a}(\text{CH}_3)$	$\nu_{2a}(\text{CH}_3)$	$\nu_s(\text{CH}_3)$
<i>A</i> /MHz	18023.87	18027.61	17863.16	17807.64	17855.01	17883.85	17846.56	17839.48
<i>B</i> /MHz	6682.14	6680.12	6611.98	6615.13	6613.15	6616.54	6617.26	6618.37
<i>C</i> /MHz	5951.59	5948.56	5889.66	5888.82	5890.62	5890.62	5891.28	5891.46
<i>D</i> <sub>J</sub> /kHz	2.896	2.846						
<i>D</i> <sub>JK</sub> /kHz	3.300	3.329						
<i>D</i> <sub>K</sub> /kHz	19.820	20.382						
<i>d</i> <sub>1</sub> /kHz	0.186	0.199						
<i>d</i> <sub>2</sub> /kHz	2.926	3.491						

<sup>a</sup> Ref. 3.

For this work, we had implemented a much more powerful pumping system, consisting of a diffusion pump (Leybold, DIP8000) backed by a combination of a roots blower (Leybold, Ruvac WAU251) and a rotary pump (Leybold, Trivac D65B). It was therefore, possible to use two slit nozzles simultaneously to introduce the sample. One nozzle is located at the centre of the multipass alignment, while the second nozzle, which was originally implemented for the cavity ring down experiments,<sup>27</sup> was situated 12 cm away. The signal intensity improved significantly in comparison with that using only the central nozzle. The optimal gas concentration was 0.5% PO ( $\geq 99.0\%$ , Aldrich) in 2.5 bar of Ne (Praxair) using the slit nozzles mentioned above, or 0.25% PO in 1.3 bar of Ne using the pinhole nozzles. Ar and He were also used as carrier gas in separate experiments to make sure that the transitions observed are not due to the Ne containing complexes such as PO–Ne. For a well resolved absorption line, the full linewidth at half maximum is about 120 MHz.

#### **4.2.3 Rovibrational spectra**

The diode lasers in single mode in most of the targeted frequency areas: 2936.2 – 2945.6, 2970.4 – 2975.1, 2979.7 – 2989.8, and 3000.7 – 3009.2  $\text{cm}^{-1}$ . The search for the spectra of PO was performed in the available frequency range using the rapid scan mid-IR diode laser spectrometer. Several hundreds of spectral lines were observed, most of which were reproducible using all three carrier gases. This indicates that the formation of PO–rare gas complexes was not significant. Care was also taken to minimize the formation of PO dimer or larger PO clusters.

### 1) The tentative assignments of the $\nu_{1a}(\text{CH}_3)$ and $\nu_{2a}(\text{CH}_3)$ bands at $2974 \text{ cm}^{-1}$

Figure 4-3 shows the recorded spectra around  $2974 \text{ cm}^{-1}$ . Both pinhole and slit nozzles were used. Less congested spectra were obtained with the pinhole nozzle because of the lower rotational temperature achieved. Comparing to the ro-vibrational spectral simulations generated with the experimental ground state constants at two different rotational temperatures, one can find strong resemblances in the experimental spectral pattern. The observed spectra show two different series, both consistent with a spectral pattern with the *b*-type selection rule with a gap in the area around the band origin. The spacing between the heads of *P* (transition  $J'_{Ka'Kc'} - J''_{Ka''Kc''} = 1_{01} - 1_{10}$ ) and *R* branches (transition  $J'_{Ka'Kc'} - J''_{Ka''Kc''} = 1_{10} - 1_{01}$ ) is directly related to rotational constants of ground and vibrationally first excited states, i.e.  $[(A'-C')+(A''-C'')]$ , omitting the effects of centrifugal distortion constants. The observed value for the strong series is 2 GHz larger than  $2(A''-C'')$  when using the experimental values of the ground state rotational constants. For the weaker series, this value is 2GHz smaller than  $2(A''-C'')$ . This requires the rotational constants of the upper state, i.e. the first vibrational excited band, to be significantly different from those of the ground vibrational state. The observation is a strong indication that there is severe perturbation associated with the first vibrationally excited state. We speculated that these two vibrational states are perturbing each other. Further experimental work with MW-IR double resonance<sup>28</sup> and with other isotopomers will help to establish the firm assignments of the observed spectra.

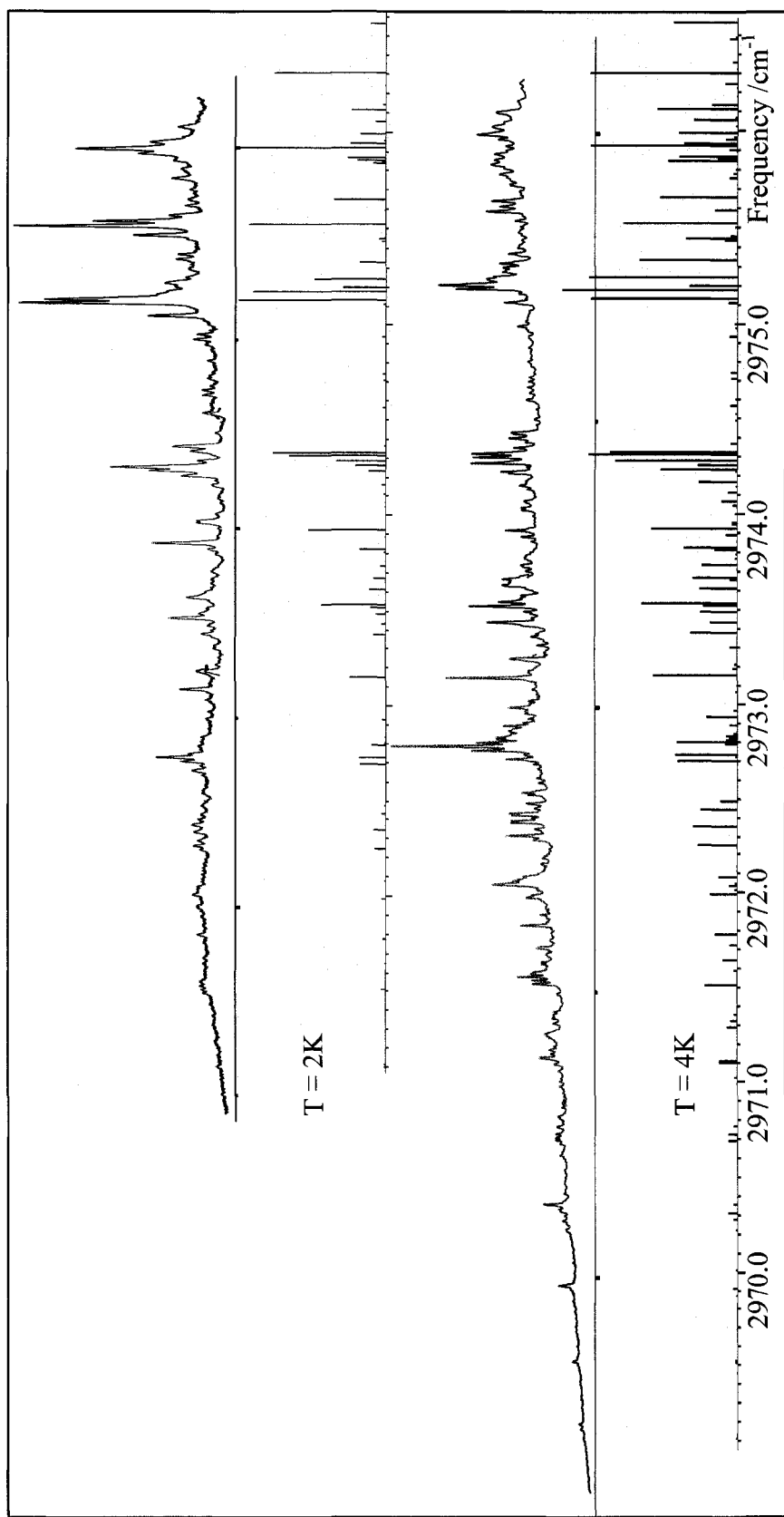
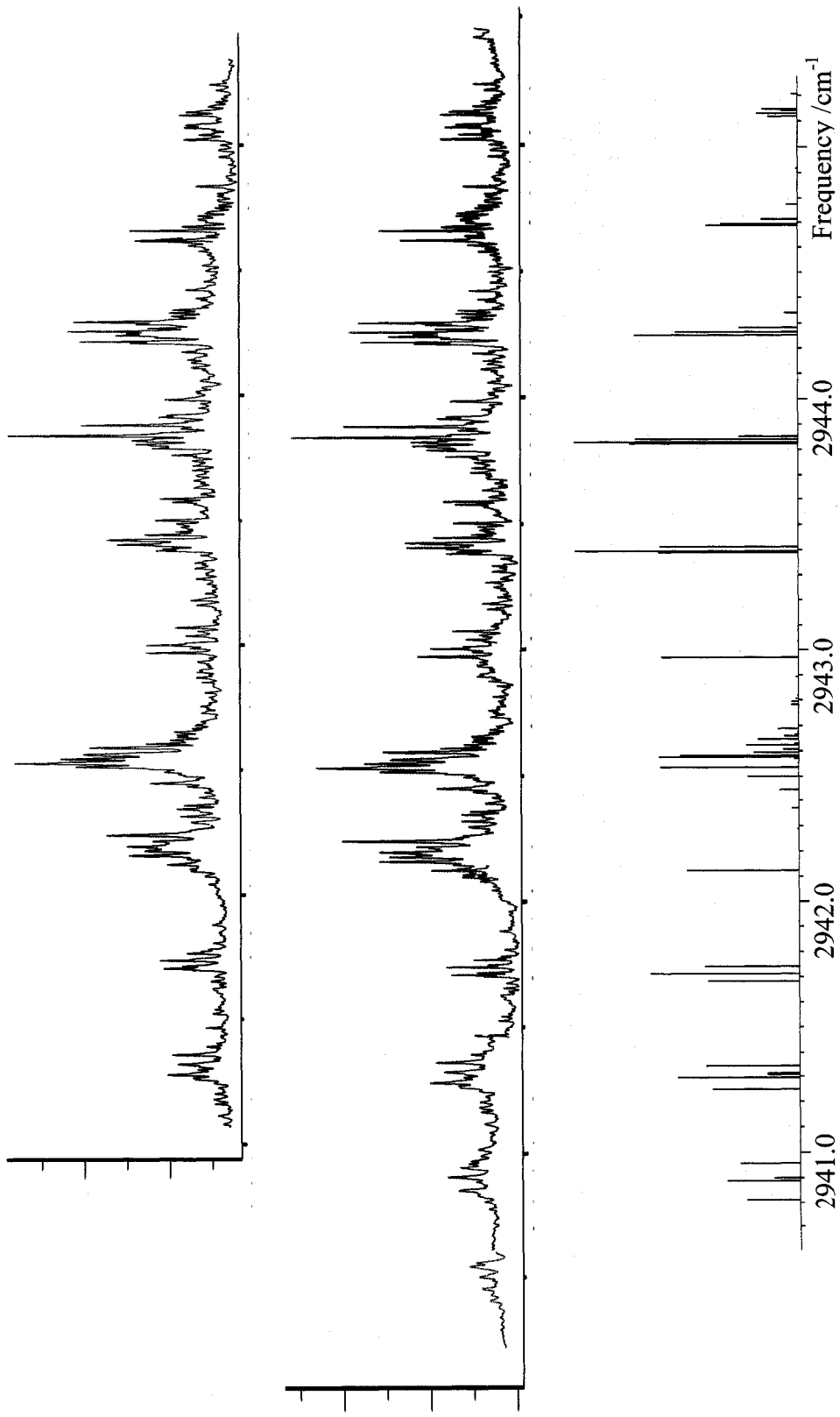


**Figure 4-3** Results for the  $\text{CH}_3$  asymmetric stretching. Top spectrum: 0.25% PO in 1.3 bar of Ne in a jet expansion using pinhole nozzle. Bottom spectrum: 0.5% PO in 2.5 bar of Ne using a slit nozzle. The stick spectra are simulated with the rotational constants from the microwave study<sup>3</sup> and the band centre from the previous FTIR study,<sup>17</sup> at a rotational temperature of 2K (top) and 4K (bottom), respectively. The rotational constants of the ground and excited states are assumed to be the same in the simulation.

## 2) The $\nu_3(\text{CH}_3)$ band at $2942\text{ cm}^{-1}$

Figure 4-4 shows the composite spectrum of three rapid-scan files. Slower ramping speed ( $0.8\text{ cm}^{-1}/\text{scan}$  as compared to  $1.6\text{ cm}^{-1}/\text{scan}$ ) was used to capture more details of the spectrum, which is a composite spectrum of seven rapid-scan files. By comparing to the simulated *a*-, *b*-, and *c*-type spectrum, it is clear that the spectral pattern is dominated with the *a*-type transition characters with little contribution from either *b*- or *c*-type transitions. The transitions were assigned using ground-state combination differences between the *P* and *R* branches. The resulting band centre is  $2942.55\text{ cm}^{-1}$ , in very good agreement with the FTIR measurements.<sup>18</sup> Because the observed spectra were fairly congested, some transitions could not be assigned with absolute confidence. Attempts were carried out to do a simultaneous fit with all rovibrational transitions assigned. But the standard deviations of the trial fits were much larger than the experimental uncertainty. This is again a strong indication that the excited vibrational state is perturbed.

**Figure 4-4** Rovibrational spectra of PO around the band origin of the  $\text{CH}_3$  symmetric stretching in the unit of  $\text{cm}^{-1}$ . Top: a composite spectrum of three rapid scan files, each at a ramping speed of  $1.6\text{ cm}^{-1}/\text{scan}$ . Middle: a composite spectrum of seven rapid scan files, each at a ramping speed of  $0.8\text{ cm}^{-1}/\text{scan}$ . Bottom: simulated spectrum at a rotational temperature of 3K.



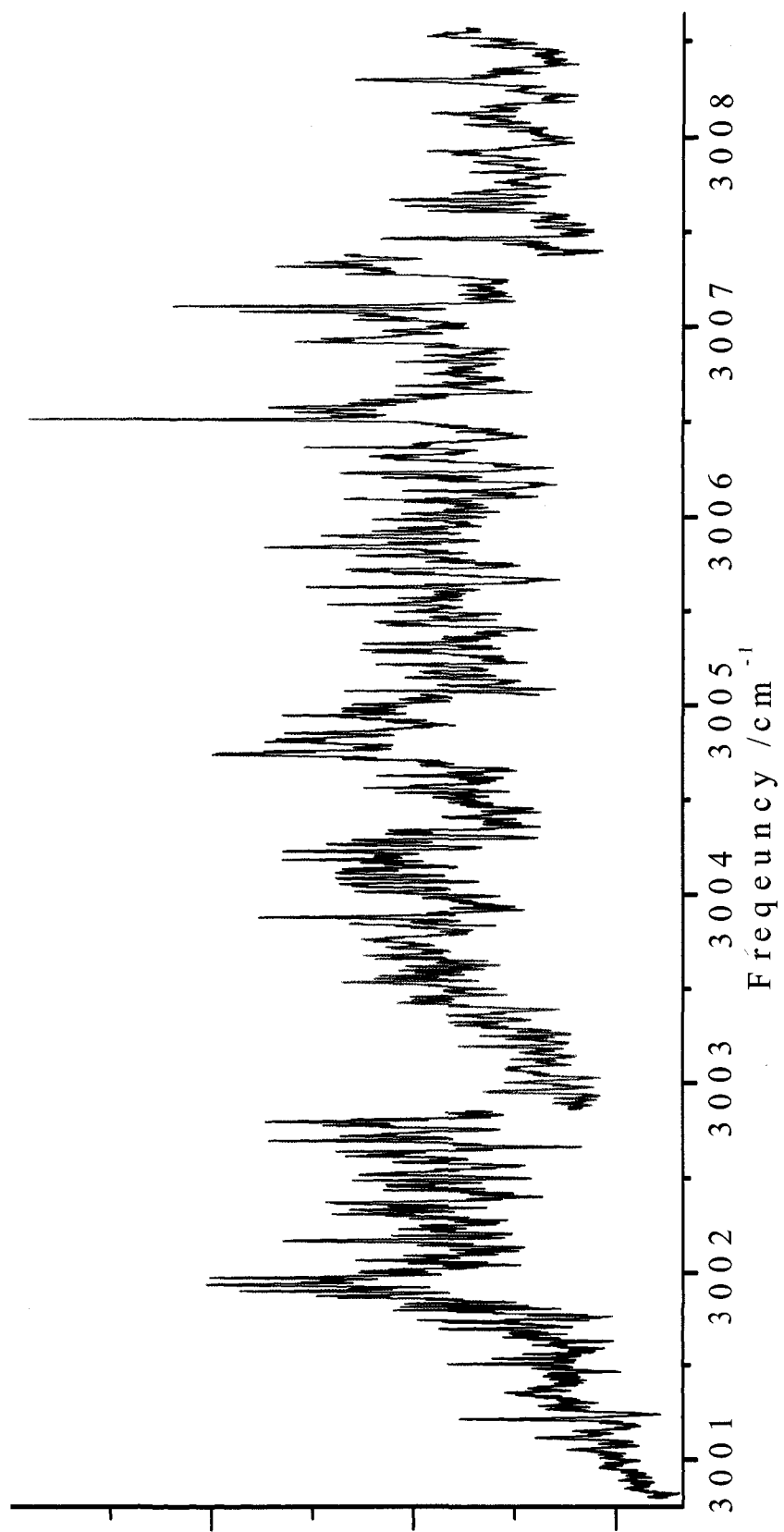


Figure 4-5 Rovibrational spectrum of PO in the area of 3000 cm<sup>-1</sup>.

### 3) Other bands

Extensive searches were also carried out in the region of 2979.7 – 2989.8 and 3000.7 – 3009.2  $\text{cm}^{-1}$ . In the former one, absorptions are much weaker compared to other regions, possibly due to the strength of the stretching mode itself. In the 3000  $\text{cm}^{-1}$  frequency region (Figure 4-5), the spectrum is highly congested. No attempt was made to make a detailed assignment.

## 4.3 Rotational study of PO–Ne molecular complex

### 4.3.1 Rotational spectra

The transitions of the PO–Ne complex were initially observed while performing the wide frequency scans for larger chiral molecular complexes involving PO. A large number of transitions were detected. This is often characteristic of the systems involving chiral molecules, where all three *a*-, *b*-, and *c*-type of transitions are allowed. Using the spectroscopic constants reported by Caminati and co-workers,<sup>6</sup> I was able to assign some of the observed transitions to the rotational transitions of PO–<sup>20</sup>Ne and PO–<sup>22</sup>Ne. These observed low *J* transition frequencies deviated by up to 1.2 MHz from the respective predictions with the millimeter wave study.<sup>6</sup> This suggests that the measured microwave transitions contain new spectroscopic information and could be used to refine the existing spectroscopic constants. The electric dipole moment of PO was determined using the Stark effect measurements to be 2.00(2) Debye,<sup>29</sup> mainly lying in the plane of the ring. Using the structural information of PO–Ne<sup>8</sup> and neglecting the small induced dipole moment generated by the PO–Ne interaction, the dipole moment for the complex along *a*-, *b*-, and *c*-axes were



calculated to be 1.89, 0.59, and 0.29 Debye, respectively. This agrees with *ab initio* calculations which indicate all dipole moment components were expected to be different from zero.<sup>6</sup> All three *a*-, *b*-, and *c*-types transitions were detected in our experiments. In total, 40 transitions, with *J* and *K<sub>a</sub>* up to 5 and 3, respectively, were measured for the <sup>20</sup>Ne containing isotopomer, and 38 transitions, with *J* and *K<sub>a</sub>* up to 4 and 3 respectively, for the <sup>22</sup>Ne containing isotopomer. All the observed transition frequencies are listed in Table A1.1 in Appendix 1.

#### 4.3.2 Discussion

The rotational fits were carried out with both the current microwave data and the millimetre wave transitions reported previously,<sup>6</sup> weighted with their respective experimental uncertainties of 1 kHz and 0.2 MHz. The transitions were fitted to a Watson's *S* reduction, *I'* presentation semi-rigid rotor Hamiltonian.<sup>30</sup> The resulting spectroscopic constants are collected in Table 4-3. The standard deviations of the fits are about 1.7 to 2.3 kHz for both isotopomers, comparable to the experimental uncertainty in the microwave measurements. The resulting spectroscopic constants are in accord with the previous published constants but with considerably smaller uncertainties.

The internal rotation of the methyl group in the PO monomer was studied in detail by Herschbach and Swalen<sup>29</sup> for the ground, first, and second vibrationally excited states. The tunnelling barrier for the vibrational ground state was estimated to be about  $894 \pm 25 \text{ cm}^{-1}$ . For the PO monomer, splittings on the order of tens of kHz were observed in our experiments for the ground state transitions with low *J* and *K<sub>a</sub>*

values. An example transition,  $J_{KaKc} = 3_{03}-3_{13}$ , for the PO monomer is given in Figure 4-6. Also shown in Figure 4-6 is the transition,  $J_{KaKc} = 2_{02}-2_{12}$ , of PO-<sup>22</sup>Ne, to demonstrate the typical signal-to-noise ratio and the resolution achieved in the measurements. In the microwave study of the dimethylether dimer complex,<sup>31</sup> splittings due to the methyl group internal rotation, on the order of tens of kHz, were observed for the “free” methyl group that is not directly involved in the van der Waals bonding. No splittings due to the internal rotation of the methyl group were observed for the PO-Ne complexes. This implies that such a splitting is effectively quenched in the PO-Ne complex. One possibility is that there is substantial interaction between the Ne atom and the methyl group in PO-Ne, which could increase the barrier height to internal rotation. However, a prediction using the XIAM internal rotation program<sup>32</sup> indicated that the tunnelling splitting would be on the order of only two or three kHz for the rotational transitions reported here for PO-Ne, even if the barrier height remains the same as in the monomer. As a consequence, no direct conclusion about the barrier height can be inferred from the current study.

In previous studies, two structures of PO-Ne complex were proposed depending on the position of the Ne with respect to the methyl group.<sup>6</sup> Our rotational measurements only resolved one set of rotational constants, which correspond to the global minimum conformer. Would it be possible to observe other structural minima for the PO-Ne van der Waals complex? In the case of the monodeuterated cyclopropane-Ne complex, two structural isomers with D-bonded and H-bonded Ne, were observed.<sup>33</sup> In that case, the zero point energy difference is about 2 cm<sup>-1</sup> between the two structural isomers, and the low temperature achieved in the molecular beam

expansion made it very difficult to detect and measure rotational transitions of the higher energy isomer. The next lowest energy structural minimum for the PO–Ne complex was predicted by the *ab initio* study to be about  $27\text{ cm}^{-1}$  higher in energy than the one observed here.<sup>8</sup> With this high energy, the observation of other structural isomers of the PO–Ne complex is unfeasible.

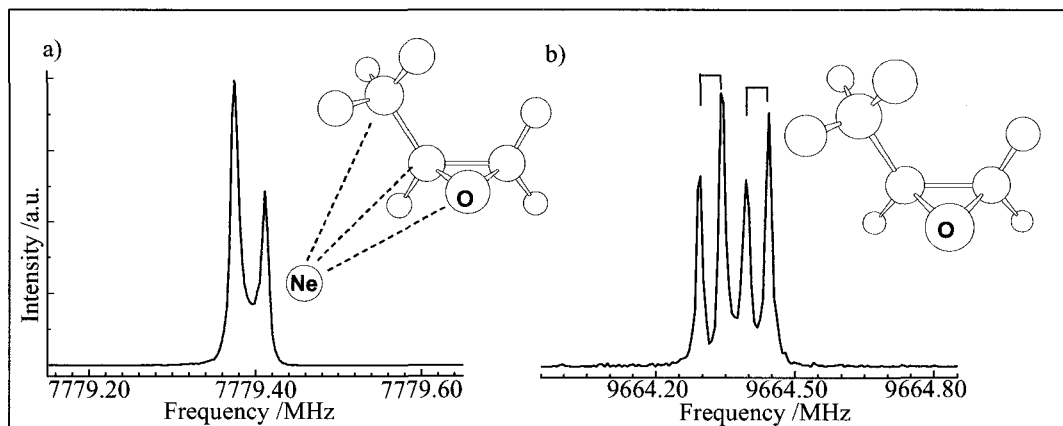


**Figure 4-6** a) An example rotational transition,  $J_{KaKc} = 2_{02}-1_{01}$ , of PO–<sup>22</sup>Ne. The insert on the right side illustrates the lowest energy configuration of PO–Ne as obtained from both the *ab initio* calculations and the experimental measurements (Ref. 6). The bonding of Ne to the three heavy atoms is indicated with dashed lines. b) An example rotational transition,  $J_{KaKc} = 3_{13}-3_{03}$ , of the PO monomer showing the narrow splittings due to the hindered internal rotation of the methyl group. The insert shows the structure of the free PO monomer. The transitions were recorded with 10 ns sampling interval, 8K data points, 16K Fourier transform, and 10 and 30 averaging cycles, respectively.

**Table 4-3** Rotational and centrifugal distortion constants of the propylene oxide–neon complex.

	PO– <sup>20</sup> Ne		PO– <sup>22</sup> Ne	
	This work	Literature <sup>b</sup>	This work	Literature <sup>b</sup>
<i>A</i> /MHz	6784.6564(7)	6784.780	6781.4211(7)	6781.561
<i>B</i> /MHz	2289.5456(2)	2289.698	2157.7888(4)	2157.96
<i>C</i> /MHz	1831.0033(2)	1831.141	1745.4865(4)	1745.53
<i>D<sub>J</sub></i> /kHz	27.64(1)	27.58	25.37(4)	25.58
<i>D<sub>JK</sub></i> /kHz	246.59(7)	255.30	223.8(1)	229.63
<i>D<sub>K</sub></i> /kHz	-199.1(2)	-204.87	-177.1(2)	-179.25
<i>d<sub>1</sub></i> /kHz	-6.415(3)	-6.525	-5.520(4)	-6.13
<i>d<sub>2</sub></i> /kHz	-1.811(2)	-1.830	-1.464(2)	-1.45
<i>H<sub>J</sub></i> /Hz	-2.6(4)	-5.47	-3(1)	-5.47
<i>H<sub>JK</sub></i> /Hz	-50(3)		-42(4)	
<i>H<sub>KJ</sub></i> /Hz	21.3(7)	39.2	26(17)	39.2
<i>H<sub>K</sub></i> /Hz	42.6(8)		16(22)	
$\sigma$ /kHz <sup>a</sup>	2.3	160	1.7	100

<sup>a</sup> Standard deviation of the fit.

<sup>b</sup> Ref. 6.

#### 4.4 Concluding remarks

In order to further investigate the intermolecular forces responsible for chiral recognition, the first step is to understand the spectrum of the monomer. The first high resolution IR spectra of four C–H stretching vibration modes of propylene oxide have been measured. Tentative assignment of the observed spectra was performed. This demonstrates the potential of using the rapid scan mid-IR lead salt diode laser spectrometer to study vibrationally excited states of chiral molecules and vibrational shifts that are signatures of the particular functional groups involving in the chiral recognition interactions. Pure rotational transitions of PO–<sup>20</sup>Ne and PO–<sup>22</sup>Ne in the frequency region between 4 to 18 GHz were measured. Refined rotational and

centrifugal distortion constants have been obtained for the PO-<sup>20</sup>Ne and PO-<sup>22</sup>Ne isotopomers. These measurements serve as the basis for the later work on larger chiral molecular complexes containing PO and using Ne as carrier gas.

## References

---

1. Portmann, S.; Inauen, A.; Lüthi, H. P.; Leutwyler, S. *J. Chem. Phys.* **2000**, *113*, 9577.
2. Borho, N.; Xu, Y. *Angew. Chem. Int. Ed.* **2006**, *46*, 2276.
3. Swalen, J. D.; Herschbach, D. R. *J. Chem. Phys.* **1957**, *27*, 100.
4. Herschbach, D. R.; Swalen, J. D. *J. Chem. Phys.* **1958**, *29*, 761.
5. Imachi, M.; Kuczkowski, R. L. *J. Mol. Struct.* **1982**, *96*, 55.
6. Blanco, S.; Maris, A.; Melandri, S.; Caminati, W. *Mol. Phys.* **2002**, *100*, 3245.
7. Blanco, S.; Maris, A.; Millemaggi, A.; Caminati, W. *J. Mol. Str.* **2001**, *612*, 309.
8. Blanco, S.; Melandri, S.; Maris, A.; Caminati, W.; Velino, B.; Kisiel, Z. *Phys. Chem. Chem. Phys.* **2003**, *5*, 1359.
9. Uskola, A.; Basterretxea, F. J.; Castano, F. *J. Mol. Spectrosc.* **1999**, *198*, 429.
10. Xu, Y.; Johns, J. W. C.; McKellar, A. R. W. *J. Mol. Spectrosc.* **1994**, *167*, 147.
11. Bauder, A.; Beil, A.; Luckhaus, D.; Müller, F.; Quack, M. *J. Chem. Phys.* **1997**, *106*, 7558.
12. Hollenstein, H.; Luckhaus, D.; Pochert, J.; Quack, M.; Seyfang, G. *Angew. Chem. Int. Ed.* **1997**, *36*, 140.
13. Gross, H.; He, Y.; Jeitziner, C.; Quack, M.; Seyfang, G. *Ber. Bunsen-Ges. Phys. Chem.* **1995**, *99*, 358.
14. Gross, H.; Grassi, G.; Quack, M. *Chem. Eur. J.* **1998**, *4*, 441.
15. Rice, C.; Borho, N.; Suhm, M. A. *Z. Phys. Chem.* **2005**, *219*, 379.
16. Borho, N.; Suhm, M. A.; Le Barbu-Debus, K.; Zehnacker, A. *Phys. Chem. Phys. Chem.* **2006**, *8*, 4449.
17. Winther, F.; Hummel, D. O. *Spectrochimica Acta* **1969**, *25A*, 417.
18. Borho, N.; Suhm, M.; private communication.

- 
19. Green, W. H.; Jayatilaka, D.; Willetts, A.; Amos, R. D.; Handy, N. C. *J. Chem. Phys.* **1990**, *93*, 4965.
20. Minichino, C.; Barone, V. *J. Chem. Phys.* **1994**, *100*, 3717.
21. Barone, V. *J. Chem. Phys.* **1994**, *101*, 10666.
22. Frisch, M. J.; Trucks, G. W.; Schlegel, H. B.; Scuseria, G. E.; Robb, M. A.; Cheeseman, J. R.; Montgomery, J. A. Jr.; Vreven, T.; Kudin, K. N.; Burant, J. C.; Millam, J. M.; Iyengar, S. S.; Tomasi, J.; Barone, V.; Mennucci, B.; Cossi, M.; Scalmani, G.; Rega, N.; Petersson, G. A.; Nakatsuji, H.; Hada, M.; Ehara, M.; Toyota, K.; Fukuda, R.; Hasegawa, J.; Ishida, M.; Nakajima, T.; Honda, Y.; Kitao, O.; Nakai, H.; Klene, M.; Li, X.; Knox, J. E.; Hratchian, H. P.; Cross, J. B.; Adamo, C.; Jaramillo, J.; Gomperts, R.; Stratmann, R. E.; Yazyev, O.; Austin, A. J.; Cammi, R.; Pomelli, C.; Ochterski, J. W.; Ayala, P. Y.; Morokuma, K.; Voth, G. A.; Salvador, P.; Dannenberg, J. J.; Zakrzewski, V. G.; Dapprich, S.; Daniels, A. D.; Strain, M. C.; Farkas, O.; Malick, D. K.; Rabuck, A. D.; Raghavachari, K.; Foresman, J. B.; Ortiz, J. V.; Cui, Q.; Baboul, A. G.; Clifford, S.; Cioslowski, J.; Stefanov, B. B.; Liu, G.; Liashenko, A.; Piskorz, P.; Komaromi, I.; Martin, R. L.; Fox, D. J.; Keith, T.; Al-Laham, M. A.; Peng, C. Y.; Nanayakkara, A.; Challacombe, M.; Gill, P. M. W.; Johnson, B.; Chen, W.; Wong, M. W.; Gonzalez, C.; Pople, J. A. *GAUSSIAN03*, Revision B.01, Gaussian, Inc., Pittsburgh PA, **2003**.
23. Binkley, J. S.; Pople, J. A. *Int. J. Quantum Chem.* **1975**, *9*, 229.
24. Krishnan, R.; Binkley, J. S.; Seeger, R.; Pople, J. A. *J. Chem. Phys.* **1980**, *72*, 650.
25. Losada, M.; Xu, Y.; private communication.
26. By the Analytical and Instrumentation Laboratory, Department of Chemistry, University of Alberta, **2007**.
27. Tam, W.; Leonov, I.; Xu, Y. *Rev. Sci. Instrum.*, **2006**, *77*, 063117.
28. Osthoff, H. D. *Axial Molecular-Beam Tunable Diode Laser Spectrometer*, PhD thesis, University of Alberta, **2004**.
29. Swalen, J. D.; Herschach, D. R. *J. Chem. Phys.* **1957**, *27*, 100; Herschbach, D. R.; Swalen, J. D. *J. Chem. Phys.* **1958**, *29*, 761.
30. Watson, J. K. G. *Vibrational Spectra and Structure: A Series of Advances*, edited by Durig, J. R.; Elsevier: New York, **1977**, Vol. 6, pp. 1-89.
31. Tatamitani, Y.; Liu, B.; Shimada, J.; Ogata, T.; Ottaviani, P.; Maris, A.; Caminati, W.; Alonso, J. L. *J. Am. Chem. Soc.* **2002**, *124*, 2739.

---

32. Hartwig, H.; Dreizler, H. *Z. Naturforsch A* **1996**, *51*, 923.

33. Xu, Y.; Jäger, W. *J. Chem. Phys.* **1997**, *106*, 7968.



\*\*\*\*\*

## CHAPTER 5

### INVESTIGATION OF $\text{PO}-(\text{H}_2\text{O})_{N=1-4}$ CLUSTERS: *AB INITIO*

#### CALCULATIONS AND ROTATIONAL SPECTRA

\*\*\*\*\*

#### 5.1 Introduction

Although it is difficult to define hydrogen (H)-bonds to include all the features ascribe to it, it is commonly accepted that the H-bond is an electrostatic interaction between electron-deficient H and a region of high electron density. The electron-deficient H atom is a proton donor; the region of high electron density is a proton acceptor, which is usually an electronegative atom such as fluorine, oxygen, or nitrogen. These interactions can occur between molecules (intermolecularly), or within different parts of a single molecule (intramolecularly). The strength of this bond lies inbetween van der Waals interactions and covalent bonds. The  $\text{Y}\cdots\text{H}-\text{X}$  type of H-bond having  $\text{X}, \text{Y} = \text{F}, \text{O}, \text{N}$  are the most frequently encountered H-bonds and are conventionally referred as primary or classic H-bonds.<sup>1, 2, 3</sup> Since early 1980s, significance of H-bonds formed by weak donors ( $\text{X} = \text{C}$ ) has arisen in many small molecule crystal structures.<sup>4, 5</sup> In recent years, interests about  $\text{O}\cdots\text{H}-\text{C}$  H-bonds in biochemistry have intensified as there is a large number of this weaker H-bonds in biomolecular systems, for example, work by Derewenda on proteins,<sup>6</sup> Sundaralingam on nucleic acids,<sup>7</sup> and Steiner on water.<sup>8</sup>

The interactions between water and chiral molecules are of significant interest since hydrogen (H)-bonding governs the solvation processes in the aqueous environments.<sup>1</sup> Water is one of the most abundant molecules on Earth and is essential for all living organisms. Since nearly all biological molecules required for life are chiral, knowledge about interactions between small chiral building blocks and water is a prerequisite to the understanding of chemistry of life.<sup>1</sup> Such knowledge is also of great importance for modeling stereoselective organic reactions in water because interactions between chiral molecules and water can significantly influence the synthetic outcome.<sup>9</sup> High resolution spectroscopy can in principle provide a detailed description of interactions between a chiral organic molecule and water molecules. In recent years, jet-cooled high resolution spectroscopy has been successfully applied to study a number of organic molecule–water adducts such as benzene–water,<sup>10</sup> phenol–water,<sup>11, 12</sup> ethylene oxide (EO)–water,<sup>13</sup> oxetane–water,<sup>14</sup> and tetrahydrothiophene–water.<sup>15</sup> These studies provided detailed and precise information about the structures of the H-bonded systems. On the other hand, there exists only a very small number of rotationally resolved spectroscopic publications on chiral molecule–water adducts. The studies of chiral molecule–water complexes are complicated by the large number of potential structural conformers and the dense spectral pattern since chiral molecules have  $C_1$  symmetry. Therefore size and conformational flexibility of the concerned chiral molecule need to be considered if attempting experimental and high level *ab initio* studies. Given this background, I am strongly motivated to study the PO–water complex using high resolution microwave spectroscopy.

For the PO–H<sub>2</sub>O dimer, attention will be focused on the O<sub>epoxy</sub>(from PO)⋯H–O (in water) type of H-bond and the effect of the additional interaction between the methyl group and H<sub>2</sub>O on the stability of structural conformers. Very recently, the role of the methyl groups in the formation of H-bonds in dimethyl sulfoxide–methanol mixtures was studied using attenuated total reflection FTIR spectroscopy, NMR spectroscopy, and *ab initio* methods.<sup>16</sup> A stabilizing contribution of the methyl groups to the intermolecular H-bonds through charge transfer was reported. Closely related to the current investigation are a number of rotationally resolved spectroscopic studies of ether–water complexes, such as EO–water,<sup>13</sup> 1,4-Dioxane–water,<sup>17</sup> and tetrahydropyran–water.<sup>18</sup> These studies were conducted by Caminati and co-workers using a pulsed-jet millimeter wave spectrometer and a FTMW spectrometer. In all these cases, only the lowest energy conformer could be detected experimentally. Investigations of the PO–water adduct provide the opportunity to probe the possible conformers in detail and to examine the effect of the methyl group on the stability of the O<sub>epoxy</sub>⋯H–O type of H-bond by comparing them with the closely related EO–water adduct.<sup>13</sup>

In addition, the strong chiral molecule–water (solute–solvent) interactions often have significant and non-intuitive effects on chiroptical measurements.<sup>19</sup> Interest in such interactions has intensified with the recent optical rotation studies by Vaccaro and co-workers.<sup>20,21</sup> Using a sensitive cavity ring down polarimeter, they measured the optical rotatory dispersion spectrum of the basic chiral building block, PO, in the gas phase for the first time. Surprisingly, the gas phase spectrum of PO resembles more closely the corresponding spectrum of PO in water than in benzene. This

observation is contrary to conventional wisdom since non-polar solvents were expected to mimic gas phase studies more appropriately than polar solvents. To explain the experimental observation, Mukhopadhyay *et al.* used molecular dynamics and time-dependent DFT methods to simulate the optical rotatory dispersion spectra of PO in water.<sup>22</sup> Their results showed that interestingly, the optical rotation response in such an environment is dominated by the binary PO–water complex rather than the PO monomer itself. The authors<sup>22</sup> drew the conclusion that water molecules have preference towards a particular position in binding to PO. These studies indicate the necessity of bridging the gap between the isolated binary PO–H<sub>2</sub>O complex and PO in bulk water in order to understand the intermolecular interactions taking place in an aqueous environment. Therefore, this chapter is devoted to the rotational spectroscopic and high level *ab initio* studies of PO sequentially solvated by a few water molecules in the gas phase.

## **5.2 *Ab initio* calculations**

### **5.2.1 PO–H<sub>2</sub>O**

#### **1) Geometry optimizations and analysis**

In terms of a conventional H-bond, PO can only act as a proton acceptor. Based on chemical intuition and the experimental results of other ether–water complexes,<sup>13, 18</sup> one may expect PO–H<sub>2</sub>O to form an O<sub>epoxy</sub>⋯H–O H-bond. To initially construct the geometry of PO–H<sub>2</sub>O complex, it is helpful to first examine the geometry of EO–H<sub>2</sub>O. EO is the smallest cyclic ether molecule, whose interaction with water has been investigated using millimeter wave spectroscopy. The lowest

energy structure of EO–H<sub>2</sub>O (shown in Figure 5-1) was determined to be the water molecule lying in the plane of symmetry of EO perpendicular to the ring and the water hydrogen involved in the H-bond points towards the ring oxygen.<sup>13</sup> Replacing one hydrogen atom of EO with a methyl group results in PO, one of the smallest cyclic ether chiral molecules. Since PO has no symmetry, two different H-bonding structures can be formed when the water molecule approaches PO from either side of the ether ring to interact with the lone electron pairs of the oxygen atom. In chemistry, the same side is conventionally referred to *syn*, and *anti* indicating the opposite side. Considering the steric hindrance effect from the methyl group, one may expect intuitively that water lying *anti* from the methyl group should be preferred.

To assist the spectral search and assignment, complete geometry optimizations were carried out using the GAUSSIAN03<sup>23</sup> software package at the MP2 level<sup>24</sup> with the following basis sets: 6-311++G(d,p),<sup>25</sup> cc-pVDZ,<sup>26</sup> and aug-cc-pVDZ.<sup>27</sup> Two minimum energy configurations, namely, *syn*-PO–H<sub>2</sub>O (i.e. H<sub>2</sub>O on the same side of the ring as the methyl group) and *anti*-PO–H<sub>2</sub>O (i.e. H<sub>2</sub>O approaching PO from the opposite direction of the methyl group with respect to the ether ring), were found with all three basis sets. Their minimum nature was confirmed by the absence of imaginary frequencies in the harmonic frequency calculations. The MP2/6-311++G(d,p) optimized structures of the complexes are shown in Figure 5-1 in their respective principal inertial axis systems. Cartesian coordinates for the two configurations of the PO–H<sub>2</sub>O complex obtained with the *ab initio* calculations are listed in Table A2-1 in Appendix 2.

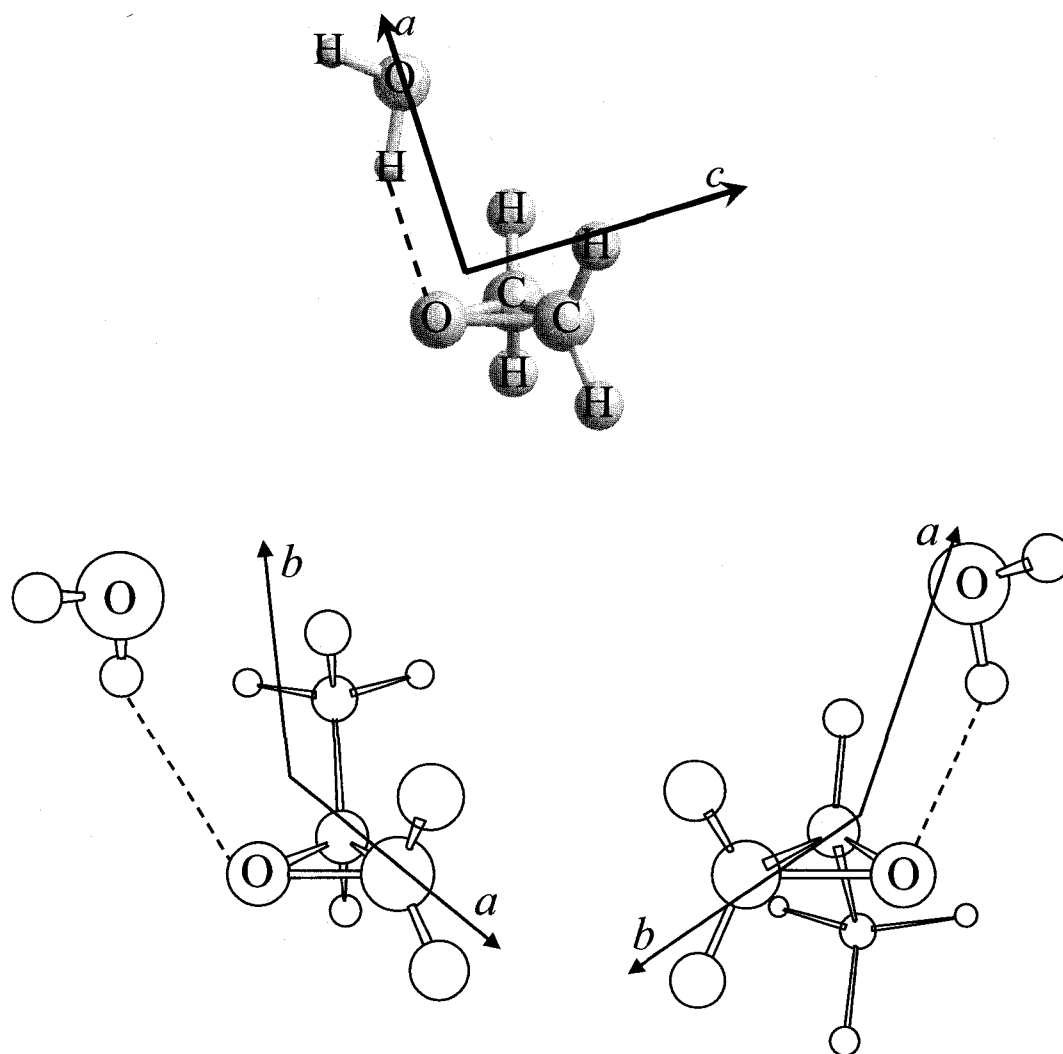


**Figure 5-1** Optimized geometries of the *syn*-PO-H<sub>2</sub>O (lower left) and *anti*-PO-H<sub>2</sub>O (lower right) conformers at the MP2/6-311++G(d,p) level of theory in their respective principal axis systems. The unlabeled elements are H and C atoms. The plausible conformation of the EO-H<sub>2</sub>O complex<sup>13</sup> is depicted (top) in its principal axis system for comparison.

In addition, geometry optimizations were also performed for the *entgegen* and *zusammen* positions<sup>13</sup> of the non-bonded water hydrogen with respect to the ether ring. The words, *entgegen* and *zusammen* are German meaning *opposite* and *together*,

respectively and correspond to the term *trans* and *cis* in chemistry notation. For both *syn*- and *anti*-configurations, the *zusammen* form always converges to the *entgegen* orientation during the geometry optimization procedures. In the study of EO–H<sub>2</sub>O, the *entgegen* form was calculated to be a local minimum in agreement with the experimental finding, while the *zusammen* form was found to be a saddle point that is 6.7 kJ/mol higher in energy than the *entgegen* form.<sup>13</sup> It is interesting to note that this preference of *entgegen* over *zusammen* is already known in the EO–H<sub>2</sub>O, 1,4-Dioxane–H<sub>2</sub>O, and tetrahydropyran–H<sub>2</sub>O complexes, by considering just the dipole-dipole interaction.<sup>13</sup> The dipole-dipole interaction energies can be calculated using the following expression:<sup>28</sup>

$$U_{\mu\mu} = -\frac{\mu_A \mu_B}{4\pi\epsilon_0 R_{CM}^3} [2 \cos \theta_A \cos \theta_B - \sin \theta_A \sin \theta_B \cos(\varphi_A - \varphi_B)] \quad (5-1)$$

where  $\mu_A$  and  $\mu_B$  are dipole moments of two subunits respectively. The direction of  $\mu_A$  is defined in a spherical coordinate system and described by the angles  $\theta_A$  and  $\varphi_A$ . The direction of  $\mu_B$  is described similarly by  $\theta_B$  and  $\varphi_B$  (see Figure 5-2).

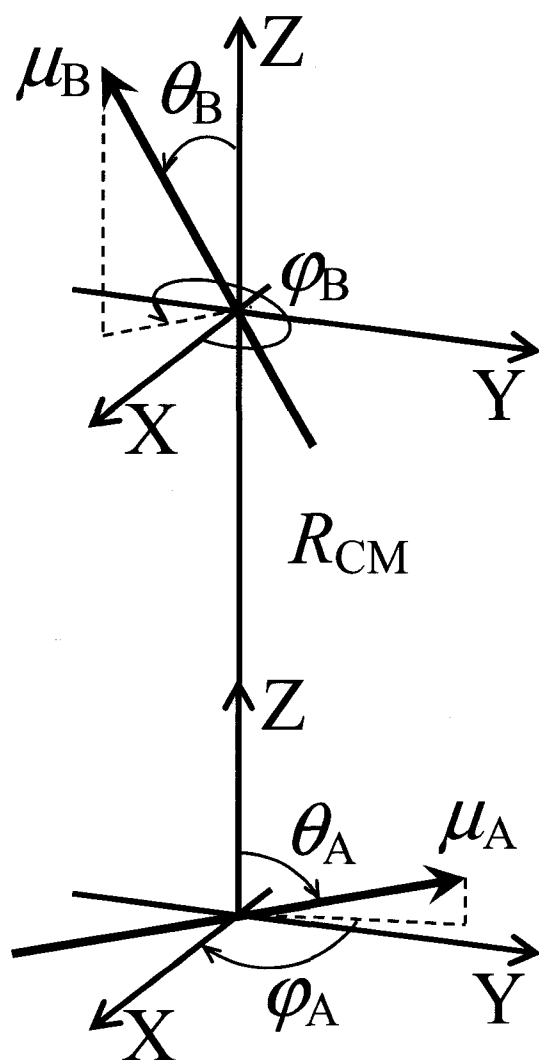


**Figure 5-2** The coordinate system for two dipoles  $\mu_A$  and  $\mu_B$  (redrawn from Figure 1.4 of Ref.28). The directions of dipoles are specified by azimuth angles,  $\theta$ , and zenith angles,  $\varphi$ .  $R_{CM}$  denotes the distance between the centres of mass of the two subunits.

Based on the MP2/6-311++G(d,p) geometries, the dipole-dipole interaction energies were calculated for the *entgegen* and *zusammen* forms of PO–H<sub>2</sub>O. The values of related parameters for EO–H<sub>2</sub>O and both conformers of PO–H<sub>2</sub>O are listed in Table 5-1. For *anti*-PO–H<sub>2</sub>O, the dipole-dipole interaction favours the *entgegen*



form over the *zusammen* one by 1.8 kJ/mol, just as in the cases of the other three ether–water complexes discussed above. For *syn*-PO–H<sub>2</sub>O, however, the opposite was found: the *zusammen* form is more stable by 1 kJ/mol than the *entgegen* form when only dipole-dipole interaction energies were considered. One plausible explanation for this behaviour is the steric hindrance effect of the methyl group in *syn*-PO–H<sub>2</sub>O that prevents the dipole moments of the two subunits to orient in a similar fashion as in EO–H<sub>2</sub>O or in *anti*-PO–H<sub>2</sub>O. The eventual effect of the *entgegen* form in *syn*-PO–H<sub>2</sub>O is therefore caused by other factors such as the additional secondary H-bonds between the methyl group and H<sub>2</sub>O, as will be discussed in a later section.

**Table 5-1** Calculated dipole-dipole interaction energies of the *entgegen* and *zusammen* forms of both *syn*- and *anti*-configurations of PO–H<sub>2</sub>O complex based on MP2/6-311++G(d,p) optimized geometries, together with the values of the EO–H<sub>2</sub>O complex for comparison.

	<i>syn</i> -PO–H <sub>2</sub> O		<i>anti</i> -PO–H <sub>2</sub> O		EO–H <sub>2</sub> O	
	<i>entgegen</i>	<i>zusammen</i>	<i>entgegen</i>	<i>zusammen</i>	<i>entgegen</i>	<i>zusammen</i>
$\mu_A$ /D	2.2569		2.2569		2.2569	
$\mu_B$ /D	2.4727		2.4727		2.4392	
$\theta_A$ /°	85.925	18.884	86.202	20.911	86.824	18.305
$\theta_B$ /°	54.436	55.264	61.407	61.998	65.964	66.842
$\phi^a$ /°	148.491	36.991	155.145	41.313	159.807	48.537
$R_{CM}$ /Å	3.1054		3.4053		3.0187	
$U_{\mu\mu}$ /kJmol <sup>-1</sup>	-8.690	-9.716	-7.305	-5.451	-10.858	-6.695

<sup>a</sup>  $\phi = (\phi_A - \phi_B)$ .

## 2) Dissociation energy

The binding energies calculated with MP2/6-311++G(d,p) for the *syn*- and *anti*-configurations are listed in Table 5-2. Also included in Table 5-2 are the basis set superposition errors (BSSEs) calculated with the counterpoise correction method<sup>29</sup> as described in Section 2.2.2 and the zero-point vibrational energy corrections for these two configurations. The zero-point vibrational corrected binding energies of the isotopically substituted complexes are calculated and summarized in Table 5-3. It has been shown that a complete basis set extrapolation gives a binding energy that is always bracketed by the BSSE corrected and uncorrected values as the BSSE tends to overcorrect the binding energies with small basis sets.<sup>30</sup> Therefore, an empirical 50% BSSE correction is also used here to help better estimate of the dissociation energies. The calculated results for EO–water are also listed in Table 5-2 for comparison. Both conformers of the PO–water adduct are predicted to be more strongly bound than the EO–water complex. While the uncorrected binding energy for *syn*-PO–H<sub>2</sub>O is 7.5 cm<sup>-1</sup> more than that of *anti*-PO–H<sub>2</sub>O, the final corrected binding energies are the same value for the two conformers. Results from calculations using other two different basis sets, cc-pVDZ and aug-cc-pVDZ are also included in Table 5-2. It is computationally too expensive to obtain the zero-point vibrational energy with the larger basis set, aug-cc-pVDZ. But from the calculations with the smaller ones, one can tell that zero point energy correction only changes the result marginally. Therefore, it is unknown *a priori* which conformer is more stable and has to be determined experimentally.

**Table 5-2** Calculated dissociation energies, counterpoise (CP) corrections for the basis set superposition error and zero-point vibrational energy ( $\Delta ZPE$ ) corrections in units of kJ/mol for the two conformers of the PO–H<sub>2</sub>O complex and the EO–H<sub>2</sub>O complex at the MP2 level of theory, with the three basis sets.

Basis set	<i>syn</i> -PO–H <sub>2</sub> O	<i>anti</i> -PO–H <sub>2</sub> O	EO–H <sub>2</sub> O
	6-311++G(d,p)		
$D_e$	-29.89	-29.80	-28.99
CP	7.02	6.80	6.83
$\Delta ZPE$	8.18	8.20	8.54
$D_0 = (D_e + \Delta ZPE)$	-21.71	-21.60	-20.45
$D_0 + 50\%CP$	-18.20	-18.20	-17.04
	cc-pVDZ		
$D_e$	-40.67	-39.13	
$D_0$	-30.69	-29.69	
	aug-cc-pVDZ		
$D_e$	-31.83	-31.81	

**Table 5-3** Calculated dissociation energies of the isotopically substituted conformers of the PO–H<sub>2</sub>O complex and the EO–H<sub>2</sub>O complex at the MP2/6-311++G(d,p) level of theory.

$D_0$ /kJmol <sup>-1</sup>	–DOD	–DOH	–HOD
EO	-22.12	-21.77	-20.91
<i>syn</i> -PO	-23.37	-23.03	-22.15
<i>anti</i> -PO	-23.27	-22.92	-22.06

### 3) Spectroscopic constants

Rotational constants and dipole moment components for the normal isotopomers of the two PO–H<sub>2</sub>O conformers from the *ab initio* calculations with all three basis sets are given in Table 5-4. The *anti*-configuration was predicted to be a

near prolate top with  $\kappa = -0.946$ , while the *syn*-configuration is a fairly asymmetric top with  $\kappa = -0.619$ . The prominent dipole moment component lies along the *a*-axis, while the magnitudes of the *b*- and *c*- dipole moments were predicted to be considerably smaller for both conformers with all three basis sets. The large difference in the rotational constant *A* (~3 GHz) between the two conformers suggests distinguishable spectral patterns for the two structures. However, it was noticed that the prediction from the three basis sets could differ up to 100 MHz, which means an even larger range for spectral searches. In the case of EO–water adduct,<sup>13</sup> the basis set 6-311++G(d,p) among all the trial basis sets gave the best agreement with the experimental results, with less than 50 MHz deviation. To confirm this point, similar comparison was made for the EO–water adducts including the deuterated species in Table 5-5. Therefore, the rotational constants of the isotopic species of PO–water complex were calculated with MP2/6-311++G(d,p) and listed in Table 5-6.

**Table 5-4** Predicted rotational constants and dipole moment components of the two conformers of the PO–H<sub>2</sub>O complex from the *ab initio* MP2 calculations.

	<i>syn</i> -PO–H <sub>2</sub> O			<i>anti</i> -PO–H <sub>2</sub> O		
	cc-pVDZ	6-311++G(d,p)	aug-cc-pVDZ	cc-pVDZ	6-311++G(d,p)	aug-cc-pVDZ
<i>A</i> /MHz	5897.39	6047.94	5915.99	9191.69	9488.04	9033.40
<i>B</i> /MHz	3292.64	3082.87	3199.63	2439.25	2310.28	2385.02
<i>C</i> /MHz	2513.07	2385.19	2445.80	2231.88	2112.86	2169.33
$\mu_a$ /D	2.05	2.04	1.92	2.14	1.79	1.65
$\mu_b$ /D	1.27	0.25	0.49	1.06	0.29	0.54
$\mu_c$ /D	0.14	0.06	0.38	0.80	0.08	0.28

**Table 5-5** Comparison between the experimental and the MP2/6-311++G(d,p) calculated rotational constants in the unit of MHz of the normal and isotopically substituted H<sub>2</sub>O conformers of the EO–water complex.

	<i>A</i>	<i>B</i>	<i>C</i>
EO–HOH			
Exp.	14827.5	3603.067	3486.472
Cal.	14834.06	3652.51	3534.59
$\Delta^a$	6.56	49.44	48.12
EO–DOH			
Exp.	14745.5	3556.990	3447.110
Cal.	14754.43	3598.24	3488.17
$\Delta^a$	8.93	41.25	41.06
EO–HOD			
Exp.	14719.3	3406.65	3305.022
Cal.	14763.19	3440.61	3339.39
$\Delta^a$	43.89	33.96	34.37
EO–DOD			
Exp.	14665.1	3367.974	3271.758
Cal.	14691.76	3395.77	3300.73
$\Delta^a$	26.66	27.80	28.97

<sup>a</sup> $\Delta = (ab\text{ initio constants}) - (\text{experimental constants})$ .

**Table 5-6** Calculated rotational constants for the isotopically substituted H<sub>2</sub>O conformers of the PO–water complex at the MP2/6-311++G(d,p) level of theory.

	<i>syn</i> -PO–			<i>anti</i> -PO–		
	DOH	HOD	DOD	DOH	HOD	DOD
<i>A</i> /MHz	6036.96	6035.28	6025.32	9450.43	9394.77	9362.20
<i>B</i> /MHz	3032.73	2907.83	2865.32	2274.15	2200.35	2168.96
<i>C</i> /MHz	2355.99	2280.84	2255.33	2083.71	2018.98	1993.48

**Table 5-7** Calculated harmonic frequencies in the unit of  $\text{cm}^{-1}$  of the vibrational bands of the water unit in the PO–water complex at the MP2/6-311++G(d,p) level of theory.

	asymmetric stretching <sup>a</sup>	symmetric stretching <sup>b</sup>	bending
HOH	4003	3885	1628
HOD	3946	2865	1427
DOD	2932	2802	1191
<i>syn</i> -PO–HOH	3963	3738	1661
<i>syn</i> -PO–DOD	2894	2706	1208
<i>syn</i> -PO–HOD	3756	2867	1488
<i>syn</i> -PO–DOH	3950	2728	1422
<i>anti</i> -PO–HOH	3965	3731	1659
<i>anti</i> -PO–DOD	2895	2702	1212
<i>anti</i> -PO–HOD	3749	2869	1492
<i>anti</i> -PO–DOH	3952	2723	1421

<sup>a</sup> The free O–H/D stretching in the complex.

<sup>b</sup> The hydrogen-bonded O–H/D stretching in the complex.

To further assist studies of the respective complexes using infrared laser spectroscopic methods, the harmonic frequencies of the OH bond involved in the H-bond was carried out at the MP2/6-311++G(d,p) level of theory. The symmetric and asymmetric OH/OD stretching bands in most cases shift by a few tens to a few hundreds of wavenumbers to lower frequency upon formation of the H-bond with PO. The water bending frequency is anticipated to shift to higher frequency upon complexation. The details are listed in Table 5-7.

### 5.2.2 PO–(H<sub>2</sub>O)<sub>2</sub>

Besides pure water clusters,<sup>31</sup> a fairly limited set of ternary clusters with two water molecules, such as HCOOH–(H<sub>2</sub>O)<sub>2</sub>,<sup>32</sup> Xe–(H<sub>2</sub>O)<sub>2</sub>,<sup>33</sup> CO<sub>2</sub>–(H<sub>2</sub>O)<sub>2</sub>,<sup>34</sup> HBr–

(H<sub>2</sub>O)<sub>2</sub>,<sup>35</sup> and more recently, formamide-(H<sub>2</sub>O)<sub>2</sub>,<sup>36</sup> have been studied using rotational spectroscopy. Based on the results of these complexes and the PO-H<sub>2</sub>O binary complex, it is expected that the most stable ternary structures have two primary O···H-O H-bonds since PO can only act as a proton acceptor in a classic H-bonding picture. Specifically, the two water molecules can approach PO from *syn*- and/or *anti*-directions with respect to the oxirane ring. To aid the spectral search and provide valuable hints on assignments, complete geometry optimizations of the PO-(H<sub>2</sub>O)<sub>2</sub> conformers were carried out at the level of MP2/6-311++G(d,p). Three most stable conformers of the PO-(H<sub>2</sub>O)<sub>2</sub> complex, namely, *syn*-PO-(H<sub>2</sub>O)<sub>2</sub>, *anti*-PO-(H<sub>2</sub>O)<sub>2</sub> and *bi*-PO-(H<sub>2</sub>O)<sub>2</sub>, have been located (see Figure 5-3).

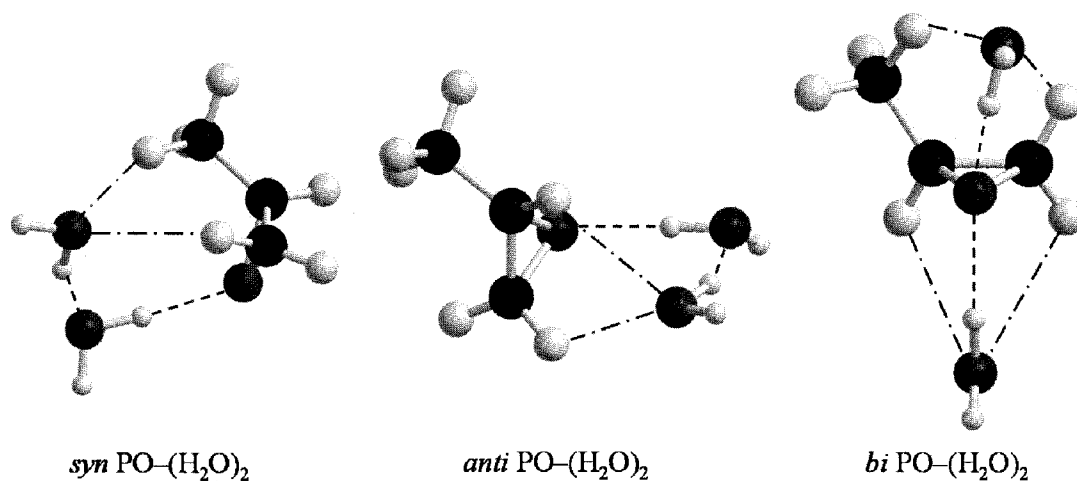


**Figure 5-3** Optimized geometries of the three most stable conformers of PO-(H<sub>2</sub>O)<sub>2</sub> obtained at the MP2/6-311++G(d,p) level of theory. Dashed and dot-dashed lines indicate the primary and secondary H-bondings, respectively. The *S*-form of PO is depicted.

The detailed structural coordinates from the *ab initio* calculations are listed in Table A2-2 in Appendix 2. Dashed and dot-dashed lines in Figure 5-3 indicate the primary and secondary H-bondings, respectively. The *S*-form of PO is depicted in Figure 5-3. For every *S*-PO-(H<sub>2</sub>O)<sub>2</sub> conformer, there is a mirror image *R*-PO-(H<sub>2</sub>O)<sub>2</sub> conformer and both give rise to the same rotational spectrum. *S*-PO is used throughout this study and, therefore, this notation is dropped for simplicity. The minimum nature of the structures shown in Figure 5-3 was confirmed with the harmonic frequency calculations. Subsequently the zero-point energies (ZPE) were obtained for the calculated dissociation energies. The basis set superposition error (BSSE) was calculated using the counterpoise correction methods of Boys and Bernardi.<sup>29</sup> The predicted dissociation energies, rotational constants and electric dipole moment components of the three conformers are summarized in Table 5-8. In addition to the three conformers shown in Figure 5-3, another group of structural isomers was also considered where one water molecule donates one of its H atoms to PO and its other H atom to the other water subunit simultaneously. Donating the first H atom reduces the electronic cloud density at the O atom and, therefore, significantly weakens its efficiency in donating its second H atom. Our calculations confirmed that this group of conformers are about 20 kJ/mol less stable than that of *syn*-PO-(H<sub>2</sub>O)<sub>2</sub>. They are therefore excluded from further considerations for experimental searches.

The *syn*- and *anti*-PO-(H<sub>2</sub>O)<sub>2</sub> conformers were predicted to be ~10 kJ/mol more stable than the *bi*-PO-(H<sub>2</sub>O)<sub>2</sub> conformer from their  $D_0$  values. The energy difference caused by the binding dissimilarity on the *syn*- and the *anti*-sides of PO is defined as the diastereofacial discrimination energy,<sup>7</sup>  $D_0(\textit{syn}) - D_0(\textit{anti})$ . This value is



about -0.73 kJ/mol for PO-(H<sub>2</sub>O)<sub>2</sub>. In a molecular jet expansion, one may expect the most stable conformer *syn*-PO-(H<sub>2</sub>O)<sub>2</sub> to be substantially more populated than the *anti*-conformer, while the much less stable *bi*-PO-(H<sub>2</sub>O)<sub>2</sub> conformer may not be populated enough to be detected experimentally. On the other hand, the predicted relative energy differences depend very much on whether one includes ZPE and/or BSSE corrections. In the case of the PO-H<sub>2</sub>O binary complex, the binding energy of the *syn*-PO-H<sub>2</sub>O conformer was found experimentally to be much larger than that of the *anti*-conformer, while the *ab initio* predictions had trouble to decipher the sign of the diastereofacial discrimination energy (refer to Section 5.5.2). Therefore, it is not known *a priori* which conformer is more stable and whether all the three conformers of the PO-(H<sub>2</sub>O)<sub>2</sub> complex will be observed experimentally.

**Table 5-8** Calculated dissociation energies ( $D_e$ ), ZPE corrected dissociation energies ( $D_0$ ), counterpoise corrected dissociation energies ( $D_0+CP$ ), rotational constants ( $A$ ,  $B$ ,  $C$ ) and electric dipole moment components ( $|\mu_{a,b,c}|$ ) of the three most stable conformers of PO-(H<sub>2</sub>O)<sub>2</sub> obtained at the MP2/6-311++G(d,p) level of theory.

	<i>syn</i> -PO-(H <sub>2</sub> O) <sub>2</sub>	<i>anti</i> -PO-(H <sub>2</sub> O) <sub>2</sub>	<i>bi</i> -PO-(H <sub>2</sub> O) <sub>2</sub>
$D_e$ /kJmol <sup>-1</sup>	-71.99	-70.78	-58.73
$D_0$ /kJmol <sup>-1</sup>	-52.92	-52.19	-42.57
$D_0+CP$ /kJmol <sup>-1</sup>	-33.59	-33.29	-26.14
$A$ /MHz	3223	3946	3457
$B$ /MHz	1807	1552	1576
$C$ /MHz	1602	1346	1257
$ \mu_a $ /D	0.60	0.63	0.13
$ \mu_b $ /D	0.06	0.46	0.00
$ \mu_c $ /D	0.59	0.54	0.64

### 5.2.3 PO-(H<sub>2</sub>O)<sub>3</sub> and PO-(H<sub>2</sub>O)<sub>4</sub>

Based on the above results of PO-(water)<sub>2</sub> and the previous studies of water trimer<sup>45</sup> and tetramer,<sup>46</sup> initial configurations of the PO-(water)<sub>3/4</sub> clusters were proposed for complete geometry optimizations. In total, five and eight local minima were found for PO-(water)<sub>3</sub> and PO-(water)<sub>4</sub> complexes, respectively. Their structures are displayed in Figure 5-4 and Figure 5-5. The labeling of **I**, **II**, **III**, etc, used in Figures 5-4 and 5-5, indicate the relative stability of the conformers. The predicted dissociation energies, rotational constants and electric dipole moment components of the conformers are summarized in Table 5-9 and Table 5-10 for the PO-(water)<sub>3</sub> and PO-(water)<sub>4</sub> complexes, respectively. The corresponding ZPEs are not available for the largest cluster, PO-(water)<sub>4</sub>. The two most stable structures of the PO-(water)<sub>3</sub> cluster are PO3w**I** and PO3w**II**, corresponding to *syn*-PO-(H<sub>2</sub>O)<sub>3</sub> and *anti*-PO-(H<sub>2</sub>O)<sub>3</sub>, following the nomenclature for the PO-(water)<sub>1/2</sub> system. PO3w**I** and PO3w**II** possess three primary H-bonds and one secondary H-bond, which tightly hold the four subunits in a five heavy atom-membered ring. The *syn*-conformation is predicted to be more stable than the *anti*-one based on their raw dissociation energies. It is of interest that the conformer with the cyclic ring structure of water trimer itself maintained, PO3w**V**, is the least favored conformer.

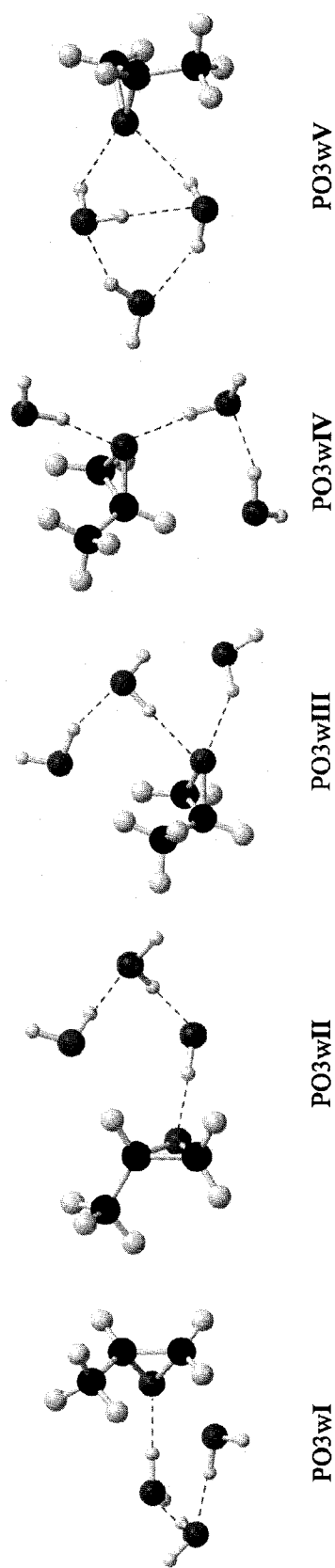


**Figure 5-4** Optimized geometries of five conformers of PO-(H<sub>2</sub>O)<sub>3</sub> cluster obtained at the MP2/6-311++G(d,p) level of theory. Dashed lines indicate the primary H-bondings. The order of labeling is based on their relative stability by comparing the raw dissociation energies

In the PO-(water)<sub>4</sub> cluster, the most stable structure seems to be the PO molecule locked by two primary H-bonds and a few secondary H-bonds. In PO4wI, the structure of tetra-water subunit changes slightly, from the structure before forming complex with PO, by pointing up the H atom of two consecutive water molecules to accommodate the solute molecule PO instead of alternating up and down in the subunit structure.

Although *syn*-(PO4wIV) and *anti*-(PO4wIII) configuration still exist as local minima, they are no longer the most stable conformers and also the energy difference between the two structures is very small, less than 1 kJ/mol. The above discussion imply that the PO-(H<sub>2</sub>O)<sub>4</sub> complex may be the transition point from microscopic hydration to macroscopic solvation.

Though extensive searches were carried out to look for all possible low energy conformers, it should be emphasized that the present *ab initio* results are preliminary and may be incomplete because of the large size of the clusters.

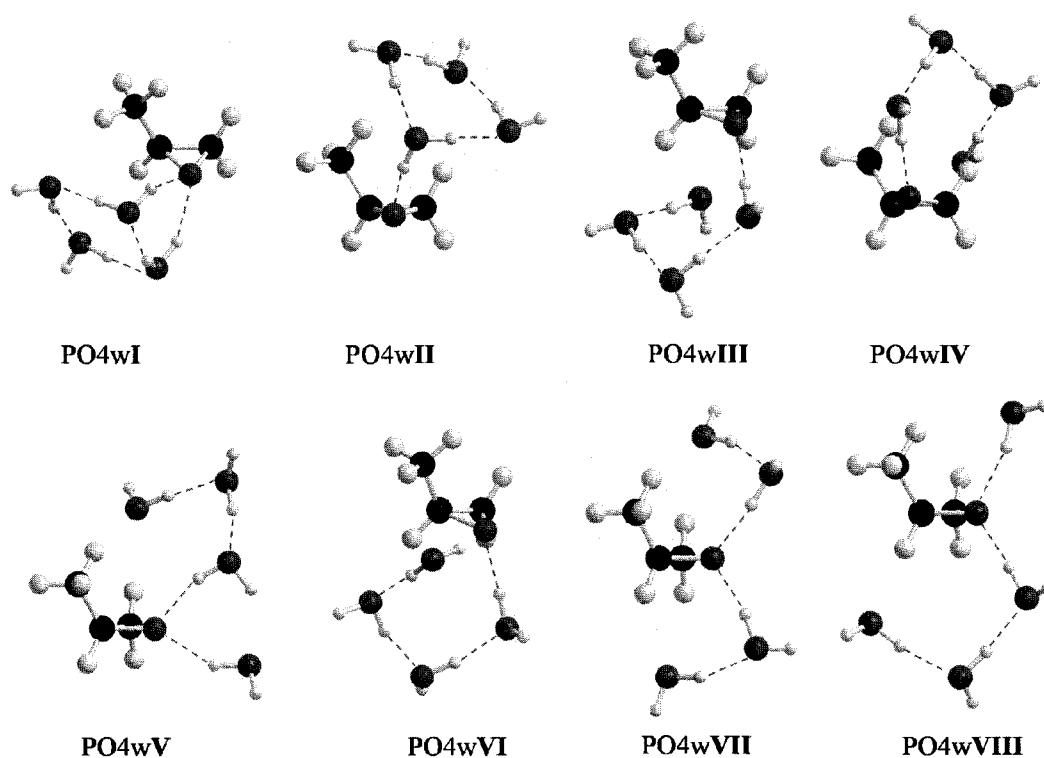


**Figure 5-5** Optimized geometries of eight conformers of PO-(H<sub>2</sub>O)<sub>4</sub> cluster obtained at the MP2/6-311++G(d,p) level of theory. Dashed lines indicate the primary H-bondings. The order of labeling is based on their relative stability by comparing the raw dissociation energies.

**Table 5-9** Calculated dissociation energies ( $D_e$ ), ZPE corrected dissociation energies ( $D_0$ ), rotational constants ( $A$ ,  $B$ ,  $C$ ) and electric dipole moment components ( $|\mu_{a,b,c}|$ ) of the five conformers of  $\text{PO}-(\text{H}_2\text{O})_3$  obtained at the MP2/6-311++G(d,p) level of theory. The corresponding geometry of each label is depicted in Figure 5-4.

	PO3wI	PO3wII	PO3wIII	PO3wIV	PO3wV
$D_e$ /kJmol <sup>-1</sup>	-114.19	-112.30	-102.52	-98.92	-98.26
$D_0$ /kJmol <sup>-1</sup>	-84.59	-82.68	-74.27	-72.19	-69.82
$A$ /MHz	2060	2112	1827	2496	2985
$B$ /MHz	1160	1051	1395	1014	926
$C$ /MHz	926	784	954	812	830
$ \mu_a $ /D	0.98	1.08	1.14	0.69	3.40
$ \mu_b $ /D	0.18	0.39	2.79	0.76	1.25
$ \mu_c $ /D	0.21	0.08	0.49	0.00	0.46

**Table 5-10** Calculated dissociation energies ( $D_e$ ), rotational constants ( $A$ ,  $B$ ,  $C$ ) and electric dipole moment components ( $|\mu_{a,b,c}|$ ) of the eight conformers of  $\text{PO}-(\text{H}_2\text{O})_4$  obtained at the MP2/6-311++G(d,p) level of theory. The corresponding geometry of each label is depicted in Figure 5-5.

	PO4wI	PO4wII	PO4wIII	PO4wIV
$D_e$ /kJmol <sup>-1</sup>	-161.65	-160.59	-152.26	-151.52
$A$ /MHz	1473	1467	1278	1199
$B$ /MHz	955	923	850	1106
$C$ /MHz	882	820	685	704
$ \mu_a $ /D	1.63	0.25	0.77	0.12
$ \mu_b $ /D	2.91	1.47	0.08	1.28
$ \mu_c $ /D	2.00	3.60	0.93	0.09
	PO4wV	PO4wVI	PO4wVII	PO4wVIII
$D_e$ /kJmol <sup>-1</sup>	-147.95	-146.01	-140.48	-140.06
$A$ /MHz	1162	1452	1849	1735
$B$ /MHz	1008	895	724	687
$C$ /MHz	635	752	618	534
$ \mu_a $ /D	2.53	0.81	0.13	0.59
$ \mu_b $ /D	2.26	2.66	0.46	1.04
$ \mu_c $ /D	0.33	3.58	0.55	0.54

### 5.3 Experimental details

To measure the PO–H<sub>2</sub>O dimer, a gas mixture of 0.14% H<sub>2</sub>O and 0.14% PO (99+%, Aldrich) in 5 bar of Ne (Praxair) was expanded through a pulsed pinhole nozzle. A molecular beam Fourier transform microwave spectrometer<sup>37</sup> operating in the frequency region between 4 and 18 GHz was used to measure the rotational spectra. The effective rotational temperature in the expansion was estimated to be lower than 1 K. Isotopically enriched D<sub>2</sub>O (99.8%, Cambridge Isotope Laboratories) was used for the investigation of the D<sub>2</sub>O containing isotopomers. The spectra of the isotopomers containing partially deuterated water were obtained in the same experiments with the D<sub>2</sub>O sample because fast proton exchange between D<sub>2</sub>O and residual H<sub>2</sub>O in the sample reservoir produced sufficient amounts of DOH after a few hours.

For PO–(H<sub>2</sub>O)<sub>2</sub> ternary cluster measurements, the gas sample mixture consisted of 0.18% H<sub>2</sub>O vapor and 0.09% PO in a helium (Praxair) carrier gas at a stagnation pressure of ~7 atm. Isotopically enriched H<sub>2</sub><sup>18</sup>O (70%, Aldrich) was used for the isotopic studies. The complexes were generated and stabilized in a supersonic expansion of the gas mixture through a General Valve (Series 9) pulsed nozzle with an orifice diameter of 0.8 mm. The estimated uncertainty of the frequency measurements is estimated to be about 2 kHz and the full linewidth at half height is about 18 kHz. The effective rotational temperature is estimated to be around 2.5 K.

## 5.4 Spectral search and assignment

### 5.4.1 PO–H<sub>2</sub>O

Initial spectral searches were carried out for the strong *a*-type transitions for the normal isotopomers of both conformers based on the *ab initio* predictions. Transitions for the *syn*-configuration were first observed. The frequency values are much closer to the 6-311++G(d,p) basis set prediction than the aug-cc-pVDZ one. Based on the observed extremely strong intensity of the *syn*-configuration (e.g., for the transition  $J_{K_a K_c} = 2_{02} - 1_{01}$ , signal-to-noise ratio is 17000 for 5 averaging cycles), it was promising to find the second structural isomer. The *anti*-configuration was finally observed with the corresponding transition intensity 9 times weaker than the *syn*-configuration. Similar to the case of the *syn*-configuration, the frequency values are very close to the prediction obtained from the 6-311++G(d,p) basis set. In total, rotational transitions with *J* up to 4 and *K<sub>a</sub>* up to 2 were found and assigned for both configurations. The initial fits with the *a*-type transitions were used to predict the much weaker *b*- and *c*-type transitions. Indeed, a few weak *b*- and one very weak *c*-type transitions were detected. The measured rotational transition frequencies for *syn*-PO–H<sub>2</sub>O and *anti*-PO–H<sub>2</sub>O are listed in Table A1-2 in Appendix 1. Although no Stark measurements were carried out for these complexes, it is possible to estimate roughly the magnitudes of the dipole moment components using the optimized microwave excitation pulse widths and the known dipole moment of OCS (0.7149 Debye).<sup>38</sup> The magnitude of the *a*-dipole moment component is about 2 Debye for both conformers. The magnitudes of the *b*- and *c*-dipole moment components are estimated to be in the order of one tenth of a Debye with the *b*-dipole moment component being slightly

larger. The above observations are in accord with the *ab initio* calculations. No splittings due to the internal rotation of the methyl group were observed for either *syn*-PO-H<sub>2</sub>O or *anti*-PO-H<sub>2</sub>O. It should be noted that fairly narrow tunnelling splittings of less than 2 kHz were predicted for *syn*-PO-H<sub>2</sub>O and less than 10 kHz for *anti*-PO-H<sub>2</sub>O with the XIAM internal rotation program,<sup>39</sup> assuming that the barrier height remains the same as in the monomer. Therefore, no concrete conclusion can be reached regarding the methyl internal rotation barrier height from the present study.

The searches and assignments for the other isotopomeric species followed the procedure described above. A summary of all the measured transition frequencies of the minor isotopomers are provided in Table A1-3. Small splittings of a few to about twenty kHz were observed in a number of transitions of the D containing isotopomers. These are due to the quadrupolar deuterium nucleus/nuclei (nuclear spin quantum number  $I_D=1$ ). No attempt was made to analyze these hyperfine structures in detail because the splittings were only partially resolved in most cases. The transition frequencies of the most intense components were used in the rotational fits in these cases. The uncertainties in these transition frequencies were estimated to be  $\pm 5$  kHz.

The measured rotational transition frequencies of all the isotopomeric species were fitted with Watson's *S*-reduction Hamiltonian in its  $I'$ -representation.<sup>40</sup> The resulting spectroscopic constants are summarized in Table 5-11 for both configurations. In the case of *anti*-PO-water, there is not enough information to fit both  $A$  and  $D_K$  because the system is a near prolate top. Therefore, the  $D_K$  values were fixed at 0.0 kHz for all the isotopomers.



**Table 5-11** Experimental rotational and centrifugal distortion constants of the parent and the deuterated isotopomers of the *syn*- and *anti*-configurations of PO–water complex.

	<i>syn</i> -configuration			
	PO–HOH	PO–DOH	PO–HOD	PO–DOD
<i>A</i> /MHz	6063.2695 (7) <sup>a</sup>	6051.271 (1)	6047.92 (4)	6036.849 (1)
<i>B</i> /MHz	3035.7424 (4)	2994.1636 (7)	2873.0355 (8)	2837.4176 (7)
<i>C</i> /MHz	2352.7137 (4)	2328.2062 (7)	2254.4995 (7)	2232.9386 (7)
<i>D<sub>J</sub></i> /kHz	5.99 (2)	5.76 (2)	4.93 (3)	4.80 (2)
<i>D<sub>JK</sub></i> /kHz	41.52 (5)	40.0 (2)	39.7 (5)	35.7 (2)
<i>D<sub>K</sub></i> /kHz	-88.6 (2)	-88.6 (-) <sup>b</sup>	-88.6 (-) <sup>b</sup>	-88.6 (-) <sup>b</sup>
<i>d<sub>1</sub></i> /kHz	-1.67 (1)	-1.66 (2)	-1.31 (2)	-1.20 (2)
<i>d<sub>2</sub></i> /kHz	-0.594 (7)	-0.34 (4)	-0.31 (-) <sup>c</sup>	-0.31 (4)
<i>N</i> <sup>d</sup>	15	10	7	10
$\sigma$ /kHz <sup>e</sup>	1.5	0.7	2.4	2.0
	<i>anti</i> -configuration			
	PO–HOH	PO–DOH	PO–HOD	PO–DOD
<i>A</i> /MHz	9478.8538 (4)	9446.634 (1)	9394.77 <sup>f</sup>	9356.674 (1)
<i>B</i> /MHz	2281.5644 (2)	2248.9839(9)	2177.438 (1)	2149.6736 (5)
<i>C</i> /MHz	2080.5421 (2)	2054.3828(8)	1993.6911 (8)	1969.9105 (4)
<i>D<sub>J</sub></i> /kHz	5.237 (5)	4.954(6)	4.67(3)	4.253 (8)
<i>D<sub>JK</sub></i> /kHz	-39.23 (3)	-36.5 (1)	-21.5 (3)	-33.7 (1)
<i>d<sub>1</sub></i> /kHz	-1.015 (4)	-1.13 (4)	0.01917 (4)	-0.53 (1)
<i>d<sub>2</sub></i> /kHz	-0.270 (7)	-3.5 (9)	-0.27 (-) <sup>b</sup>	-0.27 (-) <sup>b</sup>
<i>N</i>	19	12	6	11
$\sigma$ /kHz	4.4	3.0	3.3	7.3

<sup>a</sup> Standard error in parentheses are expressed in units of the last digits.

<sup>b</sup> Fixed at the corresponding value of the parent species.

<sup>c</sup> Fixed at the corresponding value of the DOD species.

<sup>d</sup> Number of transitions in the fit.

<sup>e</sup> rms deviation of the fit.

<sup>f</sup> Fixed at the corresponding value from the MP2/6-311++G(d,p) calculations.

The standard deviations of the fits for *anti*-PO–H<sub>2</sub>O are therefore slightly larger than for *syn*-PO–H<sub>2</sub>O where all five quartic centrifugal distortion constants were fitted independently. Some distortion constants of the minor isotopomers had to be fixed at the corresponding values of the normal or related isotopomers due to the less extensive data set available. From normal water species to D<sub>2</sub>O, the centrifugal distortion constants decreased, indicating more strongly bound complex with growing mass. This trend is due to the lower zero-point energy associated with heavier species. In general, the MP2 calculations with the 6-311++G(d, p) basis sets gave the best agreement with the experimental rotational constants, with consistent deviations for all isotopomeric species of both *syn*- and *anti*-configurations. The largest deviation is about 1.5% with MP2/6-311++G(d, p), while the deviation is 8.5% with MP2/cc-pVDZ and 5.4% with MP2/aug-cc-pVDZ. The details are summarized in Table 5-12.

**Table 5-12** Comparison between the experimental and the *ab initio* rotational constants of the normal and isotopically substituted conformers of the PO–water complex. The relative deviation from the experimental values is listed in parenthesis.

Basis set	6-311++G(d,p)			
	<i>syn</i> -configuration		<i>anti</i> -configuration	
	PO–H <sub>2</sub> O	PO–D <sub>2</sub> O	PO–H <sub>2</sub> O	PO–D <sub>2</sub> O
$\Delta A$ /MHz	-15 (-0.2%)	-12 (-0.2%)	9 (0.1%)	5 (0.1%)
$\Delta B$ /MHz	47 (1.5%)	28 (1.0%)	29 (1.3%)	19 (0.9%)
$\Delta C$ /MHz	32 (1.4%)	22 (1.0%)	32 (1.5%)	23 (1.2%)
Basis set	aug-cc-pVDZ			
	<i>syn</i> -configuration		<i>anti</i> -configuration	
	PO–H <sub>2</sub> O	PO–D <sub>2</sub> O	PO–H <sub>2</sub> O	PO–D <sub>2</sub> O
$\Delta A$ /MHz	-147 (-2.4%)	-141 (-2.3%)	-445 (-4.7%)	-422 (-4.5%)
$\Delta B$ /MHz	164 (5.4%)	139 (4.9%)	103 (4.5%)	89 (4.1%)
$\Delta C$ /MHz	93 (4.0%)	82 (3.7%)	89 (4.3%)	78 (4.0%)

#### 5.4.2 PO-(H<sub>2</sub>O)<sub>2</sub>

To maximize the chance to observe all three conformers, helium was chosen as the carrier gas for initial searches and neon was used only in the final step to confirm the assignment. The ground vibrational state of the PO monomer was investigated thoroughly with rotational spectroscopy. Therefore the corresponding transitions can be easily identified and excluded.<sup>41, 42, 43</sup> Water clusters have only very few rotational transitions in the targeted frequency region, due to the rotation-tunneling motion in the water dimer.<sup>44, 45, 46</sup> Any lines not belonging to the PO containing clusters were identified using a sample without PO. Even with all the information available from substantial previous spectroscopic work of related molecular systems, it was still not straightforward to recognize the *a*-type transition patterns of the PO-(H<sub>2</sub>O)<sub>2</sub> ternary cluster. The main reason is that all the conformers are highly asymmetric tops, with asymmetry parameter  $\kappa$  being -0.75, -0.84 and -0.71 for *syn*, *anti*- and *bi*-PO-(H<sub>2</sub>O)<sub>2</sub>, respectively. In addition, it was tricky to optimize the water concentration in the gas phase for the observation of the targeted molecular system. Fluctuations in concentration often result in large changes of line intensities observed, making it challenging to carry out the assignments. The initial search and assignment for the *J*=3-2 stack of the *anti*-conformer was successful after substantial trial and error. In total, twenty-one *a*-type transitions were measured for *anti*-PO-(H<sub>2</sub>O)<sub>2</sub>, and nineteen for *syn*-PO-(H<sub>2</sub>O)<sub>2</sub>. The *anti*-conformer was found to be twice as strong as the *syn*-conformer on average. No fine splittings due to the internal rotation of the methyl group or the tunneling motions of water subunits were observed for either conformer. There are a number of lines measured in the 4-9 GHz region, which could be ascribed

to the PO+H<sub>2</sub>O cluster using a sample mixture in both Ne and He. None of them could be assigned satisfactorily to the *bi*-PO-(H<sub>2</sub>O)<sub>2</sub> conformer. Further efforts were made to search for this third conformer using much longer MW pulse widths than the one optimized for *syn*- or *anti*-PO-(H<sub>2</sub>O)<sub>2</sub>, considering the much smaller  $\mu_a$  dipole moment component predicted.<sup>38</sup> The search for the stronger *c*-type transitions of *bi*-PO-(H<sub>2</sub>O)<sub>2</sub> yielded no assignment either. It is suspected that this higher energy conformer is not populated substantially in the molecular expansion. A list of mystery lines, which are confirmed belonging to PO containing system, is given in Table A1-4 for future interests.

To confirm the identity of the molecular systems assigned, further experiments with an isotopically enriched H<sub>2</sub><sup>18</sup>O sample (70%) were performed. Because H<sub>2</sub><sup>16</sup>O is present in the enriched H<sub>2</sub><sup>18</sup>O sample, one may expect four different isotopomers with H<sub>2</sub><sup>16</sup>O-H<sub>2</sub><sup>16</sup>O, H<sub>2</sub><sup>18</sup>O-H<sub>2</sub><sup>18</sup>O, H<sub>2</sub><sup>18</sup>O-H<sub>2</sub><sup>16</sup>O, and H<sub>2</sub><sup>16</sup>O-H<sub>2</sub><sup>18</sup>O for both *anti*-PO-(H<sub>2</sub>O)<sub>2</sub> and *syn*-PO-(H<sub>2</sub>O)<sub>2</sub>. On the other hand, deuterium substitution on H<sub>2</sub>O is expected to produce in 16 (2×2×2×2) different isotopomers for each conformer, resulting in very crowded spectral pattern. Therefore no effort has been made to measure the spectra of deuterated species. The initial rotational constants for the rare isotopomers containing <sup>18</sup>O were predicted using the calculated geometries and the corresponding shifts between the experimental and calculated rotational constants of the H<sub>2</sub><sup>16</sup>O-H<sub>2</sub><sup>16</sup>O parent isotopomer. It is relatively straightforward to locate the transitions for these rarer isotopomers. Only the mixed clusters, i.e. H<sub>2</sub><sup>18</sup>O-H<sub>2</sub><sup>16</sup>O and H<sub>2</sub><sup>16</sup>O-H<sub>2</sub><sup>18</sup>O of the *syn*-conformer were not located, possibly because of much weaker signal for the *syn*-conformer than the *anti*-one.

A summary of all measured rotational transition frequencies of the *syn*- and *anti*-conformers are listed in Table A1-5. They were fitted to a Watson's *A*-reduction semirigid rotor Hamiltonian in its *I'*-representation.<sup>40</sup> The resulting spectroscopic constants of all the isotopomers are listed in Table 5-13. The standard deviations of the spectroscopic fits are a few kHz, in good agreement with the experimental uncertainty. The calculated rotational constants agree reasonably well with the experimentally determined values, with the largest deviation being about 3.6%.

**Table 5-13** Experimental spectroscopic constants<sup>a</sup> of the two PO-(H<sub>2</sub>O)<sub>2</sub> conformers, including both normal and H<sub>2</sub><sup>18</sup>O isotopomers.

Conformers	<i>syn</i> -H <sub>2</sub> <sup>16</sup> O-H <sub>2</sub> <sup>16</sup> O		<i>syn</i> -H <sub>2</sub> <sup>18</sup> O-H <sub>2</sub> <sup>18</sup> O		<i>anti</i> -H <sub>2</sub> <sup>16</sup> O-H <sub>2</sub> <sup>16</sup> O	
<i>A</i> /MHz	3200.394(8)	3223 <sup>b</sup>	3049.352(5)	3070	3846.901(8)	3946
<i>B</i> /MHz	1744.6903(5)	1807	1660.8805(3)	1720	1529.8990(4)	1552
<i>C</i> /MHz	1556.9635(4)	1602	1461.1292(3)	1504	1311.7199(4)	1346
$\Delta_J$ /kHz	2.067(5)		1.793(3)		1.351(3)	
$\Delta_{JK}$ /kHz	5.74(3)		5.77(2)		8.14(2)	
$\delta_J$ /kHz	0.077(3)		0.106(2)		0.142(2)	
$\delta_k$ /kHz	0.2(2)		-1.91(9)		-12.6(1)	
<i>N</i>	20		24		23	
$\sigma$ /kHz	1.6		1.8		4.8	
Conformers	<i>anti</i> -H <sub>2</sub> <sup>18</sup> O-H <sub>2</sub> <sup>18</sup> O		<i>anti</i> -H <sub>2</sub> <sup>18</sup> O-H <sub>2</sub> <sup>16</sup> O		<i>anti</i> -H <sub>2</sub> <sup>16</sup> O-H <sub>2</sub> <sup>18</sup> O	
<i>A</i> /MHz	3622.441(8)	3715	3752.30(1)	3846	3723.46(1)	3821
<i>B</i> /MHz	1457.7134(4)	1479	1490.570(1)	1511	1492.464(1)	1516
<i>C</i> /MHz	1234.3055(3)	1266	1273.096(1)	1305	1270.017(2)	1305
$\Delta_J$ /kHz	1.201(3)		1.42(2)		1.16(2)	
$\Delta_{JK}$ /kHz	7.81(2)		7.50(9)		7.61(9)	
$\delta_J$ /kHz	0.128(2)		0.148(3)		0.126(3)	
$\delta_k$ /kHz	-10.2(1)		-2.7(6)		-18.5(6)	
<i>N</i>	23		17		17	
$\sigma$ /kHz	3.1		2.3		2.4	

<sup>a</sup>  $\Delta_K$  was fixed at 0.0 in all fits. <sup>b</sup> MP2/6-311++G(d,p) calculations for comparison.

Although no Stark measurements were carried out for these conformers, it was able to get a rough estimate for the magnitude of the dipole moment components from the optimized microwave excitation pulse widths.  $\mu_a$  is estimated to be around 0.5~1.0 Debye for both conformers, in accord with the MP2/6-311++G(d,p) calculations. Since the two conformers are both highly asymmetric tops, the  $A$  rotational constants are well determined from the  $a$ -type transition fits, leading to fairly precise predictions of the  $b$ - and  $c$ -type transitions. However, no  $b$ - or  $c$ -type transitions were observed for either conformer. This indicates that the dipole moment components,  $\mu_b$  and  $\mu_c$ , for both the *syn*- and *anti*-configurations are much smaller than  $\mu_a$ . This observation is contradictory to the *ab initio* predictions that  $\mu_c$  of *syn*-PO-(H<sub>2</sub>O)<sub>2</sub>, and  $\mu_b$  and  $\mu_c$  of *anti*-PO-(H<sub>2</sub>O)<sub>2</sub> are of similar magnitude to  $\mu_a$  in these two conformers.

## 5.5 Discussion

### 5.5.1 Structural analysis

#### 1) PO-H<sub>2</sub>O

To analyze the relative orientation of the two subunits in the respective structural conformers, the experimental rotational constants were used in the structural fitting procedures. In these fits, the structures of water and PO were assumed to be unchanged upon complex formation and the experimental structural parameters for PO<sup>41</sup> and water<sup>47</sup> were used. This is a reasonable assumption since the *ab initio* calculations suggested little changes of the structures of the two monomers upon formation of the complex. Six additional structural parameters (defined in Figure 5-6) are needed to describe the relative orientation of the two monomers. These are the

three parameters for the H-bonded hydrogen atom of H<sub>2</sub>O:  $r$  (H-bonding length O<sub>epoxy</sub>⋯H),  $\tau$  [ $\angle$ (C<sub>m</sub>-O<sub>epoxy</sub>⋯H)], and  $\theta_1$  [ $\angle$ (C<sub>2</sub>-C<sub>m</sub>-O<sub>epoxy</sub>⋯H)]; the two parameters for the O atom:  $\phi$  [ $\angle$ (O<sub>epoxy</sub>⋯H-O)] and  $\theta_2$  [ $\angle$ (C<sub>m</sub>-O<sub>epoxy</sub>⋯H-O)]; and the dihedral angle  $\theta_3$  [ $\angle$ (O<sub>epoxy</sub>⋯H-O-H)] for the non-bonded hydrogen atom. C<sub>m</sub> denotes the midpoint of the C<sub>2</sub>-C<sub>3</sub> bond. In the case of *syn*-PO-H<sub>2</sub>O,  $\theta_2$  was fixed at the *ab initio* value during the structural fit.

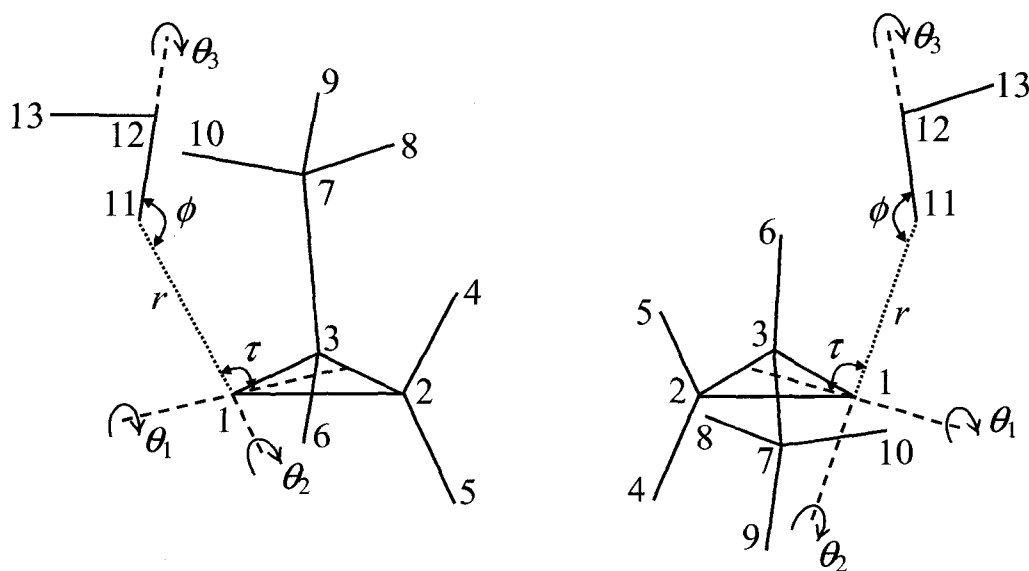


**Figure 5-6** Definition of the H-bonding parameters for the *syn*-PO-H<sub>2</sub>O (left) and the *anti*-PO-H<sub>2</sub>O (right) conformers.

The results are reported in Table 5-14, together with the corresponding values from the *ab initio* calculations for comparison. To facilitate comparison with other ether-water complexes, the values for  $\angle$ (ring-O<sub>epoxy</sub>⋯H) and  $R_{CM}$  were then calculated from the obtained structures of both conformers and are also listed in Table

5-14. From Table 5-14, one can see that the intermolecular H-bonding angles  $\angle(\text{ring-O}_{\text{epoxy}}\cdots\text{H})$  and  $\phi$  are similar for *anti*-PO-H<sub>2</sub>O and EO-H<sub>2</sub>O. This is not surprising considering the only difference between EO and PO is an additional methyl group, which is on the opposite side of the H-bond in *anti*-PO-H<sub>2</sub>O. Therefore, the effect of the methyl group is not expected to be dramatic. In contrast, the H-bonding angle  $\phi$  is much closer to linearity for *syn*-PO-H<sub>2</sub>O as compared to *anti*-PO-H<sub>2</sub>O and EO-H<sub>2</sub>O, implying the dramatic effect of the methyl group in steric repulsion towards the water entity.

**Table 5-14** Experimental and MP2/6-311++G(d,p) H-bonding structural parameters of the PO-H<sub>2</sub>O complex, together with the experimental values of the EO-H<sub>2</sub>O complex for comparison.

	<i>syn</i> -PO-H <sub>2</sub> O		<i>anti</i> -PO-H <sub>2</sub> O		EO-H <sub>2</sub> O <sup>a</sup>
	Exp.	Theo.	Exp.	Theo.	Exp.
$r/\text{\AA}$	1.908 (7) <sup>b</sup>	1.905	1.885 (2)	1.900	1.92 (1)
$\tau/\text{deg}$	110 (1)	115.4	103.7 (3)	106.7	103 (1)
$\phi/\text{deg}$	177 (2)	158.2	161.7 (6)	153.1	163 (2)
$\theta_1/\text{deg}$	80.0 (9)	80.1	-94.5 (4)	-89.3	90.0
$\theta_2/\text{deg}$	-10.0 <sup>c</sup>	-10.0	51 (5)	-0.3	0.0
$\theta_3/\text{deg}$	-157 (9)	-168.6	-233 (4)	-179.4	-180.0
$R_{\text{CM}}/\text{\AA}^{\text{d}}$	3.15	3.105	3.45	3.405	2.84
$\angle(\text{ring-O}_{\text{epoxy}}\cdots\text{H})/\text{deg}^{\text{d}}$	112	117.1	104.3	106.7	103

<sup>a</sup> Ref. 13. The  $\theta$  angles are fixed by the symmetry of the complex.

<sup>b</sup> Experimental uncertainties in parenthesis are in units of the last digit.

<sup>c</sup> Fixed at the corresponding theoretical value. See text for detail.

<sup>d</sup> Calculated from the respective derived structures.



## 2) PO-(H<sub>2</sub>O)<sub>2</sub>

Using the experimental isotopic rotational constants and the Kraitchman equations listed as following,<sup>48</sup> the coordinates of the two oxygen atoms of water in the principal axis system were derived to be (2.070, -1.290, -0.307) and (2.033, 1.521, -0.076) in *anti*-PO-(H<sub>2</sub>O)<sub>2</sub>.

$$\begin{aligned}
 |x| &= \left[ \frac{\Delta P_x}{\mu} \left( 1 + \frac{\Delta P_y}{I_x - I_y} \right) \left( 1 + \frac{\Delta P_z}{I_x - I_z} \right) \right]^{1/2} \\
 |y| &= \left[ \frac{\Delta P_y}{\mu} \left( 1 + \frac{\Delta P_z}{I_y - I_z} \right) \left( 1 + \frac{\Delta P_x}{I_y - I_x} \right) \right]^{1/2} \\
 |z| &= \left[ \frac{\Delta P_z}{\mu} \left( 1 + \frac{\Delta P_x}{I_z - I_x} \right) \left( 1 + \frac{\Delta P_y}{I_z - I_y} \right) \right]^{1/2}
 \end{aligned} \tag{5-2}$$

where

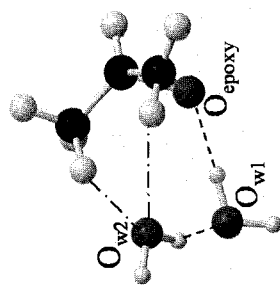
$$\begin{aligned}
 \Delta P_x &= \frac{1}{2} (-\Delta I_x + \Delta I_y + \Delta I_z) \\
 \Delta P_y &= \frac{1}{2} (-\Delta I_y + \Delta I_z + \Delta I_x) \\
 \Delta P_z &= \frac{1}{2} (-\Delta I_z + \Delta I_x + \Delta I_y)
 \end{aligned} \tag{5-3}$$

The relative signs of the coordinates were chosen based on the predicted structures. From these values, the distance between the two oxygen atoms in the two water molecules,  $r(\text{O}_{w1}-\text{O}_{w2})$ , is determined to be 2.82 Å. We noted that, in PO-(H<sub>2</sub>O)<sub>2</sub>, the spatial orientations of the two lone electron pairs of the O<sub>epoxy</sub> atom dictate the directions of the primary O<sub>epoxy</sub>⋯H-O<sub>w1</sub> H-bonding, similar to that in the binary PO-H<sub>2</sub>O complex. From the good agreement between the experimental and predicted rotational constants, one can infer that the actual geometries of the PO-(H<sub>2</sub>O)<sub>2</sub> ternary

conformers are close to the calculated results. For example, the calculated  $r(\text{O}_{\text{w1}}-\text{O}_{\text{w2}})$  is 2.79 Å, in reasonable agreement with the corresponding experimental value of 2.82 Å. The important structural parameters of the H-bonding lengths,  $r(\text{O}_{\text{epoxy}}\cdots\text{H})$  and  $r(\text{O}_{\text{w1}}\cdots\text{H})$ , H-bonding angles,  $\angle(\text{O}_{\text{epoxy}}\cdots\text{H}-\text{O}_{\text{w1}})$  and  $\angle(\text{O}_{\text{w1}}\cdots\text{H}-\text{O}_{\text{w2}})$ , of these two conformers are listed in Table 5-15. Also listed in Table 5-15 are the corresponding parameters of the PO–H<sub>2</sub>O complex and the water dimer. The experimentally determined structural parameters are also included in Table 5-15.<sup>44</sup> While the structural parameters of the (H<sub>2</sub>O)<sub>2</sub> subunit in the *syn*- and *anti*-PO–(H<sub>2</sub>O)<sub>2</sub> conformers are almost the same, they differ noticeably from those of the pure (H<sub>2</sub>O)<sub>2</sub>.  $r(\text{O}_{\text{w1}}\cdots\text{H})$  and  $r(\text{O}_{\text{w1}}-\text{O}_{\text{w2}})$  are about 0.1 to 0.2 Å shorter in PO–(H<sub>2</sub>O)<sub>2</sub> than in (H<sub>2</sub>O)<sub>2</sub>, while the H-bonding angle  $\angle(\text{O}_{\text{w1}}\cdots\text{H}-\text{O}_{\text{w2}})$  deviates further from linearity in PO–(H<sub>2</sub>O)<sub>2</sub> than in (H<sub>2</sub>O)<sub>2</sub>. It can be suggested that these changes are made in order to maximize the interactions between water and PO, that is to best solvate the PO molecule with water molecules. It was also noted that  $r(\text{O}_{\text{epoxy}}\cdots\text{H})$  of the primary H-bond between PO and water is about 0.1 Å shorter in the ternary PO–(H<sub>2</sub>O)<sub>2</sub> cluster than in the binary PO–H<sub>2</sub>O complex. Furthermore, the secondary H-bonds O<sub>w2</sub>⋯H–C effectively lock the oxygen atom of the second water in a specific position, with the  $r(\text{O}_{\text{w2}}\cdots\text{H}-\text{C})$  values being 2.44 and 2.54 Å in *syn*-PO–(H<sub>2</sub>O)<sub>2</sub>, 2.54 and 2.65 Å in *anti*-PO–(H<sub>2</sub>O)<sub>2</sub>. They are considerably shorter than the corresponding distance of 2.71 Å in the *syn*-PO–H<sub>2</sub>O binary conformer. Overall, the ternary PO–(H<sub>2</sub>O)<sub>2</sub> molecular clusters is more tightly bound through the two primary H-bonds and two secondary H-bonds than the corresponding binary systems.

**Table 5-15** Important structural parameters of the two observed conformers of PO-(H<sub>2</sub>O)<sub>2</sub> obtained at the MP2/6-311++G(d,p) level of theory, together with the corresponding values of the PO-H<sub>2</sub>O and (H<sub>2</sub>O)<sub>2</sub> complexes. The available experimental values are given in parenthesis.

Conformer	<i>syn</i> -PO-(H <sub>2</sub> O) <sub>2</sub>	<i>anti</i> -PO-(H <sub>2</sub> O) <sub>2</sub>	<i>syn</i> -PO-H <sub>2</sub> O	<i>anti</i> -PO-H <sub>2</sub> O	(H <sub>2</sub> O) <sub>2</sub> <sup>a</sup>
$r(\text{O}_{\text{epoxy}} \cdots \text{H}) / \text{\AA}$	1.808	1.800	1.905 (1.908)	1.900 (1.885)	-
$r(\text{O}_{\text{w1}} \cdots \text{H}) / \text{\AA}$	1.869	1.868	-	-	1.952
$r(\text{O}_{\text{w1}}-\text{O}_{\text{w2}}) / \text{\AA}$	2.789	2.784 (2.82)	-	-	2.918 (2.98)
$\angle(\text{O}_{\text{epoxy}} \cdots \text{H}-\text{O}_{\text{w1}}) / ^\circ$	168.9	166.2	158.2 (177)	153.1 (161.7)	-
$\angle(\text{O}_{\text{w1}} \cdots \text{H}-\text{O}_{\text{w2}}) / ^\circ$	157.0	156.4	-	-	178.4



<sup>a</sup> Ref. 44.

## 5.5.2 Conformational stability and hydrogen bonding strength

### 1) PO–H<sub>2</sub>O

The intermolecular H-bonding strength can be measured using the corresponding stretching force constant estimated with a model developed by Read *et al.*<sup>49</sup> The experimental rotational and centrifugal distortion constants were used in Equation 5-4<sup>49</sup> to calculate the stretching force constant, provided that the stretching coordinate is near-parallel to the *a*-axis. In the cases of the two PO–H<sub>2</sub>O conformers, this condition is approximately satisfied because based on the *ab initio* calculations the angle between the *a*-axis and the intermolecular O··H bond is 20.4° and 18.8° for the *syn*- and *anti*-configurations, respectively. In Equation 5-4:

$$k_S = 16\pi^4 (\mu R_{CM})^2 \left[ (B^2 + C^2)^2 + 2(B^4 + C^4) \right] / hD_J \quad (5-4)$$

$\mu$  is the reduced mass of the complex, *B*, *C* and *D<sub>J</sub>* are the spectroscopic constants listed in Tables 5-13, and *R<sub>CM</sub>* is the separation between the centres-of-mass of the two subunits, listed in Table 5-14. The related vibrational frequency,  $\nu_s$ , can be calculated using Equation 5-5:<sup>50</sup>

$$\nu_S = 1 / 2\pi (k_S / \mu)^{1/2} \quad (5-5)$$

The binding energy,  $\Delta E$ , can then be estimated using Equation 5-6, assuming a Lennard-Jones potential function:<sup>50</sup>

$$\Delta E = (1 / 72) k_S R_{CM}^2 \quad (5-6)$$

The results are summarized in Table 5-16 together with the corresponding values for EO–H<sub>2</sub>O<sup>13</sup> and H<sub>2</sub>O–H<sub>2</sub>O.<sup>44</sup> The harmonic frequencies from the MP2/6-311++G(p,d)

calculations, scaled with an empirical factor 0.97, are also included in Table 5-16 for comparison.

**Table 5-16** Comparison of the H-bonding force constants, stretching frequencies, and binding energies for several water containing complexes. The harmonic frequencies were calculated based on the MP2/6-311++G(d,p) geometries and are scaled by a factor of 0.97.

	<i>syn</i> -PO-H <sub>2</sub> O	<i>anti</i> -PO-H <sub>2</sub> O	EO-H <sub>2</sub> O <sup>a</sup>	H <sub>2</sub> O-H <sub>2</sub> O <sup>b</sup>
$k_s$ /Nm <sup>-1</sup>	8.9	5.0	7.3	10.8
$\nu_s$ /cm <sup>-1</sup>	105	79	98	143
$\Delta E$ /kJmol <sup>-1</sup>	7.2	5.0	4.9	8.0
$\nu_{harm.}$ /cm <sup>-1</sup>	177	177	198	166

<sup>a</sup> Calculated using the experimental results from Ref. 13.

<sup>b</sup> Calculated using the experimental results from Ref. 44.

The ratio of the values of  $k_s$  for *syn*- and *anti*-PO-H<sub>2</sub>O is ~1.8 and ~2.0 for *syn*- and *anti*-PO-D<sub>2</sub>O respectively, indicating that the O··H-O intermolecular H-bond is weaker for the *anti*-configuration than for the *syn*-one. This agrees qualitatively with the fact that higher intensities were observed for all isotopomers of *syn*-PO-H<sub>2</sub>O than for the corresponding *anti*-PO-H<sub>2</sub>O isotopomers.

The order of stability for the three complexes is *syn*-PO-H<sub>2</sub>O > *anti*-PO-H<sub>2</sub>O ≥ EO-H<sub>2</sub>O, according to the experimentally estimated binding energies ( $\Delta E$ s). The relationship between the experimentally observed intensities of different conformers in a molecular beam environment, their relative stabilities, and the inter-conversion barriers between them were discussed in details by Godfrey *et al.* for glycolic acid<sup>51</sup> and histamine.<sup>52</sup> They found that the thermal equilibrium of the conformers prior to jet

expansion was preserved if the inter-conversion barriers were high enough. In cases of much less strongly bound rare gas van der Waals clusters, dramatic isotopic enrichments were reported.<sup>37</sup> For example, transitions of  $^{22}\text{Ne}_2\text{Ar}$  (0.64% abundance) were found to be stronger than those of  $^{20}\text{Ne}^{22}\text{NeAr}$  (16% abundance). For the systems with such low binding energies, the repeated dissociation and reformation in the molecular expansion process leads to an equilibrium distribution in which the heavier species with lower zero-point energy are greatly enriched at the low temperature achieved in the expansion. It is expected that the dissociation and recombination effects are small for the much more strongly bound H-bonded PO–H<sub>2</sub>O. At the pre-expansion temperature of 298 K, an abundance ratio of ~2.4:1 is calculated for *syn*- vs. *anti*-PO–H<sub>2</sub>O from the experimentally estimated energy difference of 2.2 kJ/mol. At the very low temperature of 1 K in the molecular expansion environment, there would be only a negligible amount of *anti*-PO–H<sub>2</sub>O if there were significant collisional relaxation. The detection of both conformers with comparable intensities suggests that the inter-conversion barrier between these two conformers is high enough to minimize the effect of collisional relaxation. A possible transition state, connecting these two conformers where the water molecule lies in the ring plane, was identified in the *ab initio* calculation. It is a first order saddle point with one imaginary frequency of  $-193\text{ cm}^{-1}$ , corresponding to the out of plane wagging motion of the water moiety. The  $\text{O}_{\text{epoxy}}\cdots\text{H}$  H-bonding length was calculated to be 2.252 Å and the raw binding energy for this transition state is  $-19.88\text{ kJ/mol}$ , at the MP2/6-311++G(d,p) level. The barrier height was estimated to be  $\sim 800\text{ cm}^{-1}$ . One would therefore expect the abundance ratio at the pre-expansion temperature to be approximately preserved in the beam

environment. This is roughly consistent with the experimentally observed intensity ratio of about 1.8:1.

The intensity ratio for the D- and H-bonded isomers in the HOD containing PO–water complex is further examined. In the H-bonding molecule–water complexes, the D-bonded species is often substantially enriched in the jet expansion because of its lower zero-point energy and the collisional relaxation through the tunnelling motion that interchanges the D and H atoms of water. For example, only the D-bonded isomer was detected in 1,4-dioxane–DOH,<sup>17</sup> and a 3:1 ratio in favour of EO–DOH over EO–HOD was reported.<sup>13</sup> The differences in zero-point energies between H- and D-bonded species are -0.88 kJ/mol and -0.86 kJ/mol for *syn*- and *anti*-PO–water, respectively, almost the same as for EO–H<sub>2</sub>O. This means an abundance ratio of ~1.4:1 for the D-bonded species over H-bonded species at the pre-expansion temperature of 298 K, for *syn*-PO–water, *anti*-PO–water and EO–water. The experimental intensity ratio for PO–DOH over PO–HOD is about 1.5:1, indicating that very little collisional relaxation through the hydrogen tunnelling motion occurs for PO–water in the jet expansion. The presence of a relatively high barrier is further supported by the fact that no tunnelling splitting due to H<sub>2</sub>O was detected experimentally for PO–H<sub>2</sub>O. Additionally, the observed intensity ratios suggest that the tunnelling barrier is higher for PO–water than that of EO–water.

The above discussions indicate that the intermolecular H-bond in *syn*-PO–H<sub>2</sub>O is stronger and the monomer subunits are more rigidly locked in their positions than in EO–H<sub>2</sub>O. The differences between *anti*-PO–H<sub>2</sub>O and EO–H<sub>2</sub>O, on the other hand, are less prominent. This observation is attributed to the additional stabilizing effect of the

methyl group to the H-bond. The roles of the weak secondary H-bonds (the  $\text{H}_2\text{O}\cdots\text{H}-\text{C}$  noncovalent interactions) in these complexes are examined. In the *syn*-configuration, the intermolecular distance of  $\text{H}_2\text{O}\cdots\text{H}-\text{CH}_2$  is 2.71 Å, considerably shorter than 3.06 Å for  $\text{H}_2\text{O}\cdots\text{H}-\text{CH}$ . The intermolecular separations of  $\text{H}_2\text{O}\cdots\text{H}-\text{C}$  and  $\text{H}_2\text{O}\cdots\text{H}-\text{CH}$  in the *anti*-configuration are 2.95 Å and 2.97 Å, respectively. The above observed trend was also supported by the MP2/6-311++G(d,p) calculations. These weak secondary H-bonds can be classified as *improper-blue shifted* H-bonds and were investigated systematically by Hobza and co-workers.<sup>53</sup> One character of this type of H-bond is a decrease in the C–H bonding length when the C–H bond gets involved in the H-bond. This is manifested in the *syn*-PO–H<sub>2</sub>O species where the bonded and the non-bonded C–H bonding lengths from the MP2/6-311++G(d,p) calculations in  $\text{H}_2\text{O}\cdots\text{H}-\text{CH}_2$  are 1.092 Å and 1.094 Å, respectively, and are in good agreement with the average shortening of 0.002 Å as reported in those studies.<sup>53</sup>

## 2) PO–(H<sub>2</sub>O)<sub>2</sub>

The experimental line intensities of different conformers have been used to establish conformational stability ordering for monomers<sup>54</sup> and for complexes.<sup>55</sup> While the error bars in the intensity measurements here are relatively large, several studies indicate that cluster formation in such a jet expansion is still largely thermodynamically controlled and that the line intensities reflect the stability ordering of the set of conformers. To establish the conformational stability ordering from the experiments, the observed line intensities of the same *a*-type rotational transitions of different conformers were compared since the *a*-dipole moment components were



predicted and experimentally confirmed to be very similar for the two conformers detected. Experimentally, the line intensities of *anti*-PO-(H<sub>2</sub>O)<sub>2</sub> are about twice as strong as *syn*-PO-(H<sub>2</sub>O)<sub>2</sub>. This is very interesting since the diastereofacial discrimination favors *syn*-configuration in the binary PO-H<sub>2</sub>O complex. The addition of the second water molecule must have played a significant role in the diastereofacial discrimination process since the sign of diastereofacial discrimination energy is now reversed! One plausible explanation is that as the number of water molecules grows, the secondary H-bonding contribution from the methyl group to the O atom of water becomes less significant, which is the deciding factor for the stabilization in PO-H<sub>2</sub>O. The main factors in the action of the molecular system are to maximize the interactions between the second water molecule and the PO, as well as between water molecules. On the other hand, experimental results with the PO-water binary and ternary complexes shows that the MP2 calculations failed to capture the energy differences between the conformers. Therefore, future high resolution spectroscopic work has to be carried out to establish the conformational stability ordering in the PO-(water)<sub>3</sub> cluster. The good signal-to-noise ratio achieved for the transitions of the PO-(water)<sub>1,2</sub> clusters, as well as the favorable rotational constants and dipole moments predicted for these larger clusters, suggests that this is feasible.

## 5.6 Concluding remarks

The PO-water complex was investigated using rotational spectroscopy and *ab initio* methods for the first time. Two structural conformers (*syn*-PO-H<sub>2</sub>O and *anti*-PO-H<sub>2</sub>O) were detected experimentally. The conformational stability and the H-

bonding strength of the PO–H<sub>2</sub>O conformers were established using the experimental spectroscopic constants based on a pseudo-diatomic model and were further discussed using the derived structures. The barrier to inter-conversion between the two distinct structural minima was evaluated with *ab initio* calculations and discussed in terms of the observed intensities of the two conformers. A stabilizing contribution of the methyl group to the intermolecular H-bond was demonstrated with the experimental observations. Two hydrogen-bonded 1:2 PO–water conformers (*syn*-PO–(H<sub>2</sub>O)<sub>2</sub> and *anti*-PO–(H<sub>2</sub>O)<sub>2</sub>) were also measured and analyzed. The geometries and stability ordering were established for the two most stable conformers. In particular, the experimental observation shows that the *anti*-PO–(H<sub>2</sub>O)<sub>2</sub> conformer is favoured over the *syn*-PO–(H<sub>2</sub>O)<sub>2</sub>, opposite of what was observed for the PO–H<sub>2</sub>O complex, but in accord with what was predicted for PO in bulk water. This result clearly demonstrates how the stabilities of conformers can alter during the initial steps of hydration. The current study is a step further in bridging the gap of our knowledge from the isolated binary PO–H<sub>2</sub>O system to PO in bulk water. The trend observed from one to two water molecules is in accord with the theoretical prediction that the *anti*-configuration is preferred for PO in aqueous solution.<sup>22</sup> It would be of great interest to follow the solvation process by sequentially solvating PO with more water molecules and conclusively establishing the trend. *Ab initio* calculations of PO solvated with three and four water molecules indicate the feasibility of following the solvation process experimentally. The present report demonstrates the great potential of high resolution spectroscopy in combination with quantum chemistry calculations for exploring the underlying mechanism of solvation of chiral organic molecules in aqueous solution.

## References

---

1. Jeffrey, J. A.; Saenger, W. *Hydrogen Bonding in Biological Structures*, Springer-Verlag: Berlin, **1991**.
2. Desiraju, G. R. *The Weak Hydrogen Bond in Structural Chemistry and Biology*, edited by Steiner, T.; Oxford University Press Inc: New York, **1999**.
3. Scheiner, S. *Hydrogen Bonding*, Oxford University Press: New York, **1999**.
4. Sarma, J. A. R. P.; Desiraju, G. R. *J. Chem. Soc. Perkin Trans.* **1987**, 2, 1195.
5. Desiraju, G. R.; Murty, B. N. *Chem. Phys. Lett.* **1987**, 139, 360.
6. Derewenda, Z. S.; Lee, L.; Derewenda, U. *J. Mol. Biol.* **1995**, 252, 248.
7. Wahl, M.; Sundaralingam, M. *Trends Biochem. Sci.* **1997**, 22, 97.
8. Steiner, T. *Acta Crystallogr., Sect. D* **1995**, 51, 93.
9. Lindström, U. M. *Chem. Rev.* **2002**, 102, 2751.
10. Gutowsky, H. S.; Emilsson, T.; Arunan, E. *J. Chem. Phys.* **1993**, 99, 4883.
11. Gerhards, M.; Schmitt, M.; Kleinermanns, K.; Stahl, W. *J. Chem. Phys.* **1996**, 104, 967.
12. Melandri, S.; Maris, A.; Favero, P. G.; Caminati, W. *Chem. Phys.* **2002**, 283, 185.
13. Caminati, W.; Moreschini, P.; Rossi, I.; Favero, P. G. *J. Am. Chem. Soc.* **1998**, 120, 11144.
14. Paolo, O.; Giuliano, M.; Velino, B.; Caminati, W. *Chem. Eur. J.* **2004**, 10, 538.
15. Sanz, M. E.; López, J. C.; Alonso, J. L.; Maris, A.; Favero, P. G.; Caminati, W. *J. Phys. Chem. A* **1999**, 103, 5285.
16. Li, Q.; Wu, G.; Yu, Z. *J. Am. Chem. Soc.* **2006**, 128, 1438.
17. Caminati, W.; Dell'Erba, A.; Melandri, S.; Favero, P. G. *J. Am. Chem. Soc.* **1998**, 120, 5555.
18. Spoerel, U.; Stahl, W.; Caminati, W.; Favero, P. G. *Chem. Eur. J.* **1998**, 4, 1974.
19. Losada, M.; Xu, Y. *Phys. Chem. Chem. Phys.* **2007**, 9, 3127.

- 
20. Müller, T.; Wiberg, K. B.; Vaccaro, P. H. *J. Phys. Chem. A* **2000**, *104*, 5959.
21. Wilson, S. M.; Wiberg, K. B.; Cheeseman, J. R.; Frisch, M. J.; Vaccaro, P. H. *J. Phys. Chem. A* **2005**, *109*, 11752.
22. Mukhopadhyay, P.; Zuber, G.; Goldsmith, M-R.; Wipf, P.; Beratan, D. N. *ChemPhysChem* **2006**, *7*, 2483.
23. Frisch, M. J. *et al.* GAUSSIAN03 (Revision B.01): see Chapter 4 References.
24. Binkley, J. S.; Pople, J. A. *Int. J. Quantum Chem.* **1975**, *9*, 229.
25. Krishnan, R.; Binkley, J. S.; Seeger, R.; Pople, J. A. *J. Chem. Phys.* **1980**, *72*, 650.
26. Dunning, T. H. Jr. *J. Chem. Phys.* **1989**, *90*, 1007.
27. Woon, D. E.; Dunning, T. H. Jr. *J. Chem. Phys.* **1993**, *98*, 1358.
28. Stone, A. J. *The Theory of Intermolecular Forces*, Clarendon Press: Oxford, **1996**, p.39.
29. Boys, S. F.; Bernardi, F. *Mol. Phys.* **1970**, *10*, 553.
30. Kim, K. S; Tarakeshwar, P.; Lee, J. Y. *Chem. Rev.* **2000**, *100*, 4145.
31. Zwart, E.; Ter Meulen, J. J.; Meerts, W. L. *Chem. Phys. Lett.* **1990**, *166*, 580.
32. Priem, D.; Ha, T.-K.; Bauder, A. *J. Chem. Phys.* **2000**, *113*, 169.
33. Qin, W.; Jäger, W. *J. Phys. Chem. A* **2007**, *111*, 2093.
34. Peterson, I.; Suenram, R. D.; Lovas, F. J. *J. Chem. Phys.* **1991**, *94*, 106.
35. Kisiel, Z.; Pietrewicz, B. A.; Desyantnyk, O.; Pszczolkowski, L.; Struniewicz, C.; Sadlej, J. *J. Chem. Phys.* **2003**, *119*, 5907.
36. Blanco, S.; López, J. C.; Lesarri, A.; Alonso, J. L. *J. Am. Chem. Soc.* **2006**, *128*, 12111.
37. Xu, Y.; Jäger, W. *J. Chem. Phys.* **1997**, *106*, 7968.
38. Dijkerman, H. A.; Ruitenberg, G. *Chem. Phys. Lett.* **1969**, *3*, 172.
39. Hartwig, H.; Dreizler, H. *Z. Naturforsch A* **1996**, *51*, 923.

- 
40. Watson, J. K. G. *Vibrational Spectra and Structure: A Series of Advances*, edited by Durig, J.R.; Elsevier: New York, **1977**, Vol. 6, pp. 1-89.
41. Swalen, J. D.; Herschbach, D. R. *J. Chem. Phys.* **1957**, 27, 100.
42. Herschbach, D. R.; Swalen, J. D. *J. Chem. Phys.* **1958**, 29, 761.
43. Imachi, M.; Kuczkowski, R. L. *J. Mol. Struct.* **1982**, 96, 55.
44. Dyke, T. R.; Mack, K. M.; Muentner, J. S. *J. Chem. Phys.* **1977**, 66, 498.
45. Liu, K.; Loeser, J. G.; Elrod, M. J.; Host, B. C.; Rzepiela, J. A.; Pugliano, N.; Saykally, R. J. *J. Am. Chem. Soc.* **1994**, 116, 3507.
46. Cruzan, J. D.; Viant, M. R.; Brown, M. G.; Saykally, R. J. *J. Phys. Chem. A* **1997**, 101, 9022.
47. Cook, R. L.; De Lucia, F. C.; Helminger, P. *J. Mol. Spectrosc.* **1974**, 53, 62.
48. Gordy, W.; Cook, R. L. *Microwave Molecular Spectra*, Wiley: New York, **1984**, Chap. XIII.
49. Read, W. G.; Campbell, E. J.; Henderson, G. *J. Chem. Phys.* **1983**, 78, 3501.
50. Bettens, R. P. A.; Spycher, R. M.; Bauder, A. *Mol. Phys.* **1995**, 86, 487.
51. Godfrey, P. D.; Rodgers, F. M.; Brown, R. D. *J. Am. Chem. Soc.* **1997**, 119, 2232.
52. Godfred, P. D.; Brown, R. D. *J. Am. Chem. Soc.* **1998**, 120, 10724.
53. Hobza, P.; Havlas, Z. *Chem. Rev.* **2000**, 100, 4253.
54. Maris, A. *Phys. Chem. Chem. Phys.* **2004**, 6, 2611.
55. Borho, N.; Xu, Y. *Angew. Chem. Int. Ed.* **2006**, 46, 2276.

\*\*\*\*\*

## CHAPTER 6

# INVESTIGATION OF PO DIMERS: *AB INITIO* CALCULATIONS AND ROTATIONAL SPECTRA

\*\*\*\*\*

### 6.1 Introduction

For chemists, the *R/S* system is IUPAC (International Union of Pure and Applied Chemistry) organic nomenclature for denoting enantiomers of a chiral system.<sup>1</sup> Each stereogenic center is labeled *R* or *S* according to the rank of the four groups (1, 2, 3, 4) attached to the stereogenic center based on atomic number. If the center is oriented so that the lowest priority group 4 is pointed away from a viewer, the viewer will then see two possibilities: if the priority of the remaining three substituents decreases (1 to 2 to 3) in clockwise direction, it is labeled *R* (for *Rectus*), if it decreases in counterclockwise direction, it is *S* (for *Sinister*). Chiral recognition is the ability of a chiral molecule (*R/S*) to distinguish between the two enantiomeric forms (*R'* and *S'*) of another chiral molecule.<sup>2</sup> One important question is how the intermolecular forces act in a concerted way to enable the substantial enantioselectivity in many natural processes. Enantiomeric discrimination is also the basis of chiral chromatography,<sup>3</sup> asymmetric synthesis, and NMR analysis of enantiomeric purity.<sup>4</sup> Although these techniques are evidently consequence of enantioselectivity based on different interaction energies of the *RR* and *RS*

diastereomeric pairs,<sup>5</sup> there is very little quantitative experimental information on the nature of these interactions and their contributions to chiral discrimination on the molecular level. Very recently, Soloshonok reported that nonracemic mixtures of chiral molecules containing perfluoromethyl groups exhibit remarkable amplification of the self-disproportionation,<sup>6</sup> and that putting such mixtures through an achiral-Si gel column can produce an *ee* (enantiomeric excess) as high as 99% depending on the effluents used. This underscores the importance in understanding the interactions among chiral molecules and between chiral molecules and solvent molecules.

It is possible to probe such recognition mechanism on the molecular level in a microscopic model system. Spectroscopic studies of chiral molecular complexes formed in a supersonic expansion were first reported by the groups of Zehnacker and Giardini-Guidoni in an effort to provide quantitative evidence of enantiomeric selection.<sup>7, 8, 9, 10</sup> These groups have studied complexes composed of a chiral aromatic derivative and a chiral alcohol using laser-induced fluorescence,<sup>7</sup> hole-burning,<sup>8</sup> and resonance enhanced multiphoton ionization spectroscopy.<sup>9, 10</sup> More recently, Suhm and co-workers used ragout-jet Fourier transform (FT) infrared (IR) spectroscopy to probe vibrational band structures of a number of chiral and transient chiral molecular complexes, such as glycidol dimer,<sup>11, 12</sup> binary, ternary,<sup>13</sup> and even larger aggregates of lactates,<sup>14</sup> ethanol dimer,<sup>15</sup> and fluoroethanol dimer.<sup>16</sup> The first high resolution spectroscopic study of a chiral molecular complex, butan-2-ol dimer,<sup>17</sup> was reported by Howard and co-workers, where one heterochiral dimer was assigned. Subsequently, the same group published a rotational study of ethanol dimer, focusing on the transient chirality of the molecular system.<sup>18</sup> High resolution spectroscopy is sensitive to even

the subtlest differences in the structures. Rotationally resolved spectra can be used to obtain accurate structural information of different conformers that is difficult to extract from the low resolution electronic or FTIR measurements mentioned above. Almost parallel to the time period of accomplishing the work for this chapter, rotational spectra of all six possible hydrogen-bonded PO–ethanol (EtOH) conformers were detected and analyzed.<sup>19</sup> This case study shows that the chiral discriminating forces at play are the concerted effect of secondary hydrogen bonding interactions and steric hindrance, leading to a preference of the *syn*-conformation and the heterochiral combination. This observation is unlike in the classic lock-and-key picture in which steric hindrance is a major player. It is also one of the first few reports that demonstrate the great potential of high resolution FTMW spectroscopy for exploring the underlying mechanism of molecular recognition on the microscopic level.

The very limited high resolution spectroscopic data of chiral molecular complexes highlight the fact that achieving unambiguous assignments of rotationally resolved spectra of large molecular systems with many potential conformers is a daunting task. To aid the spectroscopic studies, a small number of high level quantum chemistry studies have been dedicated to the investigations of chiral discrimination effects of suitable small chiral molecules. Portmann *et al.* investigated chiral recognition in the complexes of PO–HOOH and its derivatives.<sup>20</sup> Detailed studies on the hydrogen (H)-bonded molecular complex between propylene imine and HOOH have been carried out during my PhD work. Alkorta and Elguero studied a series of  $\beta$ -aminoalcohols and H-bonded complexes consisting of compounds with axial chirality.<sup>21, 22</sup>



In this chapter, the detailed rotational spectroscopic and high level *ab initio* studies of chiral self-recognition in PO dimer in the gas phase will be reported. As discussed in the previous chapter, the secondary H-bonding may have subtle yet decisive contribution to the stability ordering of the conformers. In the following sections, the first high resolution spectroscopic assignments of six homo- and heterochiral conformers of PO dimer will be described. Attention will be focused on the weak secondary H-bonds (the  $O_{\text{epoxy}} \cdots \text{H}-\text{C}$  noncovalent interactions) and their roles in the chiral self-discrimination process in PO dimer.

## **6.2 *Ab initio* calculations**

### **6.2.1 Construction of binary conformers**

Even for a simple chiral molecular system such as PO, the number of possible binary conformers is surprisingly large. By restraining the consideration only to the  $O_{\text{epoxy}} \cdots \text{H}-\text{C}$  noncovalent interaction as the main binding motivation, the number can be largely reduced. Even with these restrictions, on the basis of chemical intuition, more than twenty preliminary structures were proposed originally. These structures can be divided into two groups, differing in the number of the secondary H-bonds utilized in each conformer. The first group emphasizes that each PO monomer simultaneously accepts two protons from and donates two protons to the other monomer. The two PO subunits are connected through those four secondary H-bonds, forming two six- or five-membered intermolecular H-bonded rings. Statistically, this group consists of six homochiral and six heterochiral conformers considering each C atom out of the three C's of one PO can contribute one H atom every time. In the

second group each monomer can only act as either proton acceptor or donor, that is only two intermolecular H-bonds are formed in each conformer. A symbolic sketch of the two groups is given in Figure 6-1. As the number of H-bonds in the second group is only half of that in the first group, it is expected that the first group conformer have stronger binding.



**Figure 6-1** Schematic view of PO binary conformers. Left: each PO monomer simultaneously accepts two protons from and donates two protons to the other monomer, resulting four secondary H-bonds in total to connect the two subunits. Right: each monomer can only act as either proton acceptor or donor, i.e. only two intermolecular H-bonds are formed in each conformer.

### 6.2.2 Geometry optimizations

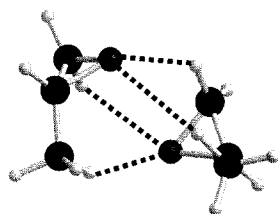
To provide valuable clues for the spectroscopic study, a series of geometry optimizations for the possible homo- and heterochiral dimers were carried out using the GAUSSIAN03 software package.<sup>23</sup> Second-order Møller-Plesset perturbation theory (MP2)<sup>24</sup> with the basis set 6-311++G(d,p)<sup>25</sup> was employed for full geometry optimizations. As the estimation, the conformers in the second group were calculated to have about half of the dissociation energies compared to those of the first group, and are, thus, being excluded from experimental searches. The twelve proposed structures of the first group were all found to be local minima. The raw and counterpoise corrected<sup>26</sup> dissociation energies, rotational constants, and electric dipole

moment components for the above twelve optimized structures calculated with MP2/6-311++G(d,p) are summarized in Table 6-1. The Cartesian coordinates of the twelve structural conformers of PO dimer are listed in Table A2-3 in Appendix 2. It was noticed that the differences in the rotational constants of some of these conformers are very small. Therefore, to be certain about the proposed configurations, additional geometry optimization calculations were also carried out using three more basis sets: 6-311++G(2d, 2p), aug-cc-pVDZ<sup>27</sup> and a mixed basis set, i.e. aug-cc-pVDZ for the heavy atoms C and O, and 6-311+G(d,p) for the H atoms, respectively. The dissociation energies, rotational constants, and electric dipole moments for the twelve optimized structures calculated with the three additional basis sets are shown in Table 6-2. In general, the values predicted by all four basis sets agree with each other, confirming the distinct identity of each configuration. For the few conformers with similar rotational constants, their dipole moment components differ enough to possess distinguishable spectral pattern. For simplicity, the result from MP2/6-311++G(d,p) will be referred in the remainder of this chapter and reference to the results by the other three basis sets will be made only when needed.

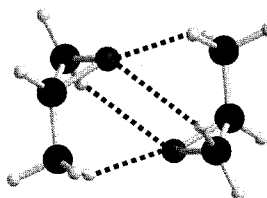
### 6.2.3 Nomenclature

The MP2/6-311++G(d,p) optimized structures of the twelve conformers of PO dimer are shown in Figure 6-2. Considering the complexity of this molecular system, it is necessary and important to differentiate each structure clearly. I proposed a unique notation for the conformational structures under consideration. It is of the form H<sub>x</sub>H<sub>y</sub>R-H<sub>x'</sub>H<sub>y'</sub>R/S where *R* or *S* specify the chirality of the monomer subunit. The

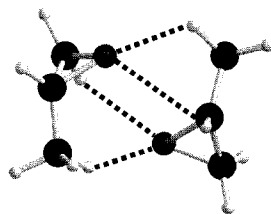
*RR* or *SS* combination indicates homochiral dimer, while the *RS* or *SR* label means heterochiral dimer. Since the *SS* and *RR* of a particular configuration give the same rotational spectrum and the same is true for the *RS* and *SR* pair, *R* notation is always used for the first subunit for simplicity. The letters *x*, *y* and *x'*, *y'* take the integer values of 1, 2 or 3, indicating that the corresponding hydrogen atoms which contribute to the H-bonds are from the CH, CH<sub>2</sub> or CH<sub>3</sub> sites, respectively. For easy bookkeeping, the integers are kept in descending order in each monomer subunit.



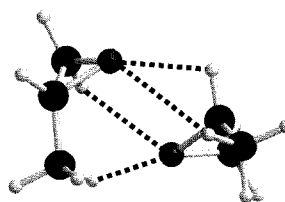
H3H2R-H3H2R (*RR*1)



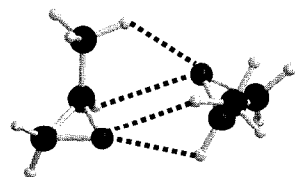
H3H2R-H3H2S (*RS*1)



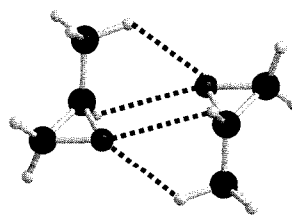
H3H2R-H3H1R (*RR*2)



H3H2R-H3H1S (*RS*2)



H3H1R-H3H1R (*RR*3)



H3H1R-H3H1S (*RS*3)

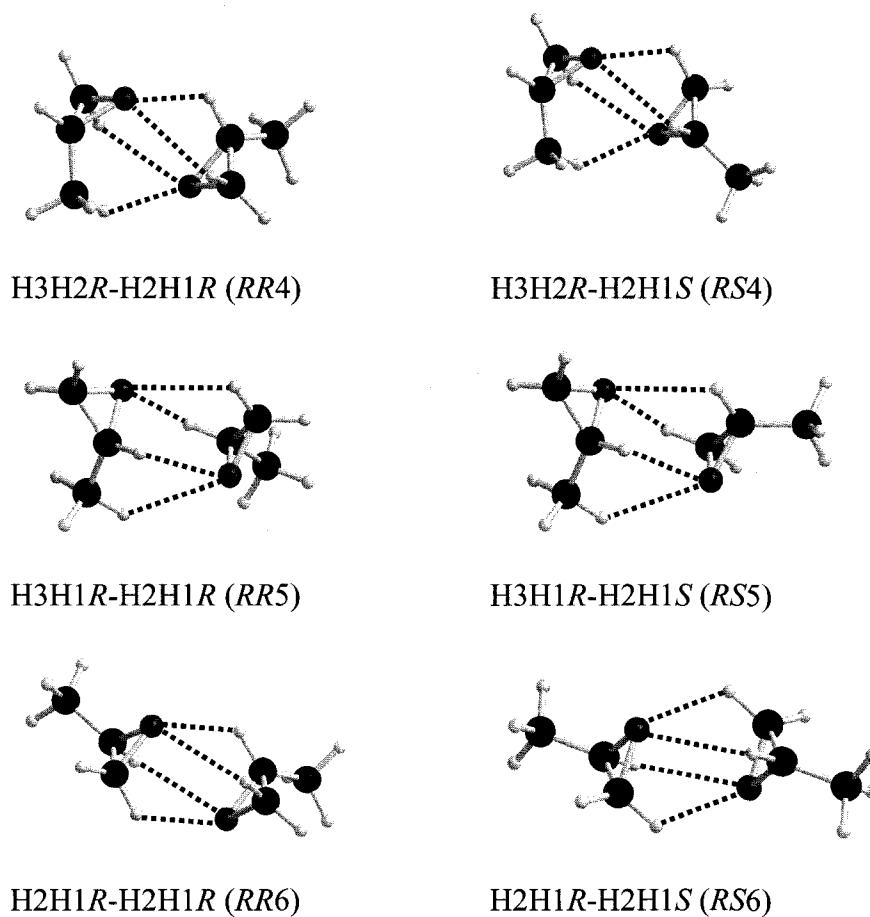


**Figure 6-2** Optimized geometries at the MP2/6-311++G(d,p) level of theory of six homochiral (*RR*) and six heterochiral (*RS*) conformers of PO dimer. The corresponding notation for each conformer takes the form of H<sub>x</sub>H<sub>y</sub>*R*-H<sub>x'</sub>H<sub>y'</sub>*R/S* where *R* or *S* specifies the chirality of the monomer subunit. The letters *x*, *y* and *x'*, *y'* indicates that the corresponding hydrogen atoms are from the CH, CH<sub>2</sub> or CH<sub>3</sub> sites, respectively. For additional details, refer to the text.

Thus in the nomenclature described here, H3H2*R*-H2H1*S* represents a heterochiral dimer with four intermolecular H-bonds where CH<sub>3</sub> and CH<sub>2</sub> of *R*-PO each contributes one H atom to the O atom of *S*-PO, and the other two H atoms from CH<sub>2</sub> and CH of *S*-PO point towards the O atom of *R*-PO. The notation introduced here provides important information about the binding sites in each conformer and is given

in Figure 6-2 for all twelve configurations. These notations will be used in later discussions of stability order and chiral self-recognition where specific binding sites are relevant. To make the text more concise, further simplification is made as labeling the six homochiral conformers as *RR1* to *RR6* and the corresponding heterochiral conformers as *RS1* to *RS6* (see Figure 6-2).

**Table 6-1** Calculated raw and counterpoise corrected dissociation energies (in kJ/mol), rotational constants (in MHz), and electric dipole moment components (in Debye) of the homochiral and heterochiral conformers of PO dimer at the MP2/6-311++G(d,p) level of theory.

	$D_e$	$D_e+CP$	$A$	$B$	$C$	$ \mu_a $	$ \mu_b $	$ \mu_c $
<i>RR1</i>	-23.55	-15.31	3013	1131	1007	0.01	0.04	0.00
<i>RS1</i>	-22.95	-14.98	3168	1116	939	0.01	0.00	0.01
<i>RR2</i>	-22.98	-14.97	3171	1111	932	0.52	0.54	0.03
<i>RS2</i>	-22.92	-14.91	3179	1048	1013	0.58	0.35	0.23
<i>RR3</i>	-22.42	-14.36	3363	1020	958	0.00	0.00	0.59
<i>RS3</i>	-21.97	-14.05	3290	1095	887	0.00	0.00	0.00
<i>RR4</i>	-22.84	-14.79	3838	970	874	0.18	0.26	0.06
<i>RS4</i>	-23.21	-14.92	3454	1025	904	0.23	0.22	0.18
<i>RR5</i>	-22.34	-14.22	3707	967	893	0.78	0.20	0.42
<i>RS5</i>	-22.15	-14.22	3833	948	857	0.67	0.77	0.03
<i>RR6</i>	-22.60	-14.46	3934	912	821	0.00	0.43	0.00
<i>RS6</i>	-22.55	-14.44	4866	851	801	0.00	0.00	0.00

**Table 6-2** Calculated raw and counterpoise corrected dissociation energies (in kJ/mol), rotational constants (in MHz), and electric dipole moment components (in Debye) of the homochiral and heterochiral conformers of PO dimer at the MP2 level of theory with the 6-311++G(2d,2p) and aug-cc-pVDZ basis sets and a mix basis set, aug-cc-pVDZ/6-311++G(d,p).

	$D_e$	$A$	$B$	$C$	$ \mu_a $	$ \mu_b $	$ \mu_c $
6-311++G(2d,2p)							
<i>RR1</i>	-24.24	3011	1158	1029	0.00	0.01	0.00
<i>RS1</i>	-23.77	3146	1148	961	0.00	0.00	0.00
<i>RR2</i>	-24.05	3160	1131	950	0.51	0.63	0.07
<i>RS2</i>	-24.07	3185	1060	1030	0.63	0.37	0.22
<i>RR3</i>	-23.37	3402	1029	966	0.00	0.00	0.52
<i>RS3</i>	-22.83	3314	1100	895	0.00	0.00	0.00
<i>RR4</i>	-23.92	3810	993	892	0.16	0.24	0.05
<i>RS4</i>	-24.07	3476	1039	920	0.20	0.21	0.17
<i>RR5</i>	-23.46	3713	977	906	0.83	0.22	0.42
<i>RS5</i>	-23.33	3836	963	868	0.70	0.76	0.04
<i>RR6</i>	-23.69	3956	924	835	0.00	0.37	0.00
<i>RS6</i>	-23.69	4910	861	814	0.00	0.00	0.00
aug-cc-pVDZ							
<i>RR1</i>	-28.57	2966	1167	1037	0.00	0.01	0.00
<i>RS1</i>	-28.19	3109	1144	957	0.00	0.00	0.00
<i>RR2</i>	-28.25	3098	1140	952	0.48	0.62	0.10
<i>RS2</i>	-28.24	3142	1067	1034	0.62	0.31	0.22
<i>RR3</i>	-27.82	3377	1032	978	0.00	0.00	0.53
<i>RS3</i>	-27.22	3275	1111	904	0.00	0.00	0.00
<i>RR4</i>	-27.63	3761	992	891	0.16	0.26	0.04
<i>RS4</i>	-27.99	3374	1052	929	0.21	0.20	0.18
<i>RR5</i>	-27.25	3639	986	914	0.81	0.15	0.41
<i>RS5</i>	-26.98	3721	975	873	0.66	0.79	0.10
<i>RR6</i>	-27.22	3841	937	841	0.00	0.41	0.00
<i>RS6</i>	-27.11	4790	864	815	0.00	0.00	0.00

**Table 6-2** (Continued)

	$D_e$	$A$	$B$	$C$	$ \mu_a $	$ \mu_b $	$ \mu_c $
	aug-cc-pVDZ/6-311++G(d,p) <sup>a</sup>						
<i>RR1</i>	-24.79	2972	1145	1017	0.00	0.02	0.00
<i>RS1</i>	-24.31	3113	1131	948	0.00	0.00	0.00
<i>RR2</i>	-24.91	3111	1130	945	0.45	0.60	0.09
<i>RS2</i>	-24.85	3139	1058	1024	0.57	0.35	0.20
<i>RR3</i>	-24.91	3356	1029	974	0.00	0.00	0.51
<i>RS3</i>	-24.40	3259	1107	899	0.00	0.00	0.00
<i>RR4</i>	-24.63	3768	983	883	0.19	0.24	0.06
<i>RS4</i>	-24.91	3402	1041	919	0.23	0.22	0.18
<i>RR5</i>	-24.72	3652	979	905	0.79	0.17	0.40
<i>RS5</i>	-24.39	3758	966	868	0.65	0.75	0.05
<i>RR6</i>	-24.76	3871	928	835	0.00	0.36	0.00
<i>RS6</i>	-24.69	4829	862	813	0.00	0.00	0.00

<sup>a</sup> The basis set aug-cc-pVDZ for the heavy atoms C and O, and 6-311+G(d,p) for the H atoms.

### 6.3 Spectral search and assignment

The pulsed molecular beam FTMW spectrometer,<sup>28</sup> described in Chapter 3, was used in this study. For the investigations of the homochiral species, a gas mixture of less than 1.0 % enantiomeric *R*-PO ( $\geq 99.0\%$ , Aldrich) in 6.5 bar of helium (Praxair) at room temperature was expanded through a General Valve (Series 9, 0.8mm). A racemic mixture of PO (99+%, Aldrich) was used for the spectral searches and measurements of the heterochiral dimers and for the intensity investigation of all homo- and heterochiral diastereomers. The full linewidth at half height of a well resolved line is about 18 kHz and the uncertainty of the frequency measurements is  $\sim 2$  kHz. The estimated effective rotational temperature in the helium expansion is 2.5 K.



In the previous jet-cooled rotational spectroscopic studies of van der Waals complexes, for example dimethyl ether dimer,<sup>29</sup> only the lowest energy conformer was detected. However, the spectral search for *RR1*, which was predicted to be the most stable conformer of all, could be difficult here due to its small electric dipole moments as predicted by *ab initio* calculations. On the other hand, the FTMW spectroscopy was successfully utilized for the studies of mixed rare gas clusters whose dipole moments were estimated to be in the same order of magnitude or smaller than that of *RR1* conformer.<sup>30</sup> Therefore, initially the spectral scan was carried out in the 4-7 GHz range for the low *J* transitions of *RR1* conformer. A very rich spectrum was obtained. To determine the identity of the line carriers, test measurements were conducted by replacing helium carrier gas with neon and enantiopure PO with racemic PO. Some lines can be identified as homochiral complexes according to the fact that they are present in both He and Ne carrier gases and have stronger intensity in the enantiopure sample. However, the intensity of each measurement fluctuated dramatically over time. Therefore comparison was not confirmative enough at the beginning.

After a lot of effort, none of the observed lines could be assigned satisfactorily to this lowest energy configuration without dramatic changes in the shape of the conformer. Spectral search was then carried out for other homochiral configurations. It was found that nine previously observed lines could be assigned to the *a*-type transitions of the second lowest energy homochiral configuration, *RR2*. The *b*-type and the much weaker *c*-type transitions were then predicted based on the initial fit, and successfully observed. The *a*- and *b*-type transitions require similar optimized MW excitation pulse width, while the optimized MW pulse widths for the *c*-type transitions

are much longer. This observation is in accord with the ratio of the dipole moment components predicted by the MP2/6-311++G(d,p) calculations. The experimental magnitudes of the dipole moment components, estimated by comparing the optimized pulsed widths to that of OCS with a known dipole moment of 0.7149 D,<sup>31</sup> are also consistent with the prediction. The assignment of the observed lines to this particular conformer is therefore not only verified by the similarity of the observed and calculated rotational constants, but is also further reinforced by the good agreement between the experimentally estimated and theoretically predicted electric dipole moments.

In addition to the *RR2* conformer, seven *a*-type transitions of *RR4* were found. The magnitude of the *a*-dipole moment component is estimated to be about 1.5 times larger than that of *RR2*, in general agreement with the prediction. The searches for the *a*-type transitions of *RR4* were more difficult due to the predicted dipole moments and the corresponding transitions were detected with a significantly longer MW pulse width. That ties in well with the fact that the predicted *a*-dipole moment component is several times smaller than that of *RR2* or *RR5*. In total, ten lines were assigned to the *a*-type transition with *J* up to 5 and *K<sub>a</sub>* up to 2. Searches for the *b*- and *c*-type transitions of *RR4* and *RR5* were attempted, but no concrete assignments have been achieved. Although a few candidates were located for *RR3* and *RR6* in the spectral searches, no satisfactory assignment could be achieved since these two conformers have only *c*- or *b*-type transitions whose patterns are much more difficult to recognize than the *a*-type transitions.

The searches and assignments for the heterochiral PO dimers followed the procedure described above. The three configurations, *RS2*, *RS4*, and *RS5*, predicted to have substantial electric dipole moment values, were identified successfully. The experimentally estimated magnitudes of the *a*-, *b*- and *c*-dipole moments are again in reasonable agreement with the MP2/6-311++G(d,p) predictions. In total, 42 lines were measured for the heterochiral PO dimers: 17 for *RS2*, 11 for *RS4*, and 14 for *RS5*. These transitions are not present using the enantiopure PO sample. The remaining three *RS* conformers have close to zero electric dipole moments and no spectral searches were attempted for them. Figure 6-3 shows all the transitions detected in both the enantiopure and racemic PO samples in a 1 GHz frequency span, plotted with the observed relative intensity ratio. A number of unassigned transitions are also shown. Although experimental evidence indicates that the carriers of these unassigned transitions are most likely due to the binary or larger PO clusters, their exact identities are not yet determined. A complete list of mystery lines in this molecular system is given in Table A1-6 and A1-7 in Appendix 1 for enantiopure and racemic samples, respectively.

The measured rotational transition frequencies of the six PO dimers are summarized in Tables A1-8 and A1-9 in Appendix 1 for homochiral and heterochiral configurations, respectively. They were fitted to a Watson's *S*-reduction semi-rigid rotor Hamiltonian in its *I*<sup>-</sup>representation.<sup>32</sup> The resulting spectroscopic constants are listed in Tables 6-3 and 6-4 for the homo- and heterochiral diastereomers, respectively. The standard deviations of the spectroscopic fits are a few kHz, in good agreement with the experimental uncertainty.

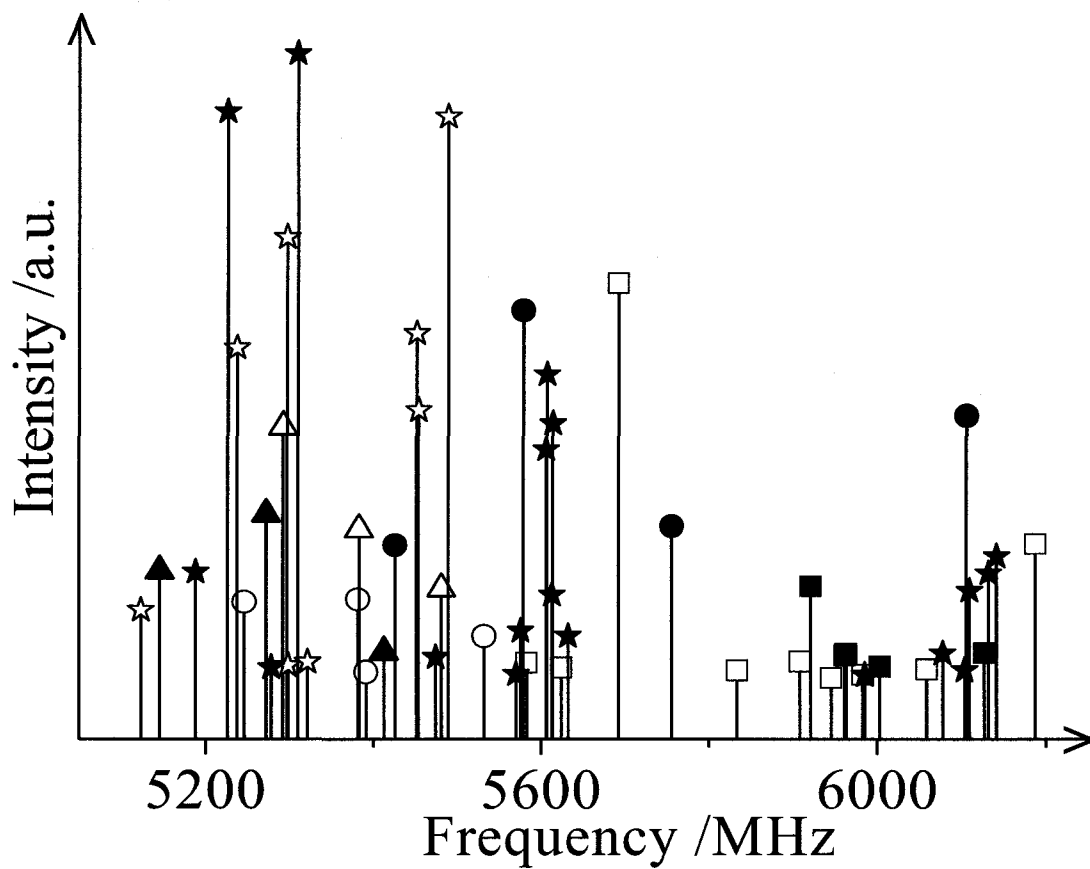


**Figure 6-3** Observed rotational transitions with the enantiomeric *R*-PO and racemic PO samples. The transitions are assigned to *RR*2 (□); *RR*4 (○); *RR*5 (△); *RS*2 (■); *RS*4 (●) and *RS*5 (▲). ☆ represents unassigned lines in enantiopure sample; ★ indicates unassigned lines only in racemic sample but not in enantiopure one.

**Table 6-3** Experimental rotational and centrifugal distortion constants of the three homochiral conformers of PO dimer.

	<i>RR2</i>	<i>RR4</i>	<i>RR5</i>
<i>A</i> /MHz	3157.9758 (6) <sup>a</sup>	3799.5 (4)	3728.3 (3)
<i>B</i> /MHz	1073.4876 (1)	946.0501 (7)	929.3788 (4)
<i>C</i> /MHz	908.3481 (1)	850.8587 (6)	866.3289 (4)
<i>D<sub>J</sub></i> /kHz	0.678 (2)	0.60 (1)	0.577 (6)
<i>D<sub>JK</sub></i> /kHz	3.020 (8)	0.1 (2)	0.6 (3)
<i>D<sub>K</sub></i> /kHz	-2.7 (1)	0.0 <sup>b</sup>	0.0 <sup>b</sup>
<i>d<sub>1</sub></i> /kHz	-0.127 (2)	-0.11 (1)	-0.047 (4)
<i>d<sub>2</sub></i> /kHz	-0.029 (1)	0.0 <sup>b</sup>	0.006 (3)
<i>N</i> <sup>c</sup>	36	7	10
$\sigma$ /kHz <sup>d</sup>	4.9	0.4	1.1

<sup>a</sup> Standard errors in parentheses are expressed in units of the last digits.

<sup>b</sup> Fixed at 0.0 in the fit.

<sup>c</sup> Number of transitions in the fit.

<sup>d</sup> rms deviation of the fit.

**Table 6-4** Experimental rotational and centrifugal distortion constants of the three heterochiral conformers of PO dimer.

	<i>RS2</i>	<i>RS4</i>	<i>RS5</i>
<i>A</i> /MHz	3186.5835 (9) <sup>a</sup>	3473.684 (2)	3808.5 (3)
<i>B</i> /MHz	1007.4002 (2)	987.2129 (6)	924.5426 (3)
<i>C</i> /MHz	980.0498 (2)	877.1365 (5)	835.6008 (4)
<i>D<sub>J</sub></i> /kHz	0.711 (3)	0.697 (9)	0.46 (2)
<i>D<sub>JK</sub></i> /kHz	-0.8(2)	0.4 (1)	0.9 (3)
<i>D<sub>K</sub></i> /kHz	2.33 (3)	7.7 (8)	0.2 (3)
<i>d<sub>1</sub></i> /kHz	-0.047 (2)	-0.05 (2)	-0.051 (4)
<i>d<sub>2</sub></i> /kHz	-0.004 (3)	1.2 (4)	-0.018 (9)
<i>N</i> <sup>b</sup>	17	11	14
$\sigma$ /kHz <sup>c</sup>	3.7	4.4	0.5

<sup>a</sup> Standard errors in parentheses are expressed in units of the last digits.

<sup>b</sup> Number of transitions in the fit.

<sup>c</sup> rms deviation of the fit.

## 6.4 Discussions

### 6.4.1 Conformational geometries

With the MP2/6-311++G(d,p) calculations, the largest deviation from the experimental rotational constants is only 41 MHz, while that of MP2/6-311++G(2d,2p), MP2/aug-cc-pVDZ and the mixed basis set, i.e. aug-cc-pVDZ/6-311++G(d,p) is 58 MHz, 101 MHz and 76 MHz, respectively. The detailed comparison is summarized in Table 6-5. Here the MP2/6-311++G(d,p) calculation provides the best agreement. Similar conclusions were made in the previous chapter of studies of the PO–water adduct.

It is noted that the rotational constants alone may not provide enough discrimination for the unambiguous assignment of a particular conformer since some conformers have very similar predicted rotational constants (see Table 6-1). In these cases, the information on the electric dipole moment components and the experimental distinction whether a dimer is homo- or heterochiral, serve as additional identification criteria. The small differences between the observed and the MP2/6-311++G(d,p) rotational constants, as well as the good agreements for the electric dipole moment components lead to the conclusion that the actual structures of the measured dimer species are very close to the MP2/6-311++G(d,p) optimized geometries. The most important intermolecular structural parameters are defined in Figure 6-4 using *RR2* as an example. Here,  $d$  is the H-bonding distance  $O_{\text{epoxy}}\cdots\text{H}$ ;  $\theta$  is the H-bonding angle,  $\angle O_{\text{epoxy}}\cdots\text{H}-\text{C}$ ; and  $\tau$  is  $\angle \text{H}\cdots O_{\text{epoxy}}\cdots\text{H}$ . The subscripts 1, 2, 3, 4 illustrated in Figure 6-4 define the appearance of each set of the structural parameters from top to bottom in every configuration as shown in Figure 6-2.

**Table 6-5** Comparison between the experimental and the *ab initio* calculated rotational constants at the level of MP2 theory in the unit of MHz of the six measured conformers of the PO dimer.

Configurations	RR2	RR4	RR5	RS2	RS4	RS5
Basis set	6-311++G(d,p)					
$\Delta A^a$	13	3	-21	-8	-20	12
$\Delta B$	38	24	38	41	38	23
$\Delta C$	24	23	27	33	27	21
Basis set	6-311++G(2d, 2p)					
$\Delta A$	2	-25	-15	-2	2	15
$\Delta B$	58	47	48	53	52	38
$\Delta C$	42	41	40	50	43	32
Basis set	aug-cc-pVDZ					
$\Delta A$	-60	-74	-89	-45	-98	-102
$\Delta B$	67	46	57	60	65	50
$\Delta C$	44	40	48	54	52	37
Basis set	aug-cc-pVDZ/6-311++G(d,p)					
$\Delta A$	-47	-67	-76	-48	-56	-67
$\Delta B$	57	37	50	51	54	40
$\Delta C$	37	32	39	44	42	31

<sup>a</sup>  $\Delta = (\textit{ab initio} \text{ constants}) - (\text{experimental constants})$ .

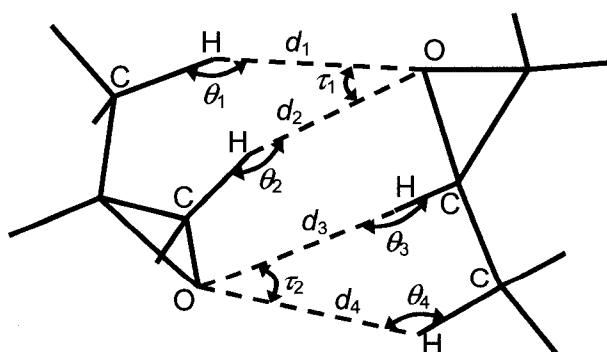


**Figure 6-4** Definition of the most important H-bond structural parameters for PO dimer, using the structure of the RR2 conformer as an example.

The *ab initio* values of these structural parameters for the six observed conformers are listed in Table 6-6. The H-bond length ranges from 2.46 to 2.85 Å, which falls in the general range expected for this type of secondary H-bonds. The H-bond angle varies from 95° to 149°, while the magnitude of  $\tau$  changes from 55° to 60° for the homo- and heterochiral pairs. It is noted that the relative difference between the experimental and calculated *A* rotational constant is the smallest among the three rotational constants and can be either positive or negative. On the other hand, the *ab initio* calculation consistently overestimates the magnitude of *B* and *C* constants by ~4% at the MP2/6-311++G(d,p) level. This implies that the actual structures of the six observed conformers are slightly more compact than predicted.

**Table 6-6** Secondary hydrogen bond structural parameters of the six experimentally observed conformers of PO dimer at the MP2/6-311++G(d,p) calculations.<sup>a</sup>

	<i>RR2</i>	<i>RS2</i>	<i>RR4</i>	<i>RS4</i>	<i>RR5</i>	<i>RS5</i>
$d_1$ /Å	2.502	2.770	2.586	2.617	2.613	2.568
$d_2$ /Å	2.454	2.704	2.692	2.652	2.523	2.562
$d_3$ /Å	2.875	2.463	2.542	2.534	2.811	2.838
$d_4$ /Å	2.577	2.507	2.572	2.576	2.625	2.618
$\theta_1$ /deg	148.8	100.3	120.1	117.3	114.8	117.8
$\theta_2$ /deg	130.8	121.7	114.9	117.7	119.4	116.5
$\theta_3$ /deg	95.6	130.8	125.9	125.9	94.9	94.1
$\theta_4$ /deg	125.3	148.6	145.3	145.1	121.9	122.5
$\tau_1$ /deg	60.1	55.2	55.8	55.9	57.6	57.7
$\tau_2$ /deg	55.2	60.0	57.6	57.8	55.5	55.3

<sup>a</sup> The structural parameters are defined in Figure 6-4.



#### 6.4.2 Secondary hydrogen-bonds and conformational stability

The counterpoise corrected dissociation energies by MP2/6-311++G(d,p) of all the twelve conformers involving four intermolecular secondary H-bonds are about -15 kJ/mol, surprisingly close to those of the strongly H-bonded PO–H<sub>2</sub>O conformers at -21 kJ/mol. Furthermore, the detection of six distinct conformers of this molecular adduct bound only by weak secondary H-bonds is somewhat unexpected since one may expect it to be a floppy system with a relatively flat minimum and large amplitude motions. The experiment shows that even though the dissociation energy of one secondary H-bond is much smaller than a classic H-bond, the sum of all four possible secondary H-bonds could have an effect as large as one strong H-bond. The direct detection of six distinct conformers implies that although these secondary H-bonds are relatively weak in binding strength, they can play a significant role in locking the binding subunits in a specific position. These observations suggest that the secondary H-bond interactions may play an important role in many biological processes, a subject of intense current interest,<sup>33, 34, 35</sup> since secondary H-bonds are very common in the much larger biological systems.<sup>36, 37</sup>

The number of observed structural conformers in supersonic jet experiments is typically much smaller compared to the number of stable species predicted by *ab initio* calculations with appreciable population at thermal equilibrium at room temperature. This can be understood since the collisional relaxation in the jet expansion promotes local minima to collapse to the lowest energy conformer if the dissociation energies of the complexes are small enough that repeated dissociation and recombination occur,<sup>28</sup> or if the interconversion barriers between them are

accessible.<sup>38,39</sup> Because of the large dissociation energies, it is not expected that the repeated dissociation and recombination of the complexes happen substantially under the current experimental condition. The observation of the six structural conformers of PO dimer suggests that the interconversion barriers between these conformers are relatively high and that the collisional relaxations in the helium expansion do not interconvert these conformers readily. It is interesting to note that using heavier carrier gas such as neon seemed to enhance the interconversion between conformers. This point is manifested in the experiments by the fact that only one conformer, i.e. *RR2*, was observed when using Ne as carrier gas instead of He. The intensities of the other five conformers were too weak to be observed, indicating substantial population transferring out of these local minima. This also explains the difficulty encountered in the early stage of the spectral search when Ne was used. The observation may be understood by the fact that the collision energy of He with the complex is much smaller than that with Ne. Recently, Miller III *et al.* reported a theoretical study of collision-induced conformational changes in glycine with He, Ne and Ar.<sup>40</sup> They showed that, in addition to the energy of collision, attractive interactions between the heavier colliding atom such as Ne or Ar and the glycine molecule can catalyze conformer interconversion substantially. This may also be the case here, although detailed theoretical modelling is out of the scope of this chapter.

To establish the relative stability of the observed conformers, the intensities of the same rotational transitions of both the homo- and heterochiral species were measured under the same experimental condition with the same sample mixture using racemic PO. The experimentally observed line intensities, scaled by the respective

calculated dipole moment component values, give the following stability order:  $RR2 > RR4 \approx RS4 > RS5 > RR5 > RS2$ . Comparing to a classic H-bond, one may expect the strength of the  $O_{\text{epoxy}} \cdots H-C$  secondary H-bonds goes qualitatively with the negativity of the carbon atom involved. Since the carbon atoms of the  $CH_2$  and  $CH$  groups are bonded directly to the more electron negative oxygen atom, it is expected that the electron negativity order for the carbon atom of each group to be:  $CH_3 > CH_2 \geq CH$ . For the homochiral diastereomers, the stability order  $RR2$  ( $H3H2R-H3H1R$ )  $>$   $RR4$  ( $H3H2R-H2H1R$ )  $>$   $RR5$  ( $H3H1R-H2H1R$ ) seems to correlate with the sum of the indexes which in turn tell us how many  $CH_3$ ,  $CH_2$  and  $CH$  types of secondary H-bonds there are in each conformer. However, the stability order of the heterochiral conformers is very different even though they utilize the same secondary H-bonds as in the corresponding homochiral pairs. This is because such simple sum rule does not take into account other interactions such as steric hindrance effect, which will be discussed in relation to the chirodiastaltic energies in the next section. The experimental stability order is compared to the order predicted by the *ab initio* calculations in Table 6-7. As one can see, the experimental stability trend is not well captured at either the MP2/6-311++G(d,p) or the MP2/aug-cc-pVDZ levels. Since the MP2/6-311++G(d,p) gives the best agreement with the experimental geometries, single point energy calculation with counterpoise correction were performed at the MP2/aug-cc-pVTZ level with the MP2/6-311++G(d,p) optimized geometries. The accordingly obtained dissociation energies are also listed in Table 6-7 for comparison. However, they do not noticeably improve the degree of the agreement.

**Table 6-7** Experimental results and theoretical dissociation energies and chirodiastaltic energies (in kJ/mol) at the level of MP2 theory of the six observed conformers of PO dimer.

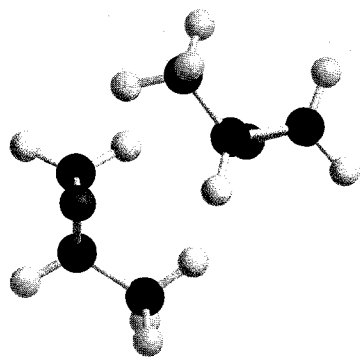
Obs. Conf.	Exp. Sign	6-311++G(d,p)		aug-cc-pVDZ		aug-cc-pVTZ <sup>a</sup>	
		$D_e+CP$	$\Delta E_{chir}$	$D_e+CP$	$\Delta E_{chir}$	$D_e+CP$	$\Delta E_{chir}$
<i>RR2</i>	<0	-14.97	-0.06	-18.09	-0.10	-19.45	0.24
<i>RS2</i>		-14.91		-17.99		-19.69	
<i>RR4</i>	~0	-14.79	0.13	-17.65	0.10	-19.51	0.03
<i>RS4</i>		-14.92		-17.75		-19.54	
<i>RR5</i>	>0	-14.22	0.00	-17.12	-0.03	-18.90	-0.09
<i>RS5</i>		-14.22		-17.09		-18.81	

<sup>a</sup> Single point energy calculation using MP2/aug-cc-pVTZ at the MP2/6-311++G(d,p) optimized geometries.

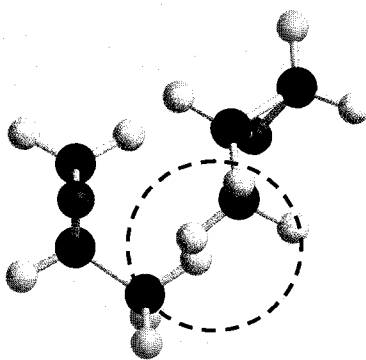
#### 6.4.3 Chirodiastaltic energies

For a chiral complex pair, the two homochiral ones,  $RR'$  and  $SS'$  have identical dissociation energies,  $\Delta E_{hom} \equiv \Delta E(RR') = \Delta E(SS')$ , and give rise to the same spectrum. This is also true for the heterochiral partners,  $\Delta E_{het} \equiv \Delta E(RS') = \Delta E(SR')$ . The small energy difference between a homochiral pair ( $RR'$  or  $SS'$ ) and a heterochiral complex ( $RS'$  or  $SR'$ ),  $\Delta E_{chir} \equiv \Delta E_{hom} - \Delta E_{het}$  is the energy term responsible for chiral recognition.<sup>41</sup> The term  $\Delta E_{chir}$  is called the *chirodiastaltic energy* as diastaltic means “serving to distinguish”, introduced by Craig and Mellor in the context of chirally discriminating intermolecular interactions.<sup>42</sup> This *chirodiastaltic energy* is central for understanding the mechanisms of chiral recognition, enantioselective reactions and multiple short-range stereospecific effects in life science. A negative sign of  $\Delta E_{chir}$  means that homochiral diastereomer is favored over the heterochiral one. According to the experimental observation, the largest negative chirodiastaltic energy among the six

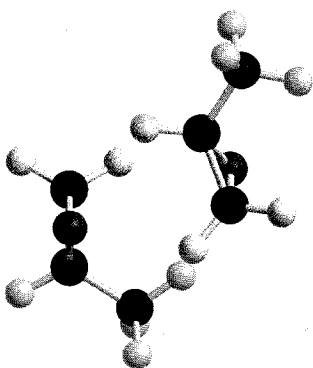
observed homo- and heterochiral diastereomers was found for the *RR2* and *RS2* pair where the *RR* conformer is favored. This is followed by a fairly small  $\Delta E_{\text{chir}}$  for the *RR4* and *RS4* pair. A positive  $\Delta E_{\text{chir}}$  was noted for the *RR5* and *RS5* pair where the heterochiral complex is preferred over the homochiral one. To aid the visualization, the  $\text{HxHyR-Hx'Hy'R/S}$  notation introduced earlier will be helpful. As shown in Figure 6-5, the first subunit is fixed at the same position in each diastereomeric pair. One may correlate the chiral self-recognition observed here with the spatial orientation of the “discriminating” methyl group in the second subunit since this is the largest functional group attached to the stereogenic centre. The distance between the two methyl C atoms in *RS2* (*H3H2R-H3H1S*) is 3.984 Å as compared to 4.906 Å in *RR2* (*H3H2R-H3H1R*). *RS2* is therefore much less favored over *RR2* because of the steric hindrance experienced by the two methyl groups. Furthermore, since this discriminating methyl group is directly utilized in the secondary H-bonds, this pair has therefore the largest chiral discrimination energy. In the *RR4* and *RS4* (*H3H2R-H2H1R/S*) pair, chirality has little effect on their relative stability since the “discriminating” methyl group points away from the binding sites in both *RR4* and *RS4*. In the last pair, *RR5* (*H3H1R-H2H1R*) is less favored with a distance of 4.902 Å between the two methyl carbon atoms compared to 5.679 Å in *RS5* (*H3H1R-H2H1S*). The overall discrimination effect, however, is smaller than in the *RR2* and *RS2* pair since the discriminating methyl group is further away from the binding sites and the two methyl groups are further apart than in the *RR/RS2* pair.



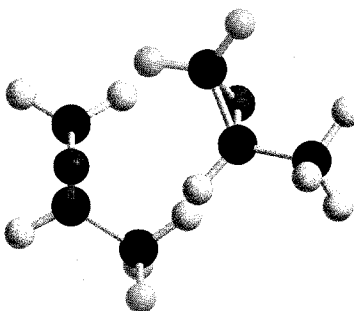
*RR2*



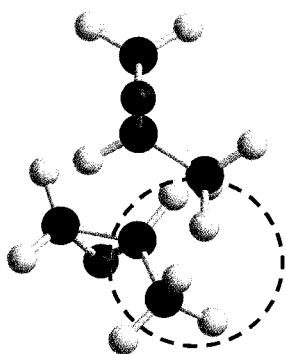
*RS2*



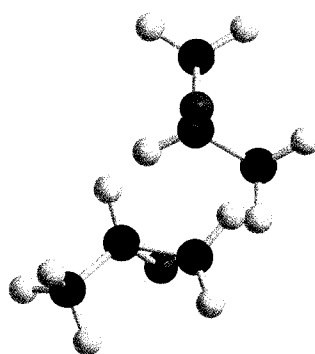
*RR4*



*RS4*



*RR5*



*RS5*

**Figure 6-5** Orientation of the six experimentally observed conformers of PO dimer. From left to right and top to bottom are the configurations H3H2R-H3H1R (*RR2*); H3H2R-H3H1S (*RS2*); H3H2R-H2H1R (*RR4*); H3H2R-H2H1S (*RS4*); H3H1R-H2H1R (*RR5*); H3H1R-H2H1S (*RS5*). The steric hindrance due to the methyl group is emphasized by dashed circles.

The *ab initio*  $\Delta E_{\text{chir}}$  values for these six conformers are estimated using their corresponding counterpoise corrected dissociation energies and are listed in Table 6-7 for comparison. It appears that even with the fairly large basis set such as aug-cc-pVTZ, it is still challenging for theoretical calculations to capture the subtle chiral recognition energy which can be unambiguously detected experimentally at present time. The current experimental data for a relatively simple chiral diastereomer may serve as a benchmark system for future theoretical development in energy evaluation of this important class of molecular systems.

## 6.5 Concluding remarks

In summary, PO dimer was investigated with high level *ab initio* methods and rotational spectroscopy. Three homochiral and the three corresponding heterochiral conformers of PO dimer were observed and assigned. The stability order and the sign of chiral recognition energies were determined experimentally and the role of secondary H-bonds in chiral recognition was demonstrated. This is the first time that *both* homo- and the corresponding heterochiral dimers have been unambiguously identified via high resolution spectroscopy. The present results also show that the overall effect of several secondary H-bonds could be as significant as a single classic H-bond in stabilizing diastereomers and in determining spatial orientations of the binding partners.

## References

---

1. *Nomenclature of Organic Chemistry*, Oxford:Pergamon Press, **1979**; *A Guide to IUPAC Nomenclature of Organic Compounds, Recommendations 1993*, Oxford:Blackwell Scientific Publications, **1993**.
2. Cantor, C. R.; Schimmel, P. R. *Biophysical Chemistry*, W. H. Freeman: San Francisco, **1980**.
3. Pirkle, W. H.; Pochapsky, T. G. *Chem. Rev.* **1989**, *89*, 347.
4. Parker, D. *Chem. Rev.* **1991**, *91*, 1441.
5. Buckingham, A. D.; Fischer, P. *Chem. Phys.* **2006**, *324*, 111.
6. Soloshonok, V. A. *Angew. Chem. Int. Ed.* **2006**, *45*, 165.
7. Alrabaa, A.; Le Barbu, K.; Lahmani, F.; Zehnacker-Rentien, A. *J. Phys. Chem. A* **1997**, *101*, 3273.
8. Le Barbu, K.; Brenner, V.; Millié, Ph.; Lahmani, F.; Zehnacker-Rentien, A. *J. Phys. Chem. A* **1998**, *102*, 128.
9. Piccirillo, S.; Bosman, C.; Toja, D.; Giardini-Guidoni, A.; Pierini, M.; Troiani, A.; Speranza, M. *Angew. Chem. Int. Ed.* **1995**, *36*, 1729.
10. Latinia, A.; Toja, D.; Giardini-Guidoni, A.; Piccirillo, S.; Speranza, M. *Angew. Chem. Int. Ed.* **1999**, *38*, 815.
11. Borho, N.; Haber, Th.; Suhm, M. A. *Phys. Chem. Chem. Phys.* **2001**, *3*, 1945.
12. Borho, N.; Suhm, M. A. *Phys. Chem. Chem. Phys.* **2002**, *4*, 2721.
13. Borho, N.; Suhm, M. A. *Org. Biomol. Chem.* **2003**, *1*, 4351.
14. Adler, T. B.; Borho, N.; Reiher, M.; Suhm, M. A. *Angew. Chem.* **2006**, *45*, 3440.
15. Emmeluth, C.; Dyczmons, V.; Kinzel, T.; Botschwina, P.; Suhm, M. A.; Yáñez, M. *Phys. Chem. Chem. Phys.* **2005**, *7*, 991.
16. Scharge, T.; Emmeluth, C.; Häber, T.; Suhm, M. A. *J. Mol. Struct.* **2006**, *786*, 86.
17. King, A. K.; Howard, B. J. *Chem. Phys. Lett.* **2001**, *348*, 343.
18. Hearn, J. P. I.; Cobley, R. V.; Howard, B. J. *J. Chem. Phys.* **2005**, *123*, 134324.



- 
19. Borho, N.; Xu, Y. *Angew. Chem. Int. Ed.* **2006**, *46*, 2276.
  20. Portmann, S.; Inauen, A.; Lüthi, H. P.; Leutwyler, S. *J. Chem. Phys.* **2000**, *113*, 9577.
  21. Alkorta, I.; Elguero, J. *J. Am. Chem. Soc.* **2002**, *124*, 1488.
  22. Alkorta, I.; Elguero, J. *J. Chem. Phys.* **2002**, *117*, 6463.
  23. Frisch, M. J. *et al.* GAUSSIAN03 (Revision B.01): see Chapter 4 References.
  24. Binkley, J. S.; Pople, J. A. *Int. Quantum Chem.* **1975**, *9*, 229.
  25. Krishnan, R.; Binkley, J. S.; Seeger, R.; Pople, J. A. *J. Chem. Phys.* **1980**, *72*, 650.
  26. Boys, S. F.; Bernardi, F. *Mol. Phys.* **1970**, *10*, 553.
  27. Woon, D. E.; Dunning, T. H. Jr. *J. Chem. Phys.* **1993**, *98*, 1358.
  28. Xu, Y.; Jäger, W. *J. Chem. Phys.* **1997**, *106*, 7968.
  29. Tatamitani, Y.; Liu, B.; Shimada, J.; Ogata, T.; Ottaviani, P.; Maris, A.; Caminati, W.; Alonso, J. L. *J. Am. Chem. Soc.* **2002**, *124*, 2739.
  30. Xu, Y.; Jäger, W. *J. Chem. Phys.* **1997**, *107*, 4788.
  31. Dijkerman, H. A.; Ruitenberg, G. *Chem. Phys. Lett.* **1969**, *3*, 172.
  32. Watson, J. K. G. *Vibrational Spectra and Structure: A Series of Advances*, edited by Durig, J. R.; Elsevier: New York/Amsterdam, **1977**, Vol. 6, p1.
  33. Desiraju, G. R. *The Weak Hydrogen Bond in Structural Chemistry and Biology*, edited by Steiner, T.; Oxford University Press Inc: New York, **1999**.
  34. Hobza, P.; Havlas, Z. *Chem. Rev.* **2000**, *100*, 4253.
  35. Desiraju, G. R. *Chem. Commun.* **2005**, *24*, 2995.
  36. Derewenda, Z. S.; Lee, L.; Derewenda, U. *J. Mol. Biol.* **1995**, *252*, 248.
  37. Wahl, M.; Sundaralingam, M. *Trends Biochem. Sci.* **1997**, *22*, 97.
  38. Godfrey, P. D.; Rodgers, F. M.; Brown, R. D. *J. Am. Chem. Soc.* **1997**, *119*, 2232.

- 
39. Godfred, P. D.; Brown, R. D. *J. Am. Chem. Soc.* **1998**, *120*, 10724.
40. Miller, III, T.F.; Clary, D. C; Meijer, A. J. H. M. *J. Chem. Phys.* **2005**, *122*, 244323.
41. Portmann, S.; Inauen, A.; Lüthi, H. P.; Leutwyler, S. *J. Chem. Phys.* **2000**, *113*, 9577.
42. Craig, D. P; Mellor, D. P. *Top. Curr. Chem.* **1976**, *63*, 1.

\*\*\*\*\*

## CHAPTER 7

### CONCLUSIONS

\*\*\*\*\*

To gain insights into the chiral discrimination phenomenon at the molecular level, I have investigated several chiral molecular systems using spectroscopic and computational methods during my PhD work. Specifically, propylene oxide (PO) has been chosen for the main study since it is one of the smallest, rigid, and chemically stable chiral molecules. The rovibrational studies of the PO monomer and rotational studies of four molecular complexes, namely PO–Ne, PO–H<sub>2</sub>O, PO–(H<sub>2</sub>O)<sub>2</sub> and PO–PO, are reported in this thesis. *Ab initio* calculations were carried out to complement the data analysis. Both experimental and theoretical results have been discussed in Chapters 4 to 6. In the following, I summarize the significant results of my thesis which contribute to the understanding of the roles of hydrogen bonds and van der Waals interactions in the chiral recognition processes.

High resolution IR spectroscopy can provide accurate information about the rotational energy levels in both the ground and vibrationally excited states, as well as information on the vibrational shifts that are signatures of the particular functional groups involved in the chiral recognition interactions. The measurements of rovibrational spectra of the PO monomer at the C–H stretching vibration modes demonstrate the potential of the rapid scan mid-IR lead salt diode laser spectrometer

for probing vibrationally excited states of chiral molecules and their complexes. The vibrational band centers of two C–H vibrational motions were derived. This work also shows the significant challenge of sorting out the very complicated rovibrational spectra.

Experimental studies of chiral molecules and/or molecular complexes are complicated by the large number of potential structural conformers and the involved spectral pattern associated with asymmetric molecules. Therefore, high level *ab initio* calculations are essential to guide initial spectral searches and to interpret the spectroscopic data. One can in turn use the experimental analysis to judge the quality of the theoretical predictions and develop appropriate models for further calculations. In parallel to the experimental efforts, extensive *ab initio* calculations were carried for the PO containing complex systems and the quality of the theoretical predictions was judged by comparison with the experimental analysis. I have found empirically that the MP2/6-311++G(d,) level of theory is very effective in guiding rotational spectroscopic studies of small chiral molecular systems. The largest deviation of calculated rotational constants from experimental values is only  $\pm 1.5\%$  in the PO–H<sub>2</sub>O complex,  $\pm 3.6\%$  in the PO–(H<sub>2</sub>O)<sub>2</sub> system, and  $\pm 4\%$  for PO–PO dimer. The good agreement between the experimental and predicted rotational constants implies that the actual structures of these complexes are very close to the *ab initio* optimized geometries.

In the previous studies of organic–water molecular complexes using high resolution spectroscopy, only the lowest energy conformer could be detected experimentally.<sup>1, 2, 3, 4, 5, 6, 7, 8, 9</sup> In my studies of the PO–water system, two distinct

structural conformers of both PO–H<sub>2</sub>O binary and PO–(H<sub>2</sub>O)<sub>2</sub> ternary complexes, namely *syn*- and *anti*-configurations were detected experimentally. Furthermore, rotational spectra of six, three homo- and heterochiral conformer pairs of the PO–PO dimer were measured and analyzed. This is the first time that both homo- and the corresponding heterochiral dimers have been unambiguously identified via high resolution spectroscopy. This novel result is certainly encouraging for more studies on chiral recognition effects, for example, rotational spectra of all six possible hydrogen-bonded PO–ethanol (EtOH) conformers were detected and analyzed.<sup>10</sup>

From the pure rotational studies, I obtained detailed structural information about the chiral molecular complexes. In the PO–H<sub>2</sub>O molecular system, values of six H-bonding structural parameters are derived from the experimental rotational constants. For example, H-bonding length  $r(\text{O}_{\text{epoxy}}\cdots\text{H})$  is  $\sim 1.9$  Å and H-bonding angle  $\phi$  [ $\angle(\text{O}_{\text{epoxy}}\cdots\text{H}-\text{O})$ ] is  $\sim 170^\circ$ , in the range of classic H-bond. In the PO–(H<sub>2</sub>O)<sub>2</sub> ternary complex, the distance between the two oxygen atoms in the two water molecules,  $r(\text{O}_{\text{w1}}-\text{O}_{\text{w2}})$ , is determined to be 2.82 Å. This separation and the distance  $r(\text{O}_{\text{w1}}\cdots\text{H})$  are about 0.1 to 0.2 Å shorter in PO–(H<sub>2</sub>O)<sub>2</sub> than in (H<sub>2</sub>O)<sub>2</sub>, while the hydrogen bonding angle  $\angle(\text{O}_{\text{w1}}\cdots\text{H}-\text{O}_{\text{w2}})$  deviates further from linearity in PO–(H<sub>2</sub>O)<sub>2</sub> than in (H<sub>2</sub>O)<sub>2</sub>. It is suggested that these changes are made in order to maximize the interactions between water and PO, i.e. to best solvate the PO molecule with water molecules. It was also noted that  $r(\text{O}_{\text{epoxy}}\cdots\text{H})$  of the primary hydrogen bond between PO and water is about 0.1 Å shorter in the ternary PO–(H<sub>2</sub>O)<sub>2</sub> cluster than in the binary PO–H<sub>2</sub>O complex. For the PO–PO dimer, the H-bond length ranges from 2.46 to 2.85 Å, which falls in the general range expected for this type of secondary H-bonds.

The H-bond angle varies from  $95^\circ$  to  $149^\circ$ , while the magnitude of  $\tau$  changes from  $55^\circ$  to  $60^\circ$  for the homo- and heterochiral pairs.

The success of studying PO with one water molecule is a significant step towards understanding the chemistry taking place in the aqueous environment. However, from one water molecule to the solution phase, there is still a big gap that needs bridging. Therefore, I carried out detailed studies of the sequential complexation of PO with a few water molecules. The results for 1:2 PO–H<sub>2</sub>O complexes have established the geometries and stability ordering of the two ternary conformers. The experimental observations show that the *anti*-PO–(H<sub>2</sub>O)<sub>2</sub> conformer is favored over the *syn*-PO–(H<sub>2</sub>O)<sub>2</sub>. This observation is opposite to *syn* over *anti* for the PO–H<sub>2</sub>O complex, but in accord with what is predicted for PO in aqueous solution. This study clearly demonstrates how the stabilities of conformers can change during the initial steps of hydration. It would be of great interest to follow the solvation process by sequentially solvating PO with more water molecules and conclusively establishing the trend. *Ab initio* calculations of PO solvated with three and four water molecules indicate the feasibility of following the solvation process experimentally.

One key question in chiral recognition is how the intermolecular forces come together in a concerted way to enable a chiral molecule to differentiate another chiral molecule from its mirror image. The study of PO–PO fulfills the ultimate goal of my thesis work, to understand the chiral discriminating forces at play in one chiral molecular system. The results show that even though the dissociation energy of one secondary H-bond is much smaller than a classic H bond, the sum of all four possible secondary H-bonds have an effect as large as one strong H-bond. The direct detection

of six distinct conformers demonstrates that the concerted effort of the weak secondary hydrogen bonds (the  $O_{\text{epoxy}}\cdots\text{H}-\text{C}$  noncovalent interactions) can successfully lock the subunits in a particular orientation and that the overall binding strength is comparable to a classic H bond. In addition, the conformational stability ordering was established and the sign of chiral recognition energies, a central quantity in chiral discrimination process, was determined experimentally. The role of secondary H-bonds in chiral recognition was demonstrated. These observations suggest that the secondary H-bond interactions may play an important role in many biological processes, a subject of intense current interest,<sup>11, 12, 13</sup> since secondary H-bonds are very common in the much larger biological systems.

The very limited high resolution spectroscopic data of chiral molecular systems highlights the fact that unambiguous assignments of rotationally and/or rovibrationally resolved spectra of chiral molecular systems are a daunting task.

My doctoral work demonstrates the great potential of high resolution microwave spectroscopy in combination with quantum chemistry computations for exploring the interactions in chiral molecular systems. In general, a further step towards the goal of understanding chiral discrimination at the microscopic level would be the extension of vibrational ground state studies to excited states. That is an even more challenging area as significant intermode couplings may occur and, therefore, complicate the spectroscopic task. It will also be of great interest to study other related chiral molecular complexes such as glycidol, where one may expect stronger chiral recognition effect because of the presence of more functional groups, such as the OH group.

## References

---

1. Kang, C.; Pratt, D. W. *Int. Rev. Phys. Chem.* **2005**, *24*, 1.
2. Gutowsky, H. S.; Emilsson, T.; Arunan, E. *J. Chem. Phys.* **1993**, *99*, 4883.
- 3 Gerhards, M.; Schmitt, M.; Kleinermanns, K.; Stahl, W. *J. Chem. Phys.* **1996**, *104*, 967.
4. Melandri, S.; Maris, A.; Favero, P. G.; Caminati, W. *Chem. Phys.* **2002**, *283*, 185.
5. Caminati, W.; Moreschini, P.; Rossi, I.; Favero, P. G. *J. Am. Chem. Soc.* **1998**, *120*, 11144.
6. Paolo, O.; Giuliano, M.; Velino, B.; Caminati, W. *Chem. Eur. J.* **2004**, *10*, 538.
7. Sanz, M. E.; López, J. C.; Alonso, J. L.; Maris, A.; Favero, P. G.; Caminati, W. *J. Phys. Chem. A* **1999**, *103*, 5285.
8. Caminati, W.; Dell'Erba, A.; Melandri, S.; Favero, P. G. *J. Am. Chem. Soc.* **1998**, *120*, 5555.
9. Spoerel, U.; Stahl, W.; Caminati, W.; Favero, P. G. *Chem. Eur. J.* **1998**, *4*, 1974.
10. Borho, N.; Xu, Y. *Angew. Chem. Int. Ed.* **2006**, *46*, 2276.
11. Desiraju, G. R. *The Weak Hydrogen Bond in Structural Chemistry and Biology*, edited by Steiner, T.; Oxford University Press Inc: New York, **1999**.
12. Hobza, P.; Havlas, Z. *Chem. Rev.* **2000**, *100*, 4253.
13. Desiraju, G. R. *Chem. Commun.* **2005**, *24*, 2995.



## Appendix 1

Tables of microwave transition frequencies measured  
for the PO containing complexes

**Table A1-1** Measured rotational transition frequencies of the PO–Ne Complex.

$J_{KaKc} - J'_{Ka'Kc'}$	PO– <sup>20</sup> Ne	PO– <sup>22</sup> Ne
	$\nu_{\text{obs}}/\text{MHz}$	$\nu_{\text{obs}}/\text{MHz}$
1 <sub>10</sub> – 1 <sub>01</sub>	4953.3337 (-5) <sup>a</sup>	5035.6407 (12)
1 <sub>11</sub> – 0 <sub>00</sub>	8615.2802 (4)	8526.5557 (18)
1 <sub>10</sub> – 0 <sub>00</sub>	9073.7710 (6)	8938.8154 (3)
2 <sub>02</sub> – 1 <sub>01</sub>	8206.9113 (-14)	7779.3905 (-7)
2 <sub>11</sub> – 1 <sub>10</sub>	8697.5613 (7)	8216.9664 (8)
2 <sub>12</sub> – 1 <sub>11</sub>	7780.8878 (1)	7392.7163 (-5)
2 <sub>20</sub> – 2 <sub>11</sub>	13517.3709 (-9)	13896.0346 (11)
2 <sub>11</sub> – 2 <sub>02</sub>	5443.9857 (-4)	5473.2195 (-2)
2 <sub>21</sub> – 2 <sub>12</sub>	14859.3187 (4)	15106.2664 (9)
2 <sub>12</sub> – 1 <sub>01</sub>	12275.7314 (-13)	12016.1002 (-7)
2 <sub>20</sub> – 2 <sub>12</sub>	14892.5350 (1)	15132.5447 (5)
2 <sub>21</sub> – 2 <sub>11</sub>	13484.1534 (6)	13869.7594 (-17)
2 <sub>11</sub> – 1 <sub>01</sub>	13650.8937 (15)	13252.6100 (-9)
3 <sub>21</sub> – 2 <sub>20</sub>	12484.5502 (-38)	11806.1898 (5)
3 <sub>03</sub> – 2 <sub>02</sub>	12226.6575 (-3)	11602.4443 (-4)
3 <sub>12</sub> – 2 <sub>11</sub>	13022.6916 (-21)	12306.5797 (-3)
3 <sub>13</sub> – 2 <sub>12</sub>	11649.9486 (-5)	11071.9084 (-5)
3 <sub>22</sub> – 2 <sub>21</sub>	12352.8898 (38)	11701.8331 (12)
3 <sub>21</sub> – 3 <sub>12</sub>	12979.2263 (6)	13395.6479 (-14)
3 <sub>12</sub> – 3 <sub>03</sub>	6240.0175 (2)	6177.3544 (4)
3 <sub>22</sub> – 3 <sub>13</sub>	15562.2652 (-6)	15736.1934 (2)
3 <sub>13</sub> – 2 <sub>02</sub>	15718.7671 (13)	15308.6176 (0)
3 <sub>03</sub> – 2 <sub>12</sub>	8157.8343 (26)	7365.7315 (27)
3 <sub>21</sub> – 3 <sub>13</sub>	15727.1334 (0)	15866.8305 (-29)
3 <sub>22</sub> – 3 <sub>12</sub>	12814.3590 (-8)	13265.0074 (51)
3 <sub>12</sub> – 2 <sub>02</sub>		17779.7995 (-8)
3 <sub>03</sub> – 2 <sub>11</sub>	6782.6729 (-11)	6129.2262 (-16)
4 <sub>22</sub> – 3 <sub>21</sub>	16763.3925 (-34)	15835.4771 (23)
4 <sub>04</sub> – 3 <sub>03</sub>	16152.4916 (-13)	15349.6242 (-12)
4 <sub>31</sub> – 3 <sub>30</sub>	16528.4601 (60)	
4 <sub>13</sub> – 3 <sub>12</sub>	17317.3396 (10)	16372.0962 (-16)
4 <sub>32</sub> – 3 <sub>31</sub>	16519.5092 (-57)	
4 <sub>14</sub> – 3 <sub>13</sub>	15495.4180 (6)	14731.9506 (-8)

**Table A1-1 (Continued)**

$J_{KaKc} - J'_{Ka'Kc'}$	PO- <sup>20</sup> Ne	PO- <sup>22</sup> Ne
	$\nu_{\text{obs}}/\text{MHz}$	$\nu_{\text{obs}}/\text{MHz}$
4 <sub>23</sub> - 3 <sub>22</sub>	16441.6991 (20)	15579.2534 (-12)
4 <sub>22</sub> - 4 <sub>13</sub>	12425.2740 (14)	12859.0317 (-4)
4 <sub>13</sub> - 4 <sub>04</sub>	7404.8674 (6)	7199.8238 (25)
4 <sub>23</sub> - 4 <sub>14</sub>	16508.5487 (-16)	16583.49757 (-16)
4 <sub>04</sub> - 3 <sub>13</sub>	12660.37809 (11)	11643.4470 (23)
4 <sub>23</sub> - 4 <sub>13</sub>	11938.7183 (3)	12472.17001 (2)
4 <sub>04</sub> - 3 <sub>12</sub>	9912.4731 (-4)	9172.2681 (1)
5 <sub>14</sub> - 5 <sub>05</sub>	9001.5889 (5)	

<sup>a</sup>The residuals (obs-calc) in parentheses are expressed in units of the last digits.

**Table A1-2** Experimental transition frequencies (MHz) of the *syn*-PO–H<sub>2</sub>O and *anti*-PO–H<sub>2</sub>O conformers.

$J_{KaKc} - J'_{Ka'Kc'}$	<i>syn</i> -PO–H <sub>2</sub> O	<i>anti</i> -PO–H <sub>2</sub> O
1 <sub>01</sub> – 0 <sub>00</sub>	5388.4336 (16) <sup>a</sup>	4362.0899 (44)
1 <sub>10</sub> – 1 <sub>01</sub>		7398.3921 (60)
1 <sub>11</sub> – 0 <sub>00</sub>	8415.9695 (-19)	11559.4636 (61)
1 <sub>10</sub> – 0 <sub>00</sub>	9098.9856 (-12)	
2 <sub>02</sub> – 1 <sub>01</sub>	10673.6683 (10)	8719.8967 (26)
2 <sub>11</sub> – 1 <sub>10</sub>	11459.5264 (-30)	8925.1946 (26)
2 <sub>12</sub> – 1 <sub>11</sub>	10093.5815 (26)	8523.2116 (-9)
2 <sub>11</sub> – 2 <sub>02</sub>		7603.6870 (29)
2 <sub>12</sub> – 1 <sub>01</sub>	13121.1188 (5)	15720.5913 (68)
2 <sub>11</sub> – 1 <sub>01</sub>	15170.0844 (3)	16323.5780 (-2)
3 <sub>21</sub> – 2 <sub>20</sub>	16561.2025 (-5)	13103.2601 (32)
3 <sub>03</sub> – 2 <sub>02</sub>	15767.1860 (9)	13069.1687 (23)
3 <sub>12</sub> – 2 <sub>11</sub>	17118.8105 (-12)	13384.7918 (-4)
3 <sub>13</sub> – 2 <sub>12</sub>	15079.9261 (10)	12781.9920 (-56)
3 <sub>22</sub> – 2 <sub>21</sub>	16163.7808 (-5)	13086.7248 (35)
3 <sub>12</sub> – 3 <sub>03</sub>	5848.0459 (25)	7919.3155 (56)
3 <sub>21</sub> – 3 <sub>12</sub>	8628.6532 (0)	
4 <sub>04</sub> – 3 <sub>03</sub>		17405.7149 (16)
4 <sub>13</sub> – 3 <sub>12</sub>		17840.7196 (72)
4 <sub>14</sub> – 3 <sub>13</sub>		17037.4728 (19)
4 <sub>04</sub> – 3 <sub>13</sub>		10692.1989 (72)

<sup>a</sup>The residuals (obs-calc) in parentheses are expressed in units of the last digits.

**Table A1-3** Experimental transition frequencies (MHz) of the deuterated isotopomers of the PO–water complex.

$J_{KaKc} - J'_{Ka'Kc'}$	<i>syn</i> -configuration		
	PO–DOH	PO–HOD	PO–DOD
1 <sub>01</sub> – 0 <sub>00</sub>	5322.3463 (-5) <sup>a</sup>	5127.5105 (-48)	5070.3330 (-40)
1 <sub>11</sub> – 0 <sub>00</sub>	8379.4690 (-1)		8269.7922 (16)
2 <sub>02</sub> – 1 <sub>01</sub>	10547.1547 (16)	10173.0522 (38)	10062.7437 (36)
2 <sub>11</sub> – 1 <sub>10</sub>	11310.2990 (-5)	10873.2482 (4)	10744.8559 (-6)
2 <sub>12</sub> – 1 <sub>11</sub>	9978.4903 (-8)	9636.2592 (-3)	9535.9761 (5)
2 <sub>12</sub> – 1 <sub>01</sub>	13035.6134 (1)		12735.4276 (-16)
3 <sub>21</sub> – 2 <sub>20</sub>	16342.0141 (0)		15512.7257 (0)
3 <sub>03</sub> – 2 <sub>02</sub>	15589.9659 (-10)	15063.7182 (-10)	14907.4824 (-18)
3 <sub>12</sub> – 2 <sub>11</sub>	16899.0059 (2)	16254.4912 (-2)	16064.7496 (3)
3 <sub>13</sub> – 2 <sub>12</sub>	14910.5039 (7)	14406.0034 (3)	14257.8913 (10)
	<i>anti</i> -configuration		
	PO–DOH	PO–HOD	PO–DOD
1 <sub>01</sub> – 0 <sub>00</sub>	4303.3432 (-37)	4171.1047 (-61)	4119.5637 (-34)
1 <sub>11</sub> – 0 <sub>00</sub>	11501.0803 (59)		11326.6329 (-38)
2 <sub>02</sub> – 1 <sub>01</sub>	8602.6855 (23)	8338.6333 (50)	8235.7129 (13)
2 <sub>11</sub> – 1 <sub>10</sub>	8801.2832 (25)	8526.5561 (0)	8418.9126 (-4)
2 <sub>12</sub> – 1 <sub>11</sub>	8412.1592 (34)	8157.8353 (-1)	8059.4328 (121)
2 <sub>12</sub> – 1 <sub>01</sub>	15609.8774 (-59)		15266.4941 (38)
3 <sub>03</sub> – 2 <sub>02</sub>	12894.0137 (-8)	12498.8793 (-13)	12345.0256 (42)
3 <sub>12</sub> – 2 <sub>11</sub>	13199.1125 (11)		12625.9886 (2)
3 <sub>13</sub> – 2 <sub>12</sub>	12615.5936 (12)	12233.1569 (1)	12086.8326 (185)
4 <sub>04</sub> – 3 <sub>03</sub>	17173.4078 (-11)		16444.1256 (-20)
4 <sub>13</sub> – 3 <sub>12</sub>	17593.5046 (3)		16111.6061 (59)
4 <sub>14</sub> – 3 <sub>13</sub>	16815.9204 (5)		

<sup>a</sup> The residuals (obs-calc) in parentheses are expressed in units of the last digits.

**Table A1-4** Experimental transition frequencies of unassigned lines in the sample mixture of racemic PO and water using helium as carrier gas in the range of 4-9 GHz.

Frequency /MHz	S/N (cycles)
4003.5247	103 (500)
5061.5325	44 (100)
5127.5212	128 (500)
5259.009	88 (100)
5297.9553	1057 (100)
5332.3434	872 (100)
5359.4055	486 (500)
5371.7	31 (200)
5379.315	131 (200)
5438.336	291 (100)
5477.5133	2039 (100)
5507.5216	110 (100)
5578.3455	1089 (100)
5797.0442	118 (100)
5811.7796	52 (100)
5961.2577	112 (500)
5982.7537	329 (500)
6047.1746	221 (100)
6977.9053	70 (500)
7209.2478	198 (500)
7944.0888	263 (5)
8108.25	437 (100)
8154.3735	228 (20)
8415.9974	283 (100)
8447.8168	132 (200)
8474.8903	56 (200)
8495.6795	189 (200)
8852.9548	14 (500)

**Table A1-5** Observed rotational transition frequencies (MHz) of several isotopomers of the two PO-(H<sub>2</sub>O)<sub>2</sub> conformers.

$J_{KaKc} - J'_{Ka'Kc'}$	$syn\text{-}PO\text{-}H_2^{16}O\text{-}H_2^{16}O$	$syn\text{-}PO\text{-}H_2^{18}O\text{-}H_2^{18}O$	$anti\text{-}PO\text{-}H_2^{16}O\text{-}H_2^{16}O$
2 <sub>02</sub> - 1 <sub>01</sub>	6586.2315 (1) <sup>a</sup>	6223.9207 (6)	5668.4844 (-16)
2 <sub>12</sub> - 1 <sub>11</sub>	6415.4960 (8)	6044.1831 (-4)	5464.9394 (37)
2 <sub>11</sub> - 1 <sub>10</sub>	6790.9405 (-13)	6443.6926 (-19)	5901.3794 (-53)
3 <sub>03</sub> - 2 <sub>02</sub>	9838.6055 (-12)	9286.9732 (-3)	8466.3191 (-22)
3 <sub>13</sub> - 2 <sub>12</sub>	9612.9333 (-12)	9054.2161 (-5)	8188.4171 (-5)
3 <sub>12</sub> - 2 <sub>11</sub>	10175.1266 (-5)	9652.2064 (7)	8842.4520 (-9)
3 <sub>22</sub> - 2 <sub>21</sub>	9904.6039 (36)	9365.6936 (-35)	
3 <sub>21</sub> - 2 <sub>20</sub>	9971.7352 (34)	9444.5588 (-4)	
4 <sub>04</sub> - 3 <sub>03</sub>	13043.7821 (-10)	12298.2388 (3)	11222.9206 (5)
4 <sub>14</sub> - 3 <sub>13</sub>	12799.3051 (-1)	12051.4694 (-8)	10901.9601 (-30)
4 <sub>13</sub> - 3 <sub>12</sub>	13544.3904 (-8)	12842.9161 (22)	11771.0895 (5)
4 <sub>23</sub> - 3 <sub>22</sub>	13192.6463 (-1)	12471.7593 (6)	11354.3777 (46)
4 <sub>22</sub> - 3 <sub>21</sub>	13354.9024 (-12)	12661.0328 (-13)	11497.5596 (12)
4 <sub>31</sub> - 3 <sub>30</sub>	13242.7551 (20)	12531.2757 (7)	11396.9402 (30)
4 <sub>32</sub> - 3 <sub>31</sub>	13236.9721 (-36)	12523.7408 (35)	
5 <sub>05</sub> - 4 <sub>04</sub>	16202.3902 (15)	15257.5993 (10)	13931.5241 (22)
5 <sub>15</sub> - 4 <sub>14</sub>	15972.9199 (-3)	15034.2581 (20)	13603.5947 (-25)
5 <sub>14</sub> - 4 <sub>13</sub>	16891.4799 (5)	16006.9330 (17)	14681.6679 (3)
5 <sub>23</sub> - 4 <sub>22</sub>	16773.7181 (3)	15915.4216 (-10)	14450.0305 (44)
5 <sub>24</sub> - 4 <sub>23</sub>		15564.3934 (-23)	14174.3057 (24)
5 <sub>33</sub> - 4 <sub>32</sub>		15665.2325 (4)	
5 <sub>32</sub> - 4 <sub>31</sub>		15691.2406 (-17)	14263.9390 (-64)

**Table A1-5 (Continued)**

$J_{KaKc} - J'_{Ka'Kc'}$	<i>syn</i> -PO-H <sub>2</sub> <sup>16</sup> O-H <sub>2</sub> <sup>16</sup> O	<i>syn</i> -PO-H <sub>2</sub> <sup>18</sup> O-H <sub>2</sub> <sup>18</sup> O	<i>anti</i> -PO-H <sub>2</sub> <sup>16</sup> O-H <sub>2</sub> <sup>16</sup> O
6 <sub>06</sub> - 5 <sub>05</sub>	18179.3686 (-39)	16594.1938 (30)	16292.3205 (-16)
6 <sub>16</sub> - 5 <sub>15</sub>	18002.5457 (28)	17567.3494 (-28)	
6 <sub>15</sub> - 5 <sub>14</sub>			
$J_{KaKc} - J'_{Ka'Kc'}$	<i>anti</i> -PO-H <sub>2</sub> <sup>18</sup> O-H <sub>2</sub> <sup>18</sup> O	<i>anti</i> -PO-H <sub>2</sub> <sup>16</sup> O-H <sub>2</sub> <sup>16</sup> O	<i>anti</i> -PO-H <sub>2</sub> <sup>18</sup> O-H <sub>2</sub> <sup>18</sup> O
2 <sub>02</sub> - 1 <sub>01</sub>	5367.5727 (-5)	5512.3414 (-6)	5509.0914 (53)
2 <sub>12</sub> - 1 <sub>11</sub>	5160.5262 (28)	5309.7798 (49)	5302.3794 (21)
2 <sub>11</sub> - 1 <sub>10</sub>	5607.4136 (10)	5744.7305 (-47)	5747.4119 (-1)
3 <sub>03</sub> - 2 <sub>02</sub>	8010.8059 (7)	8231.5346 (-2)	8224.4935 (44)
3 <sub>13</sub> - 2 <sub>12</sub>	7730.7947 (-9)	7955.5455 (10)	7943.9104 (-42)
3 <sub>12</sub> - 2 <sub>11</sub>	8400.3560 (-2)	8607.3275 (40)	8610.7415 (-23)
3 <sub>22</sub> - 2 <sub>21</sub>	8075.7464 (70)	8290.6629 (8)	8287.1361 (7)
3 <sub>21</sub> - 2 <sub>20</sub>	8140.8608 (-3)	8349.9676 (-19)	8349.9657 (13)
4 <sub>04</sub> - 3 <sub>03</sub>	10608.5950 (0)	10908.9378 (-34)	10895.8484 (-16)
4 <sub>14</sub> - 3 <sub>13</sub>	10290.1067 (-18)	10591.2473 (-15)	10574.8295 (-24)
4 <sub>13</sub> - 3 <sub>12</sub>	11179.3071 (-3)	11457.2627 (2)	11460.6181 (-25)
4 <sub>23</sub> - 3 <sub>22</sub>	10754.6856 (-24)		
4 <sub>22</sub> - 3 <sub>21</sub>	10913.8297 (-24)		
5 <sub>05</sub> - 4 <sub>04</sub>	13154.7662 (14)	13537.9593 (1)	13516.7022 (14)
5 <sub>15</sub> - 4 <sub>14</sub>	12836.4216 (-13)	13214.9135 (-7)	13193.1018 (-5)
5 <sub>14</sub> - 4 <sub>13</sub>	13937.7990 (-7)	14288.8054 (25)	14290.8730 (0)
5 <sub>24</sub> - 4 <sub>23</sub>	13422.5780 (-40)		
5 <sub>23</sub> - 4 <sub>22</sub>	13727.0891 (6)		



**Table A1-5 (Continued)**

$J_{KaKc} - J'_{KaKc}$	<i>anti</i> -PO-H <sub>2</sub> <sup>18</sup> O-H <sub>2</sub> <sup>18</sup> O	<i>anti</i> -PO-H <sub>2</sub> <sup>18</sup> O-H <sub>2</sub> <sup>16</sup> O	<i>anti</i> -PO-H <sub>2</sub> <sup>16</sup> O-H <sub>2</sub> <sup>18</sup> O
5 <sub>33</sub> - 4 <sub>32</sub>	13507.7130 (75)		
5 <sub>32</sub> - 4 <sub>31</sub>	13523.4366 (-64)		
6 <sub>06</sub> - 5 <sub>05</sub>	15653.7633 (-29)	16121.1271 (11)	16090.5566 (-11)
6 <sub>16</sub> - 5 <sub>15</sub>	15368.85779 (38)	15825.5730 (3)	15797.7916 (15)
6 <sub>15</sub> - 5 <sub>14</sub>	16667.9270 (20)	17094.9464 (-16)	17093.9724 (8)

<sup>a</sup>The residuals (obs-calc) in parentheses are expressed in units of the last digits.

**Table A1-6** Experimental transition frequencies of unassigned lines in the enantiopure PO sample using 7 bar of helium as carrier gas.

Frequency /MHz	MW pulse width / $\mu$ s	S/N (cycles)
4560.8954	3.0	71 (100)
4597.2230	1.0	553 (100)
5123.4860	1.0	120 (20)
5237.4605	1.5	1223 (100)
5297.0346	2.0	1622 (100)
5298.1517	2.0	68 (100)
5321.2883	2.0	80 (100)
5451.4239	0.8	1276 (100)
5453.5084	0.8	997 (100)
5474.3416 <sup>a</sup>	2.5	98 (100)
5489.0596	0.8	651 (10)
6312.1437 <sup>a</sup>	0.8	74 (100)
6327.9106	0.8	435 (100)
6378.3983	6.0	231 (100)
6387.2150	1.0	168 (10)
6396.8564	1.0	1392 (100)
6421.4906	1.0	344 (10)
6431.1346	1.0	98 (100)
6466.0086 <sup>a</sup>	0.3	113 (100)
6478.8187	1.2	173 (20)
6515.7429	4.0	285 (100)
6923.9020	2.0	286 (100)
6997.3482	2.0	88 (100)
7132.3338	4.0	133 (100)
8032.3149	1.0	567 (100)

<sup>a</sup> Transitions were also measured in racemic sample.

**Table A1-7** Experimental transition frequencies of unassigned lines in the racemic PO sample using 7 bar of helium as carrier gas.

Frequency /MHz	MW pulse width / $\mu$ s	S/N (cycles)
5188.7066	1.5	182 (20)
5226.6590	0.8	928 (20)
5278.3245	1.2	60 (100)
5309.6443	0.8	1022 (20)
5474.3416 <sup>a</sup>	2.5	98 (100)
5570.2289	4.5	65 (300)
5575.7044	4.0	193 (100)
5606.1984	1.0	855 (100)
5606.9679	1.0	1126 (100)
5612.9251	3.5	325 (100)
5613.6918	4.0	949 (100)
5632.0919	3.0	174 (100)
5985.1455	5.5	34 (100)
6077.2126	1.2	50 (20)
6103.3737	1.0	52 (100)
6109.0756	1.8	340 (100)
6131.4827	1.2	403 (100)
6141.4371	0.8	208 (20)
6312.1437 <sup>a</sup>	0.8	74 (100)
6327.9171	0.5	24 (20)
6466.0086 <sup>a</sup>	0.3	113 (100)
6812.6612	0.5	173 (10)
6922.3299	1.5	120 (50)
6928.2974	1.5	28 (50)
6930.3284	1.5	34 (50)
6975.2845	1.5	102 (100)
7036.1284	1.2	253 (100)
7046.0833	1.2	589 (50)
7048.4286	1.2	223 (50)
7077.1294	1.2	277 (50)
7015.0493	1.2	144 (50)
7309.4487	1.2	356 (50)

**Table A1-7 (Continued)**

Frequency /MHz	MW pulse width / $\mu$ s	S/N (cycles)
7342.9721	1.0	122 (100)
7384.4370	1.0	440 (100)
7437.8275	1.2	227 (50)
7448.1390	1.2	119 (100)
7898.4946	0.8	79 (20)
8197.5090	3.5	580 (100)

<sup>a</sup> Transitions were also measured in racemic sample.

**Table A1-8** Experimental transition frequencies in the unit MHz of the three homochiral configurations of PO dimer.

$J_{KaKc} - J'_{Ka'Kc'}$	<i>RR2</i>	<i>RR4</i>	<i>RR5</i>
1 <sub>11</sub> – 0 <sub>00</sub>	4066.3182 (-2) <sup>a</sup>		
3 <sub>22</sub> – 2 <sub>11</sub>	12198.8231 (24)		
2 <sub>12</sub> – 1 <sub>11</sub>	3798.5008 (-15)		
2 <sub>02</sub> – 1 <sub>01</sub>	3954.2211 (-11)		
2 <sub>11</sub> – 1 <sub>10</sub>	4128.7702 (-30)		
2 <sub>12</sub> – 1 <sub>01</sub>	5882.9875 (-2)		
2 <sub>21</sub> – 2 <sub>12</sub>	6748.8672 (15)		
2 <sub>20</sub> – 2 <sub>11</sub>	6262.8740 (-86)		
2 <sub>21</sub> – 1 <sub>10</sub>	10382.2321 (26)		
2 <sub>20</sub> – 1 <sub>11</sub>	10556.7959 (16)		
2 <sub>11</sub> – 1 <sub>01</sub>	6378.3966 (-5)		
3 <sub>13</sub> – 2 <sub>12</sub>	5691.9863 (-12)	5246.4403 (4)	5291.8351 (5)
3 <sub>03</sub> – 2 <sub>02</sub>	5907.9254 (-21)	5381.3028 (-8)	5382.8502 (3)
3 <sub>12</sub> – 2 <sub>11</sub>	6187.0379 (-39)	5531.9553 (4)	5480.9611 (-19)
3 <sub>22</sub> – 2 <sub>21</sub>	5945.3639 (-5)		
3 <sub>21</sub> – 2 <sub>20</sub>	5982.8627 (-28)		
3 <sub>03</sub> – 2 <sub>12</sub>	3979.1756 (137)		
3 <sub>13</sub> – 2 <sub>02</sub>	7620.7586 (56)		
3 <sub>21</sub> – 3 <sub>12</sub>	6058.7134 (71)		
3 <sub>22</sub> – 3 <sub>13</sub>	7002.2438 (13)		
4 <sub>14</sub> – 3 <sub>13</sub>	7579.0138 (-13)	6992.5491 (0)	7054.5160 (-8)
4 <sub>04</sub> – 3 <sub>03</sub>	7834.6963 (-12)	7164.1505 (1)	7172.1692 (-2)
4 <sub>13</sub> – 3 <sub>12</sub>	8237.4900 (-16)	7373.0440 (0)	7306.6287 (24)
4 <sub>22</sub> – 3 <sub>21</sub>	8012.1891 (-9)	7208.9901 (-2)	
4 <sub>22</sub> – 3 <sub>22</sub>			
4 <sub>23</sub> – 3 <sub>22</sub>	7919.7410 (-8)		7181.8432 (0)
4 <sub>31</sub> – 3 <sub>30</sub>	7946.8443 (-81)		
4 <sub>32</sub> – 3 <sub>31</sub>	7944.8438 (81)		
4 <sub>04</sub> – 3 <sub>13</sub>	6121.8654 (-65)		
4 <sub>22</sub> – 4 <sub>13</sub>	5833.3899 (-149)		
4 <sub>23</sub> – 4 <sub>14</sub>	7342.9703 (10)		
5 <sub>15</sub> – 4 <sub>14</sub>	9458.1694 (3)		8816.1500 (3)

**Table A1-8 (Continued)**

$J_{KaKc} - J'_{Ka'Kc'}$	<i>RR2</i>	<i>RR4</i>	<i>RR5</i>
$5_{05} - 4_{04}$	9728.9441 (28)		8957.2774 (0)
$5_{14} - 4_{13}$	10276.7172 (37)		9131.1204 (-9)
$5_{23} - 5_{14}$	5624.2803 (67)		
$5_{24} - 5_{15}$	7772.5908 (-7)		
$5_{05} - 4_{14}$	8271.7955 (-27)		

<sup>a</sup> The residuals (obs-calc) in parentheses are expressed in units of the last digits.

**Table A1-9** Experimental transition frequencies in the unit MHz of the three heterochiral configurations of PO dimer.

$J_{KaKc} - J'_{Ka'Kc'}$	<i>RS2</i>	<i>RS4</i>	<i>RS5</i>
$2_{12} - 1_{01}$	6126.7008 (22) <sup>a</sup>	6105.0622 (-6)	6315.0724 (9)
$2_{11} - 1_{01}$	6208.7426 (-38)	6435.2798 (-82)	
$2_{21} - 2_{12}$	6619.5688 (0)	7789.4897 (0)	
$3_{03} - 2_{02}$	5961.2545 (43)	5578.7044 (34)	5272.2823 (-3)
$3_{12} - 2_{11}$	6003.1194 (3)	5755.8000 (-56)	5412.5000 (-1)
$3_{13} - 2_{12}$	5921.0670 (-126)	5425.6686 (34)	5145.7149 (5)
$3_{21} - 2_{20}$	5963.2431 (31)		
$3_{22} - 2_{21}$	5962.2195 (17)		
$3_{13} - 2_{02}$	8073.1584 (16)	7805.6261 (2)	7942.5391 (-12)
$3_{12} - 2_{02}$		8465.9999 (85)	
$4_{04} - 3_{03}$	7947.0625 (7)	7421.7070 (19)	7020.2581 (2)
$4_{14} - 3_{03}$			9528.8658 (0)
$4_{13} - 3_{12}$	8003.7746 (25)	7669.9681 (-22)	7214.1765 (1)
$4_{14} - 3_{13}$	7894.4069 (34)	7230.1517 (-28)	6858.6084 (2)
$4_{22} - 3_{21}$	7951.8982 (-16)		7059.0394 (0)
$4_{23} - 3_{22}$	7949.3446 (-10)		
$5_{05} - 4_{04}$	9931.7870 (0)		8760.2822 (1)
$5_{14} - 4_{13}$	10004.0878 (-15)		9013.6309 (0)
$5_{15} - 4_{14}$	9867.4154 (-1)		8569.5771 (-5)
$5_{15} - 4_{04}$			11078.1858 (3)

<sup>a</sup> The residuals (obs-calc) in parentheses are expressed in units of the last digits.

## Appendix 2

Tables of *ab initio* Cartesian coordinates  
for the PO containing complexes



**Table A2-1** Cartesian coordinates (in Å) for the two configurations of the PO–H<sub>2</sub>O complex obtained from the *ab initio* geometry optimization calculations with MP2/6-311++G(d,p). The atom numbering is in accordance with Figure 5-3.

	<i>syn</i> -PO-H <sub>2</sub> O			<i>anti</i> -PO-H <sub>2</sub> O		
	x	y	z	x	y	z
O1	0.128547	-0.799604	-0.682218	0.068812	0.274073	0.788684
C2	0.718223	-1.092182	0.605927	-0.277116	1.176290	-0.289780
C3	1.215825	0.026696	-0.204326	-0.700955	-0.228208	-0.329274
H4	0.067664	-0.876936	1.449584	-1.001350	1.937755	-0.014482
H5	1.271944	-2.025399	0.642055	0.569122	1.496701	-0.890453
H6	2.134760	-0.139894	-0.763844	-0.120586	-0.894319	-0.965605
C7	0.879705	1.455114	0.120439	-2.110136	-0.644163	-0.019154
H8	1.668195	1.889599	0.743277	-2.688738	-0.730360	-0.944335
H9	-0.072454	1.511748	0.652812	-2.587364	0.093402	0.630826
H10	0.801415	2.045216	-0.797281	-2.119615	-1.614480	0.485350
H11	-1.636870	-0.165948	-0.348625	1.860286	-0.231257	0.406445
O12	-2.375615	0.221001	0.144528	2.593407	-0.426697	-0.196533
H13	-3.140627	0.052670	-0.408699	3.319743	-0.659968	0.384303

**Table A2-2** Cartesian coordinates (in Å) of the three conformers of the PO-(H<sub>2</sub>O)<sub>2</sub> complex obtained from the *ab initio* geometry optimization calculations at the MP2/6-311++G(d,p) level of theory.

	<i>syn</i> -PO-(H <sub>2</sub> O) <sub>2</sub>		
	x	y	z
C	-1.184534	0.901145	1.194195
C	-1.681120	0.004355	0.095507
O	1.915693	1.330351	-0.464514
C	-1.073724	0.017235	-1.242267
O	-0.794477	-1.064918	-0.314425
O	1.816759	-1.247824	0.594009
H	-2.714199	-0.331359	0.168566
H	-1.661994	-0.287829	-2.102487
H	-0.227562	0.674828	-1.419946
H	0.882508	-1.295940	0.320009
H	-1.820678	1.790137	1.256787
H	-1.223279	0.382364	2.156722
H	-0.158771	1.216229	0.991274
H	2.180184	-2.103957	0.358334
H	2.136352	0.458649	-0.098323
H	2.739913	1.819602	-0.436106

**Table A2-2 (Continued)**

<i>anti</i> -PO-(H <sub>2</sub> O) <sub>2</sub>			
	x	y	z
C	-2.540044	0.031016	-0.716159
C	-1.132441	0.272416	-0.253183
O	-0.502148	-0.836783	0.436877
C	-0.784111	0.386198	1.167414
O	2.108511	-1.302540	-0.317354
O	1.979566	1.475250	-0.174782
H	-0.455915	0.766466	-0.946924
H	0.097955	0.954359	1.444095
H	-1.567420	0.274430	1.912060
H	1.179631	-1.287195	-0.020191
H	-3.021971	0.983589	-0.958503
H	-2.545389	-0.595203	-1.612976
H	-3.116538	-0.470274	0.065400
H	2.517008	-2.001712	0.197084
H	2.279838	0.556324	-0.260935
H	2.684951	1.994020	-0.565470
<i>bi</i> -PO-(H <sub>2</sub> O) <sub>2</sub>			
C	-1.099105	1.716668	-0.450853
C	0.154766	1.044859	0.030049
O	-2.434814	-1.450683	-0.125683
C	0.177696	0.194864	1.225907
O	0.197623	-0.406001	-0.099344
O	2.987375	-0.572319	-0.309069
H	1.100658	1.499072	-0.258498
H	1.105500	0.069770	1.775339
H	-0.749452	0.021666	1.764706
H	2.046653	-0.775098	-0.416526
H	-1.152848	2.728411	-0.036287
H	-1.095522	1.793014	-1.541947
H	-1.981585	1.152685	-0.140824
H	3.436342	-1.263336	-0.799629
H	-1.501332	-1.266301	-0.304939
	-2.610029	-2.266200	-0.599242

**Table A2-3** Cartesian coordinates (in Å) for the twelve configurations of PO dimer obtained from the *ab initio* geometry optimization calculations with the MP2/6-311++G(d,p) level of theory.

	RR1			RS1		
	x	y	z	x	y	z
C	-1.952397	0.832013	-0.573895	1.928120	0.338664	-0.102340
C	-2.111842	0.760088	0.884197	1.551827	1.689002	-0.540152
O	-1.006634	1.481046	0.303566	1.043235	1.154948	0.697763
C	-1.765260	-0.487661	1.647454	0.545575	1.906458	-1.635965
H	-2.570511	1.513148	-1.152630	2.906205	0.169113	0.340297
H	-1.555162	-0.037468	-1.090804	1.439496	-0.511195	-0.570214
H	-2.852102	1.418532	1.337689	2.281350	2.483943	-0.387912
H	-1.343787	-0.234377	2.625366	-0.067676	2.787650	-1.422820
H	-1.035533	-1.073744	1.084182	-0.102359	1.031736	-1.726296
H	-2.664654	-1.091573	1.807318	1.058370	2.067976	-2.589854
C	1.362609	-0.088918	-1.471894	-1.926987	-0.334934	0.106762
C	1.985385	-0.839898	-0.374233	-1.552412	-1.687788	0.538250
O	0.686315	-1.216057	-0.873675	-1.042257	-1.148162	-0.696543
C	2.027461	-0.289508	1.023927	-0.547284	-1.911602	1.633762
H	1.692392	-0.252482	-2.494366	-1.437932	0.512231	0.579065
H	0.910382	0.872765	-1.244747	-2.904496	-0.162264	-0.335933
H	2.761667	-1.557237	-0.638836	-2.282587	-2.481255	0.381492
H	1.917640	-1.095145	1.756714	0.065315	-2.792332	1.416943
H	1.218421	0.431617	1.160621	-1.060967	-2.077043	2.586498
H	2.986326	0.208412	1.202379	0.101466	-1.037956	1.728815

**Table A2-3 (Continued)**

	<i>RR2</i>			<i>RS2</i>		
	x	y	z	x	y	z
C	0.498207	-1.993285	-1.675199	2.187220	0.510409	0.101869
C	-0.313466	-1.781516	-0.469089	1.511261	1.813580	0.048603
O	0.774159	-0.888953	-0.790210	1.207862	0.875094	1.098684
C	-0.137971	-2.625165	0.761177	0.408618	2.089690	-0.935580
H	0.108822	-1.707413	-2.648698	3.206606	0.448786	0.474008
H	1.253787	-2.775156	-1.671716	1.859191	-0.271375	-0.577792
H	-1.289594	-1.317676	-0.594497	2.069899	2.678751	0.404779
H	-0.350084	-2.031642	1.653647	-0.345417	2.746499	-0.490179
H	0.886433	-3.004443	0.813382	-0.067404	1.153869	-1.237653
H	-0.828322	-3.474951	0.737351	0.813342	2.586678	-1.823618
C	0.288945	0.948162	1.870487	-1.030110	-2.532496	-0.523823
C	-0.758541	1.814649	1.313418	-0.782203	-1.488545	0.479714
O	-1.050184	0.448134	1.662440	-0.352076	-1.312478	-0.886316
C	-0.805148	2.149341	-0.151452	-1.872636	-0.572268	0.956271
H	0.573336	1.051507	2.914479	-2.028934	-2.635230	-0.940972
H	1.030777	0.529411	1.196079	-0.406544	-3.422139	-0.548902
H	-1.223590	2.531267	1.989933	0.047786	-1.638573	1.167079
H	-1.842769	2.221845	-0.492541	-1.452632	0.407012	1.197589
H	-0.290737	1.374432	-0.724955	-2.342727	-0.981994	1.856504
H	-0.316558	3.112488	-0.333184	-2.634762	-0.458522	0.180178

**Table A2-3 (Continued)**

	<i>RR3</i>			<i>RS3</i>		
	x	y	z	x	y	z
C	0.327036	2.800548	0.016249	1.523596	2.454924	-0.173047
C	-0.448609	1.590971	-0.288340	1.340406	1.072199	-0.633712
O	0.943170	1.499684	0.086671	0.595983	1.577276	0.494919
C	-0.781828	1.200093	-1.700200	2.347900	-0.001013	-0.334988
H	0.204788	3.297784	0.974754	1.062067	3.274767	-0.717128
H	0.674880	3.422443	-0.805142	2.409683	2.702982	0.406364
H	-1.118746	1.213621	0.480927	0.719008	0.911937	-1.512686
H	-0.814686	0.111430	-1.790020	1.840003	-0.960988	-0.214535
H	-0.030193	1.598297	-2.387734	2.894274	0.240574	0.581018
H	-1.762783	1.599031	-1.979385	3.062265	-0.087962	-1.160516
C	-0.427947	-2.561644	1.119951	-1.601118	-2.162066	-0.138829
C	0.539754	-1.514411	0.767452	-1.417912	-0.779344	0.321840
O	-0.824363	-1.446165	0.298090	-0.673565	-1.284401	-0.806851
C	1.591893	-1.731834	-0.282834	-2.425416	0.293878	0.023191
H	-0.875106	-2.577824	2.110247	-2.487245	-2.410131	-0.718177
H	-0.383645	-3.514899	0.598631	-1.139541	-2.981909	0.405212
H	0.765968	-0.761558	1.519295	-0.796452	-0.619087	1.200772
H	1.802818	-0.793679	-0.802182	-1.917484	1.253810	-0.097466
H	1.251915	-2.478390	-1.006221	-3.139607	0.380964	0.848855
H	2.518901	-2.085473	0.180809	-2.971989	0.052224	-0.892678

**Table A2-3 (Continued)**

	<i>RR4</i>			<i>RS4</i>		
	x	y	z	x	y	z
C	0.201491	1.165148	1.463534	-1.580861	-0.729733	1.486816
C	-0.354155	1.752489	0.239428	-1.870342	0.644037	0.949231
O	0.854686	0.967892	0.190892	-0.762201	1.338398	0.344586
C	-0.205606	3.212688	-0.083707	-1.862158	0.920673	-0.493143
H	-0.260411	0.272341	1.873402	-2.462192	1.736133	-0.888280
H	0.747024	1.804891	2.153266	-1.617648	0.108191	-1.171875
H	-1.209184	1.236894	-0.194250	-2.481772	1.291437	1.577168
H	-0.098332	3.357528	-1.162932	-1.021023	-0.662948	2.425110
H	0.678864	3.621326	0.411779	-0.996945	-1.297769	0.758887
H	-1.088347	3.766667	0.252004	-2.517606	-1.261254	1.684395
C	-0.818357	-1.491069	-1.233591	2.834548	-1.694655	-0.331305
C	-0.607266	-2.477683	-0.166167	1.391431	-0.018034	-1.693511
O	-1.442968	-1.325579	0.057880	0.586606	-1.137261	-1.265703
C	0.677937	-2.528146	0.611987	1.695478	-0.720695	-0.442004
H	-1.508837	-1.712212	-2.043230	2.003913	-0.214755	-2.570237
H	-0.026522	-0.775169	-1.436491	0.888197	0.943199	-1.647790
H	-1.175653	-3.405394	-0.226128	1.374181	-0.228133	0.473498
H	0.482288	-2.788555	1.657013	3.726053	-1.192716	0.058724
H	1.174806	-1.556113	0.570401	3.066944	-2.118355	-1.311820
H	1.343870	-3.287503	0.188979	2.574919	-2.512069	0.348262

**Table A2-3 (Continued)**

	<i>RR5</i>			<i>RS5</i>		
	x	y	z	x	y	z
C	-0.149665	2.455216	0.109360	2.165656	1.723360	-0.841469
C	1.033942	1.530530	0.110465	1.072031	1.546446	0.123372
O	1.216213	0.727772	-1.074034	1.125762	0.753744	-1.080340
C	2.187433	1.749702	-0.772325	-0.062067	2.525927	0.223102
H	3.167390	1.374945	-0.489211	3.144653	1.297874	-0.637857
H	2.176908	2.598622	-1.451652	2.145651	2.581932	-1.508379
H	1.201283	0.971805	1.028746	1.281383	0.966719	1.020042
H	-1.059584	1.893433	0.334106	-0.979342	2.002869	0.503932
H	-0.251423	2.934549	-0.868425	-0.210238	3.028542	-0.736862
H	-0.023215	3.231661	0.871198	0.156769	3.280551	0.985943
C	-2.820123	-1.549109	-0.825100	-1.529706	-0.935634	-0.518502
C	-1.414910	-1.045409	-0.649672	-0.501837	-1.740213	0.152501
O	-1.029916	-0.705904	0.697926	-1.079241	-0.594677	0.810168
C	-0.390861	-1.827645	0.052723	-0.812339	-3.077178	0.764899
H	-0.661227	-2.796756	0.465608	-2.547788	-1.315515	-0.563086
H	-1.053706	-0.328074	-1.384436	-1.229276	-0.233281	-1.290388
H	0.654072	-1.668024	-0.195595	0.524670	-1.568703	-0.166143
H	-3.533084	-0.720146	-0.780675	-0.212930	-3.233981	1.666791
H	-2.927587	-2.043438	-1.796179	-0.585532	-3.880830	0.056652
H	-3.067208	-2.262974	-0.034937	-1.869817	-3.132086	1.036312



**Table A2-3 (Continued)**

	<i>RR6</i>			<i>RS6</i>		
	x	y	z	x	y	z
C	-1.429041	1.187388	0.076688	1.212291	1.030046	1.158451
C	-0.620984	2.106039	-0.733065	0.638149	1.840649	0.078681
O	-0.162728	1.678935	0.565126	1.400229	0.654038	-0.221953
C	-0.961425	3.563960	-0.864851	1.251135	3.143501	-0.351925
H	-2.295672	1.576139	0.606101	0.560940	0.367593	1.720968
H	-1.433715	0.131517	-0.176466	2.114357	1.378139	1.656075
H	-0.055512	1.655896	-1.547189	-0.427405	1.711223	-0.101332
H	-0.050136	4.165708	-0.933922	1.134557	3.283785	-1.430797
H	-1.555879	3.734562	-1.768387	2.317632	3.157162	-0.112732
H	-1.533803	3.898521	0.004191	0.762096	3.979556	0.158626
C	2.137038	-0.256731	-0.665000	-1.211771	-1.029593	-1.157788
C	3.330503	-0.746383	-1.436139	-0.638958	-1.841100	-0.078005
O	0.857091	-0.762803	-1.093095	-1.401278	-0.654896	0.222859
C	1.356560	-1.141356	0.207302	-1.252042	-3.144536	0.350686
H	1.645075	-2.186498	0.290317	-2.113358	-1.377148	-1.656627
H	2.108934	0.803677	-0.420141	-0.559686	-0.366628	-1.718817
H	0.812479	-0.708150	1.041127	0.426444	-1.711823	0.103229
H	4.251020	-0.545474	-0.878337	-1.135963	-3.286091	1.429431
H	3.251001	-1.822145	-1.612772	-0.762523	-3.979870	-0.160595
H	3.396562	-0.238925	-2.403313	-2.318421	-3.158140	0.110971